ELECTRON TEMPERATURE DYNAMICS OF TEXTOR PLASMAS

ELEKTRONEN TEMPERATUUR DYNAMICA VAN TEXTOR PLASMA'S

(met een samenvatting in het Nederlands)

PROEFSCHRIFT

ter verkrijging van de graad van doctor aan de Universiteit Utrecht, op gezag van de Rector Magnificus, Prof. Dr. W.H. Gispen, ingevolge het besluit van het College voor Promoties in het openbaar te verdedigen op

dinsdag 18 november 2003

des morgens te 10.30 uur

door

VICTOR SERGEEVICH UDINTSEV

geboren op 17 maart 1975 te Moskou, Rusland

Promotor: Prof. Dr. F.C. Schüller
Co-Promotor: Dr. A.J.H. Donné

Reading this book will have increased the amount of ordered information in your brain. However, during the same time, the heat released by your body will have had a much greater effect increasing the disorder in the rest of the universe. I suggest you stop reading now.

<u>From</u>: *Stephen Hawking,*
The Illustrated a Brief History of Time.

Aan Natasha

Contents

Chapter 1

Introduction

1.1 Principles of nuclear fusion

At the present time, most of the world's energy is produced by burning fossil fuels like coal, gas and oil, which are limited to some $100 - 200$ years of use. However, already in 50 years from now, the world population will rise to about 10 billion people [1], and the energy consumption is estimated to rise to a value that is approximately three times higher than what is being consumed now [2]. Thus, continuation of the burning of fossil fuels for energy production could pose a serious problem in the future. Moreover, the massive use of fossil fuels might lead to the release of giant quantities of CO_2 into the atmosphere. CO_2 is a greenhouse gas that leads to an increased absorption of the infrared radiation re-emitted by the Earth. This explains the importance of renewable energy sources, such as windmills, solar panel power plants, biogas power factories and many others, to overcome the abovementioned environmental effects [3]. For a number of reasons, however, the renewable energy sources can only cover approximately several tens of percent of the world energy need and therefore it is important to explore also other forms of electricity production.

One option is given by nuclear energy: *fission* and *fusion*. Fission reactors do not contribute to the greenhouse effect, but they produce a highly radioactive waste that needs to be isolated and/or reprocessed. With present fission reactor types, uranium resources are limited to about 50 years of use. Using breeder technology, however, it would be possible to transform non-fissile fuel into fissile elements and, thus, to extend resources up to 2500 $- 3000$ years.

Controlled thermonuclear fusion can fulfil the demand of mankind to have an inexhaustible source of energy that does not cause any serious environmental pollution. To produce energy, two light nuclei must be brought close enough together to overcome the so-called Coulomb barrier such they can fuse. The kinetic energy of these nuclei should be high enough to cross the barrier and arrive in the zone very close to the nucleus, where the nuclear forces are larger than the electrostatic repulsion (Fig. 1.1). In the nuclear reaction, according to the famous Einstein equation $E = mc^2$, a small portion of mass is released in the form of energy. The probability of crossing the Coulomb barrier can be quantified by a so-called effective cross-section. Figure 1.2 shows the energy dependence (expressed in keV) of several effective cross-sections for fusion reactions that are given below [4]:

$$D+T \Rightarrow {}^4He+n+17.6\,MeV$$
$$D+D \Rightarrow \begin{cases} {}^3He+n+3.3\,MeV \\ T+p+4.0\,MeV \end{cases}.$$
$$D+{}^3He \Rightarrow {}^4He+p+18.3\,MeV$$

$$(1.1)$$

The most accessible fusion reaction is the reaction involving deuterium (*D*) and tritium (*T*). It is on this reaction that most research on controlled fusion is being conducted.
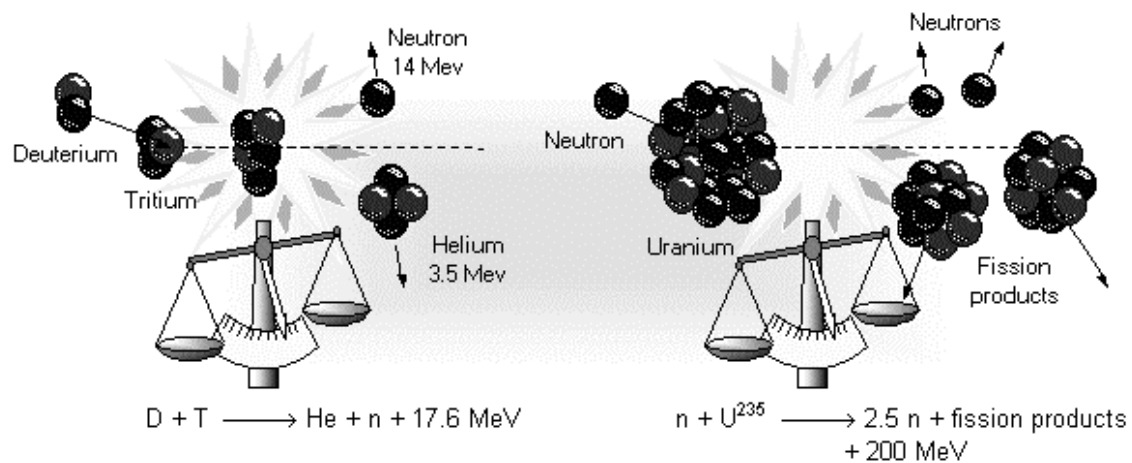
FIG. 1.1. A comparison between fusion (D - T) and fission (n - U^{235}) reactions [4]. In a fusion reaction, light atomic nuclei (D, T) join to build heavier atoms (He) with an energy of 3.5 MeV and to release neutrons (n) with an energy of 14 MeV.
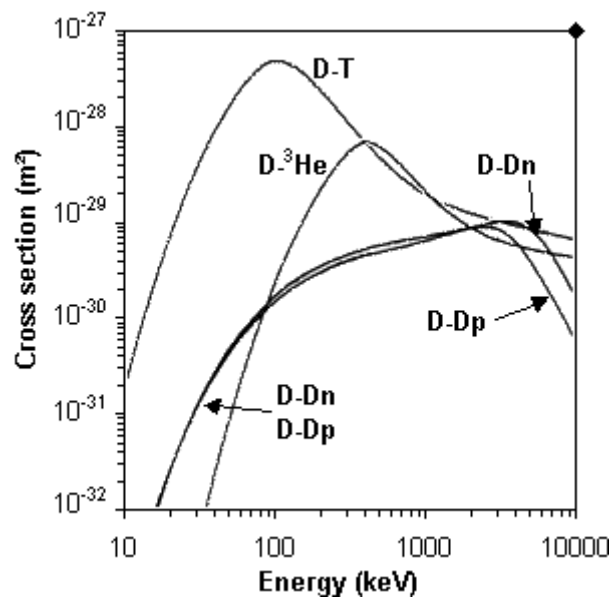
FIG. 1.2. Effective cross-sections versus interaction energy for different types of fusion reactions [4]. The D-T reaction is the most accessible one.

The temperature (which measures the interaction energy) required for nuclear fusion reactions should exceed a hundred million degrees. At this temperature electrons are detached from the nucleus. Thus, atoms are ionised and form a gas of ions and electrons. This is the fourth aggregate state of matter called *plasma*. Plasma is the most widespread form of matter in the Universe and exists in a large diversity of objects.

A star (and our Sun in particular) starts to shine when, under the action of gravity, the matter inside it attains sufficiently high densities and temperatures to set off

thermonuclear reactions. In this way the natural tendency of the plasma of dispersing and, therefore, cooling down is balanced by the gravitational force. On Earth, however, gravitational confinement of plasma is impossible. Two possible scenarios are being studied to generate fusion energy from thermonuclear reactions: *inertial confinement*, in which a small volume of matter is being raised to very high density and temperature in a short time, and *magnetic confinement*, in which a hot plasma is confined by a force from external magnetic fields. Experimental devices that are based on the idea of magnetic confinement seem to be the most promising at this time.

The aim in thermonuclear fusion research is to build a continuously operating reactor in which the energy released by the fusion reactions is sufficiently high to keep the plasma hot and to produce more fusion reactions. A criterion for a self-sustained fusion reactor has been derived by Lawson from the energy balance, taking into account energy sources and losses in the plasma [5]. It gives the value of the product of plasma density n_p, the energy confinement time τ_E and the plasma temperature T_p to attain a given amplification factor, Q, between energy put in the plasma to keep it hot and the energy released by fusion. For $Q = 1$ *(i.e. break-even)* one gets:

$$n_p \cdot \tau_E \cdot T_p > 10^{21} \; keV \cdot s \cdot m^{-3} \; \text{for } T_p \text{ between 10 to 20 keV.} \qquad (1.2)$$

In other words, to be able to produce energy from fusion reactions, a sufficiently hot (T_p) and dense (n_p) plasma must be confined effectively (τ_E). In future fusion reactors, the electron and ion temperatures will be almost equal. For $Q = \infty$, i.e. self-sustained 'burning', one needs about 4×10^{21} keV·s·m^{-3}. In present day machines like JET (EU) and JT-60U (Japan), value in excess of 1×10^{21} keV·s·m^{-3} have already been reached.

1.2 The tokamak device

Research on thermonuclear fusion can be traced back to the 1920's, when Aston had measured the "mass defect" in helium, which suggested a possibility of obtaining a large amount of energy by synthesis of a helium nucleus from hydrogen. Soon after this discovery, the British astronomer Eddington suggested that the energy of stars was "sub-atomic", and that "Man will learn one day to free this energy and use it to his own ends".

Since then, a large number of magnetic configurations for nuclear fusion research have been invented: z- and theta-pinches, magnetic traps, stellarators and many others. The most efficient magnetic configuration so far has been invented in the 1950's by Soviet scientists. This device has been called "Tokamak", which is an acronym for the Russian name "TOroidal'naya KAmera MAGnitnaya"; the letter "G" has been substituted to "K" to ease the pronunciation [6]. Tokamaks have rapidly replaced many other magnetic configurations in the research of controlled nuclear fusion. Today, only stellarators are still considered as a possible alternative to the tokamaks, albeit that their present performance is significantly lower than that of tokamaks.

A tokamak has a vacuum chamber in the form of a torus with major radius, R_0, from the centre to the axis of the chamber, and minor radius, a. The toroidal magnetic field B_φ is created by external coils, whereas the poloidal magnetic field B_θ is induced by a current flowing toroidally in the plasma (Fig. 1.3). This plasma current (I_p) is generated by means of a transformer, of which the second winding is the plasma itself. The plasma is
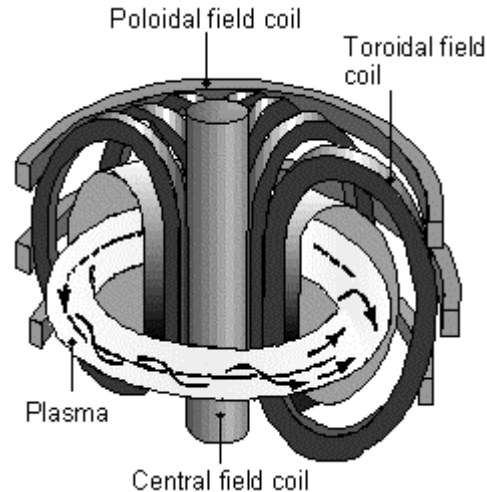
FIG. 1.3. A simplified scheme of the magnetic configuration of a tokamak [4]. The resultant helical magnetic field is created by a central field coil (transformer yoke), and sets of toroidal and poloidal magnetic coils.

confined by the resulting helical magnetic field. An additional set of poloidal magnetic coils takes care of the equilibrium shape and position of the plasma, and helps to control the plasma current. The plasma current heats the plasma by Ohmic dissipation. Additional heating can be applied to the plasma by Neutral Beam Injection (NBI) and/or by injection of microwave power, such as Electron Cyclotron Resonance Heating (ECR), Lower Hybrid Heating (LHH), Ion Cyclotron Resonance Heating (ICRH), and some others.

The research results that are reported in this thesis are obtained at the TEXTOR tokamak (Tokamak EXperiment for Technology Oriented Research) at the Institut für Plasmaphysik of the Forschungszentrum Jülich, Germany. This is a medium-sized machine with pulse duration of up to 10 s. Nowadays, the largest tokamak in the world is JET (Joint European Torus) in the United Kingdom. In the coming years, the construction of an even larger machine, ITER (Latin word for 'The way'), that will produce a fusion plasma with at least $Q = 10$, and demonstrate the feasibility of a future power plant, will start. Some typical parameters of the TEXTOR, JET and ITER tokamaks are given in Table 1.1 for comparison. Figure 1.4 gives the thermonuclear power versus pulse duration for some tokamaks (TEXTOR, Tore Supra, JET, ITER and a future fusion reactor, DEMO).

A diagram of the principle of an electricity generating fusion reactor is shown in Fig. 1.5. The *D-T* fuel is injected (1) into a chamber where it burns (2). Thus, the reactor produces *ash* (helium atoms) and net energy in the form of fast particles and/or radiation (3). This energy passes through the so-called *"first wall"* made of special components and converted into heat in the *breeding blanket* (4), which is an element behind the first wall but still inside the vacuum chamber. The first wall, blanket and vacuum chamber are intensively cooled by a heat extraction system. The heat is used to produce steam and drive a turbine and alternator electricity producing system (5).

FIG. 1.4. This diagram shows typical values of the thermonuclear fusion power versus pulse duration for some tokamaks. Note the difference in power and pulse length between TEXTOR, JET and Tore Supra, respectively [4].
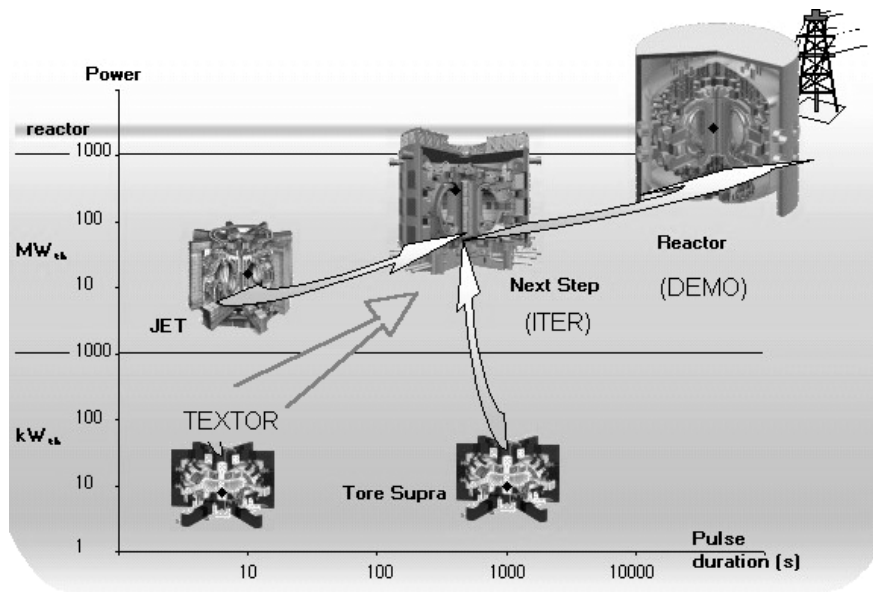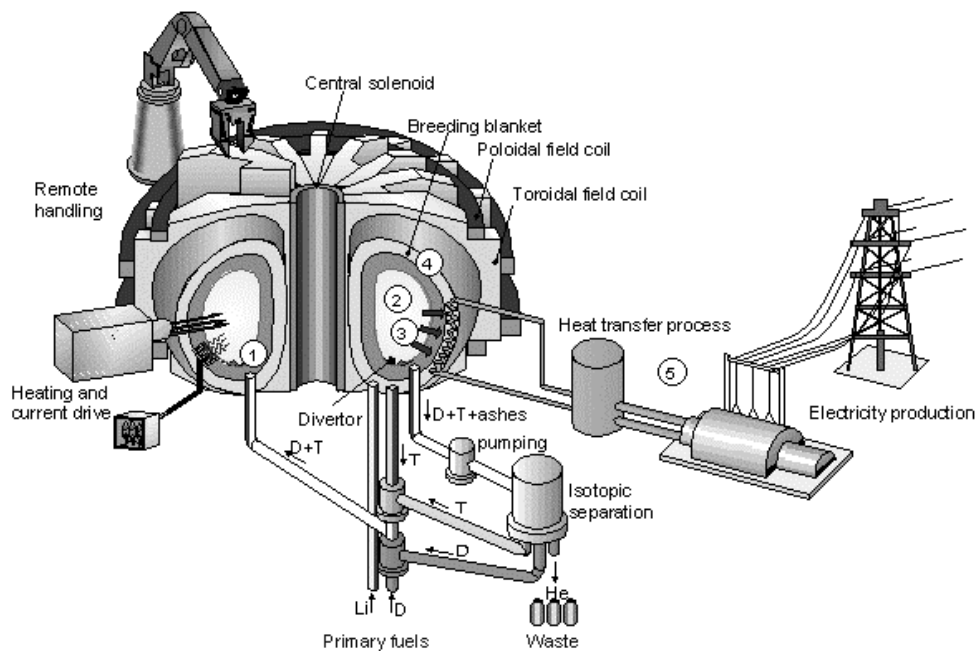

FIG. 1.5. Principle scheme of a D-T fusion power plant. Please refer to the text for the numbers given in this scheme [4].

Table 1.1. Comparison between the main parameters of TEXTOR, JET and ITER.

Parameters	TEXTOR	JET	ITER
Major Radius R_0, m	*1.75*	*3*	*6.21*
Minor Radius a, m	*0.46*	*1.25*	*2.0*
Elongation of Cross-Section	*≈1 (circular)*	*1.6*	*1.8*
Magnetic Field B_φ, T	*< 2.9 (standard operation 2.25)*	*3.4*	*5.3*
Plasma Current I_p, MA	*0.2 – 0.8*	*5 - 7*	*15*
Pulse Duration, s	*< 10*	*10*	*> 300*
Type of Plasma	*H, D*	*D, T*	*D, T*
Additional Heating	*NBI, ECRH, ICRH*	*ICRH, LH, NBI*	*ECRH, NBI,…*

1.3 This thesis

One of the most important problems in tokamak physics is to provide a stable equilibrium with a low diffusion loss of energy and particles. However, it has been found that the particle and energy transport in all tokamaks is much higher than it has been predicted by theory for normal collisional diffusion [7]. Moreover, large instabilities can destroy plasma equilibrium completely and result in a violent discharge termination, called disruption, in which the large heat load can be deposited to the wall of the machine in a very short time interval. Avoidance of disruptions is a very important issue for ITER and future fusion reactors.

Very often, disruptions are caused by an increased Magnetohydrodynamic (MHD) activity in the plasma. Even a relatively small magnetic perturbation can cause the magnetic surfaces to be destroyed and to form so-called magnetic islands. These islands grow and create turbulent regions with enhanced transport of particles and energy. Studies of the MHD stability have been done in different tokamaks all over the world [8, 9, 10]. However, a lack of information about transport properties of the plasma still exists. New sophisticated diagnostics are required for enabling this kind of studies. At TEXTOR, the electron temperature dynamics in the presence of MHD activity in the plasma is studied by means of fast Electron Cyclotron Emission (ECE) diagnostics. The temperature gradients inside and outside the island can be investigated in detail, which can shed some light on the plasma heat flow around and inside the island.

Knowing the rotation properties of the islands, one could possibly think of creating methods that are needed to avoid disruptions or to mitigate their effects. Some theoretical aspects of the MHD island rotation have been treated in [11], and some experimental schemes have become available at TEXTOR [12].

Studies of broadband electron temperature fluctuations are a relatively recent development in plasma physics. This is because of technical difficulties with using dedicated ECE correlation techniques for the correct interpretation of measured data. However, some interesting results obtained at the TEXT-U and RTP tokamaks [13, 14], as well as at the W7-X and TJ-II stellarators [15, 16], have demonstrated the importance of turbulent electrostatic and magnetic fluctuations in explaining the anomalous transport. At TEXTOR, measurements of high-frequency temperature fluctuations, as well as fluctuations that are associated with large MHD islands, have been made and are reported in this thesis.

During disruptions, a large number of fast, or runaway electrons are generated and they can cause a serious damage to the tokamak wall [17, 18]. However, lacking in the interpretation was the experimental information about the lower energetic part of the fast electron distribution function. For that purpose a new ECE diagnostic at TEXTOR has been developed to diagnose these electrons at four different radial locations.

This thesis is organized as follows. A brief introduction into the theory of MHD and microwaves in plasma is given in Chapters 2 and 3, respectively. A description of the diagnostics that were designed and used to obtain the data reported in this thesis, as well as some theoretical aspects of the ECE correlation technique, are given in Chapter 4. Chapter 5 is dedicated to the studies of the plasma transport properties in the presence of MHD modes, as well as to the avoidance and mitigation of disruptions at TEXTOR. First experimental results of the electron temperature fluctuation measurements are given in Chapter 6. Studies of non-thermal electron populations in TEXTOR are reported in Chapter 7. Finally, prospects for further studies are given in Chapter 8.

1.4 List of publications

Below, the list of publications and contributions to conferences and workshops is given. Relevant papers/contributions to this thesis are given in italic.

Journal publications

1. **"New Electron Cyclotron Emission Diagnostics for the TEXTOR Tokamak"**, M.J. van de Pol, V.S. Udintsev, A.J.H. Donné, A. Krämer-Flecken, B.H. Deng, C.W. Domier, N.C. Luhmann Jr., H.K. Park, E. Mazzucato, Fusion Eng. and Design **53**,177 (2001).

2. **"New ECE Diagnostics for the TEXTOR-94 Tokamak"**, V.S. Udintsev, M.J. van de Pol, A.J.H. Donné, J.W. Oosterbeek, A. Krämer-Flecken, Rev. Sci. Instrum., **72**, 359 (2001).
Chapters 4, 6, 7

3. **"Plasma Transport Properties in Presence of MHD Modes Studied by ECE at TEXTOR"**, V.S. Udintsev, B.Ph. Van Milligen, F.C. Schüller, A. Krämer-Flecken, A.J.H. Donné, J.C. van Gorkom, C.W. Domier, and the TEXTOR-Team, accepted for publication in Nucl. Fusion (2003).
Chapters 5, 6

4. **"Heterodyne ECE Diagnostic in the Mode Detection and Disruption Avoidance at TEXTOR"**, A. Krämer-Flecken, K.H. Finken, V.S. Udintsev, H. Larue, and the TEXTOR-Team, accepted for publication in Nucl. Fusion (2003).
Chapter 5

Material presented in *Chapter 6* is being prepared for submission to Physical Review Letters.

Conference/Workshop proceedings

1. **"Large *m/n* = 2/1 Modes Observation in TEXTOR-94 Plasmas"**, V.S. Udintsev, J.C. van Gorkom, A.J.H. Donné, A. Krämer-Flecken, H.J. van der Meiden, J.W. Oosterbeek, M.J. van de Pol, F.C. Schüller, in Proc. of the 27th EPS Conf. on Control. Fusion and Plasma Phys., Budapest, Hungary, Eur. Conf. Abstr. Vol. **24B**, 948 (2000).

2. **"Non-Thermal Electrons in TEXTOR-94 Tokamak Plasmas"**, V.S. Udintsev, R. Jaspers, A.J.H. Donné, A. Krämer-Flecken, J.W. Oosterbeek, M.J. van de Pol, E. Westerhof, in Proc. of the 27th EPS Conf. on Control. Fusion and Plasma Phys., Budapest, Hungary, Eur. Conf. Abstr. Vol. **24B**, 952 (2000).

3. **"Temporal Evolution of Temperature Profiles Inside the Magnetic Islands in TEXTOR-94 Plasmas"**, V.S. Udintsev, A. Krämer-Flecken, J.W. Oosterbeek, B.H. Deng, C. Domier, A.J.H. Donné, E. Graffmann, M.J. van de Pol, F.C. Schüller, in Proc. of the 28th EPS Conf. on Control. Fusion and Plasma Phys., Funchal, Portugal, Eur. Conf. Abstr. Vol. **25A**, 85 (2001).

4. **"Large and Small Scale MHD mode Studies at TEXTOR"**, V.S. Udintsev, B.Ph. van Milligen, F.C. Schüller, A. Krämer-Flecken, B.H. Deng, C. Domier, A.J.H. Donné, J.C. van Gorkom, N.C. Luhmann Jr., in Proc. of the 12th Joint Workshop on ECE and ECRH, p. 215 (Aix-en-Provence, May 13-16, 2002), edited by G. Giruzzi (World Scientific, Singapore, 2002).

5. **"Heterodyne ECE Diagnostic in the Mode Detection and Disruptions Avoidance at TEXTOR"**, A. Krämer-Flecken, K.H. Finken, H. Larue, V.S. Udintsev, in Proc. of the 12th Joint Workshop on ECE and ECRH, p. 197 (Aix-en-Provence, May 13-16, 2002), edited by G. Giruzzi (World Scientific, Singapore, 2002).

6. **"Temperature Fluctuation Measurements in TEXTOR"**, V.S. Udintsev, F.C. Schüller, A. Krämer-Flecken, A.J.H. Donné, F. Castejón, C.W. Domier, in Proc. of the 30th EPS Conf. on Control. Fusion and Plasma Phys., St.-Petersburg, Russia, Eur. Conf. Abstr. Vol. **27A**, P-2.314 (2003).

References

[1] "World Population Prospects: the 1994 Revision", United Nations Population Division, New York (1994); CEA Cadarache Official Web Site, http://www-fusion-magnetique.cea.fr/ (2003).

[2] J. Ongena and G. van Oost, Trans. Fusion Techn. **37**, 3 (2000).

[3] M. Kleemann, Elektrowärme International **49**, Issue A2, A62-70 (June 1991) Vulkan Verlag, Essen (1991).

[4] CEA Cadarache Official Web Site, http://www-fusion-magnetique.cea.fr/ (2003).

[5] J.D. Lawson, Proc. of the Phys. Soc. B **70**, 6 (1957).

[6] A.A. Detlaf, B.M. Yavorskiy, *Course of Physics*, Moscow, Vol. 3, p. 448 (1979) (in Russian).

[7] N.J. Lopes Cardozo, Trans. of Fusion Techn. **37**, 183 (1996).

[8] J. Wesson, *Tokamaks*, Clarendon Press, Oxford (1997).

[9] H. Soltwisch, Plasma Phys. Control. Fusion **34**, 1669 (1992).

[10] F. Salzedas *et al*., Phys. Rev. Lett. **88**, 075002 (2002).

[11] P.C. de Vries *et al*., Plasma Phys. Control. Fusion **39**, 439 (1997).

[12] A. Krämer-Flecken *et al*., in Proc. of the 12th Joint Workshop on ECE and ECRH, p. 197 (Aix-en-Provence, May 13-16, 2002), edited by G. Giruzzi (World Scientific, Singapore, 2002).

[13] C. Watts, R.F. Gandy, Phys. Rev. Lett., **75**, 1759 (1995).

[14] B.H. Deng *et al*., Rev. Sci. Instrum. **72**, 301 (2001).

[15] H.J. Hartfuss, M. Häse, in Proc. of the 10th Joint Workshop on ECE and ECRH, p. 119 (Ameland, April 6-11, 1997), edited by Tony Donné and Toon Verhoeven (World Scientific, Singapore, 1997).

[16] J. Herranz *et al*., Phys. Rev. Lett., **85**, 4715 (2000).

[17] I. Entrop *et al*., Phys. Rev. Lett. **84**, 3606 (2000).

[18] B.C. Schokker, Thesis Technische Universiteit Eindhoven (1996).

Chapter 2

Some theoretical aspects of magnetic islands

In this Chapter, some theoretical aspects of plasma stability in a tokamak will be discussed. Different kinds of instabilities caused by current and density gradients will be introduced.

2.1 Introduction to the magnetohydrodynamic theory

Particle motion in plasma can be described by the kinetic equation (see Chapter 3 for details). One can model plasma as an ionised gas consisting of charged and neutral particles. Generally, thermonuclear plasmas can be characterized as quasineutral, e.g. $\sum_\alpha e_\alpha N_\alpha \approx 0$, where e_α and N_α are charge and concentration of particles of sort α. Plasma can also be modelled as a single fluid (without division between electrons and ions) that conducts electrical current. It is obvious that an external magnetic field can influence the motion of such a fluid, and the theory that describes this motion is called *magnetohydrodynamic (MHD)* theory [1]. A detailed mathematical description of the MHD theory can be obtained from [2, 3]. Below, only a brief introduction is given.

To describe plasma in the resistive MHD model, the Maxwell equations (2.1 - 2.4) are completed with the equations of mass (2.5) and motion (2.6),

$$\nabla \times \vec{B} = \mu_0 \vec{j} + \frac{1}{c^2} \frac{\partial \vec{E}}{\partial t} \ , \tag{2.1}$$

$$\nabla \times \vec{E} = -\frac{\partial \vec{B}}{\partial t} \ , \tag{2.2}$$

$$\nabla \cdot \vec{B} = 0 \ , \tag{2.3}$$

$$\nabla \cdot \vec{E} = \frac{\rho_c}{\varepsilon_0} \ , \tag{2.4}$$

$$\frac{\partial \rho_m}{\partial t} = -\nabla \cdot (\rho_m \vec{v}) , \ \text{ or } \ \frac{d\rho_m}{dt} = -\rho_m \nabla \cdot \vec{v} , \tag{2.5}$$

$$\rho_m \left(\frac{\partial \vec{v}}{\partial t} + \vec{v} \cdot \nabla \vec{v} \right) = \vec{j} \times \vec{B} - \nabla p , \tag{2.6}$$

where $\vec{v}$ is the fluid velocity, μ_0 and ε_0 are the magnetic permeability and the electric permittivity of vacuum, respectively[1], ρ_c is the charge density, and ρ_m is the mass density. If $\frac{d\rho_m}{dt} = 0$, one speaks of incompressible fluid, and $\nabla \cdot \vec{v} = 0$. Neglecting viscosity and taking into account the equations of motion and adiabatic conservation of the internal energy,

---

[1] Values of some physical constants will be given in the Appendix A.

$$\frac{d}{dt}\left(\frac{p}{\rho_m{}^\gamma}\right)=0\ ,\tag{2.7}$$

a model of resistive MHD can be obtained. The resistivity comes in via a generalized Ohm's Law, which can be derived from the subtraction of the momentum equations for the electron- and ion-fluids.

$$\vec{E}=-\vec{v}\times\vec{B}+\eta\vec{j}\ ,\tag{2.8}$$

where η is the resistivity. Taking the curl of Eq. (2.8), one finds as an equivalent expression:

$$\frac{\partial\vec{B}}{\partial t}=\vec{\nabla}\times(\vec{v}\times\vec{B})+\frac{\eta}{\mu_0}\nabla^2\vec{B}\ .\tag{2.8a}$$

The first term at the right hand side gives the change in magnetic field due to convection of field moving with the plasma. The second term gives the change by diffusion of magnetic field driven by gradients and with a diffusion coefficient η/μ_0. In the case of a perfectly conducting plasma ($\eta=0$) the magnetic flux through each surface moving with the fluid is constant. This means that the magnetic flux is "frozen" into this fluid and moves with it.

MHD theory gives a satisfactory description of the plasma fluid in equilibrium as well as in case of instabilities with relatively low frequencies. However, it breaks down if any fast processes, like oscillations with frequencies larger than the ion cyclotron frequency, are present, or if the scale length of the instabilities becomes comparable to or smaller than the ion Larmor radius. That is why Eqs. (2.5 – 2.8a) are often modified to include different types of fluids, for example, electron, ion and/or neutral. These two- and three-fluid models include interaction between particles of different sort and different thermal motion.

2.2 Plasma equilibrium in tokamak

The idealized topology of tokamak plasmas is axisymmetric as shown in Fig. 2.1. The magnetic field lines form nested toroidal surfaces.

In tokamak plasmas without flow, the external pressure of the magnetic field balances the internal plasma pressure. Currents in external magnetic coils determine the plasma position. One can say that the plasma and the magnetic configuration are in *equilibrium*, i.e. the left part of Eq. (2.6) equals to zero:

$$\vec{j}\times\vec{B}=\vec{\nabla}p\ .\tag{2.9}$$

From Eq. (2.9), it follows that:

$$\left.\begin{aligned}\vec{B}\cdot\vec{\nabla}p=0\\ \vec{j}\cdot\vec{\nabla}p=0\end{aligned}\right\}\ .\tag{2.9a}$$

The first equation means that the plasma pressure is constant on magnetic surfaces. From the second one, it follows that the current flows along the magnetic surfaces.
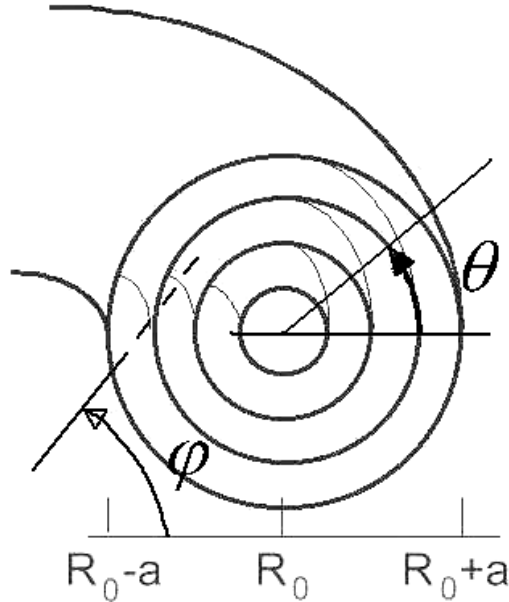
FIG. 2.1. Nested toroidal surfaces in an idealized axisymmetric topology. The toroidal and poloidal coordinates are given as φ and θ, respectively.

When describing the axisymmetric equilibrium, it is convenient to introduce the poloidal magnetic flux function ψ. It is determined by the poloidal flux lying within each magnetic surface and is therefore a constant on this surface [2]. The following equation is valid:

$$\vec{B}\cdot\vec{\nabla}\psi=0 . \tag{2.9b}$$

In a tokamak, the following approximation for the toroidal magnetic field B_φ is often used:

$$B_\varphi(R)\propto\frac{1}{R}, \tag{2.10}$$

where $R = R_0 + r$ is the major radius coordinate and R_0 is the major radius of the centre of the outermost closed flux-surface. A more precise description can be found by introducing the scalar function $f=f(\psi)$:

$$f(\psi)=\frac{RB_\varphi(R)}{\mu_0} . \tag{2.10a}$$

The differential equation for the tokamak equilibrium in terms of the poloidal flux function ψ, resulting from Eqs. (2.9b) - (2.10a), is called the Grad – Shafranov equation:

$$R\frac{\partial}{\partial R}\frac{1}{R}\frac{\partial\psi}{\partial R}+\frac{\partial^2\psi}{\partial z^2}=-\mu_0 R^2\frac{\partial p}{\partial\psi}-\mu_0^2 f(\psi)\frac{\partial f}{\partial\psi} \,. \tag{2.11}$$

The derivation of this equation is given in [2, 4]. From the solution of the Grad – Shafranov equation, a displacement of the centres of the flux surfaces $\Delta(\psi)$ in the direction of the major radius R, with respect to the centre of the outermost flux surface R_0, can be derived. The displacement of the axis is called the Shafranov shift Δ_0. This shift causes that the flux surface ψ does not coincide anymore with the radial coordinate as suggested in Fig. 2.1.

In case of plasma with a circular cross-section like in TEXTOR, one can describe the flux surfaces ψ in terms of modified major radius $R+\Delta(\psi)$ and minor radius r'. For TEXTOR plasmas, $\Delta(\psi)$ is approximated as follows:

$$\Delta(\psi)=\Delta_0\left(1-\left(\frac{r'}{a}\right)^2\right) \,. \tag{2.12}$$

Another parameter that is important in understanding the stability of the tokamak stability is the so-called *safety factor q*. The safety factor is a function of ψ. A geometrical interpretation of the safety factor can be given as follows: it equals to the number of rotations in toroidal direction φ (i.e. along the torus) the magnetic field line needs in order to perform one rotation around the plasma core in poloidal direction θ. Thus, in terms of toroidal and poloidal components of the magnetic field, B_φ and B_θ, the safety factor can be written

$$q(\psi)\cong\frac{1}{2\pi}\int_0^{2\pi}\frac{B_\varphi r'}{R_0 B_\theta(r')}d\theta\approx\frac{B_\varphi r'}{B_\theta(r')R_0}=q_{cyl}(r') \,. \tag{2.13a}$$

Here, q_{cyl} is the approximation of $q(\psi)$ valid for a plasma with a circular cross-section and with aspect ratio $R/a\gg 1$. The poloidal field B_θ is a function of the toroidal current density j_φ. At radius r', it can be expressed using the following relation:

$$B_\theta(r')=\frac{\mu_0}{r'}\int_0^{r'}j_\varphi(r'')r''dr'' \,, \tag{2.14}$$

in which $j_\varphi(r')$ is the toroidal current density, poloidally averaged over the flux surface with the modified minor radius r'. In a tokamak, the radial current density profile $j_\varphi(r')$ can be approximated by the Spitzer resistivity model based on Coulomb collisions between charged particles [6]. A result of such a calculation for typical TEXTOR plasmas will be given in Chapter 5.

If q is rational, Eq. (2.13a) can be re-written as the ratio between two integer numbers m and n:

$$q(r_s) = \frac{m}{n} \ , \tag{2.13b}$$

where r_s is a rational surface. On flux surfaces with a rational q value, field lines close on themselves after m revolutions along the toroidal direction and n revolutions along the poloidal direction. Rational q values play an important role in stability. In the TEXTOR tokamak, q is changing from about $q_0 = 1$ in the plasma centre to values of $q_a = 3 - 5$ at the plasma edge. Some examples of the evolution of rational q surfaces will be given in Chapter 5.

Another important parameter is proportional to the derivative of q: the magnetic field shear Θ. It characterizes the variation in helicity of the magnetic field lines. Shear is an important factor to provide the stability to the closed magnetic configuration in case a resonance perturbation is present. The shear value can be determined as follows [7]:

$$\Theta(\rho) = \frac{\rho}{q} |\frac{dq}{d\rho}| \ . \tag{2.15}$$

To define the efficiency of confining an averaged plasma pressure $<p>$ by the magnetic field in the tokamak, the following dimensionless parameter β is used:

$$\beta = \frac{\langle p \rangle}{\left\langle B^2 / 2\mu_0 \right\rangle} \ . \tag{2.16}$$

As has been discussed in Chapter 1, β plays an important role in fusion experiments [2]. For instance, in a fusion reactor the reaction rate is proportional to $n^2 < \sigma v > \propto n^2 T^2 \propto p^2$ and, therefore, $\propto \beta^2 B^4$. Since the costs of magnetic field coils are dominating the costs of a reactor, it is important to reach the highest β possible. The parameter β strongly influences the behaviour of plasma instabilities, as will be discussed below.

A similar kind of expression can be written for the poloidal β_p. At the plasma edge, it can be determined as [8]:

$$\beta_p = \frac{2\mu_0 \langle p \rangle}{B_{\theta a}^2} \ , \tag{2.17}$$

where $B_{\theta a}$ is the (flux surface averaged) poloidal magnetic field at the edge, and $<p>$ is the pressure averaged over plasma cross-section. Knowledge of the β_p value helps to determine if the plasma is paramagnetic or diamagnetic, with respect to the toroidal field in vacuum. In vacuum, $f(\psi)$ is constant. In case $\beta_p < 1$, the value of $f(\psi)$ increases from the edge of the plasma towards the magnetic axis, i.e. the plasma is paramagnetic with respect to the toroidal field in vacuum. However, if $\beta_p > 1$, the value of $f(\psi)$ decreases from the edge to the centre; i.e. the plasma is diamagnetic. For a typical TEXTOR discharge with an electron density $n_e < 5 \times 10^{19}$ m^{-3}, $\beta_p < 1$ meaning that plasma is paramagnetic. In the Radiative Improved (RI) mode with its high densities, β_p can be above 1, and the plasma has diamagnetic properties. Measurements of β_p allow to estimate) the *energy confinement time* τ_E of ohmically heated plasmas:

$$\tau_E = \frac{W}{P_{OH}} = \frac{3}{8}\mu_0\beta_p\frac{R}{\Omega_{plasma}} \ , \tag{2.18}$$

where W is the total plasma kinetic energy content, P_{OH} is the Ohmic power, and Ω_{plasma} is the plasma resistance. For TEXTOR, τ_E in the Ohmic regime is typically 40 – 60 ms.

2.3   Magnetohydrodynamic modes in tokamak plasmas

In the MHD model, the main destabilizing forces in the tokamak are due to gradients of either the plasma current distribution or of the plasma pressure or of both. The MHD modes can be categorized into *ideal modes*, which would even occur if the plasma would be perfectly conducting, and *resistive modes*, which depend on the finite resistivity of the plasma [2, 9]. In a helical magnetic field, each mode can be characterized by its m and n numbers. In this case, m stands for the number of wavelengths of the modes on the poloidal circumference, and n for the number on the toroidal circumference. It is clear that a geometrical resonance occurs on the magnetic surface where $q(\psi)=m/n$. As has been discussed in Section 2.2, magnetic shear (see Eq. (2.15)) is the main stabilizing factor that provides stability in a closed magnetic configuration against geometrically resonant perturbations. Magnetic field line bending and compression help to stabilize the magnetic configuration. Typical instabilities and their origin are given in Table 2.1. One should realize, however, that under certain conditions, the pressure gradient could influence the growth of the modes driven by the current gradient. Later, some examples will be given.

Table 2.1. Examples of instabilities relevant for TEXTOR plasmas as classified by their origin and category.

	Ideal	*Resistive*
Driven by current gradient	*Kink mode*	*Tearing mode*
Driven by pressure gradient	*Ballooning mode*	
Driven by both gradients	*Internal kink (m=1) mode*	

In this Chapter, MHD modes relevant for TEXTOR plasmas will be discussed. The experimental observation of these modes and their influence on plasma transport properties will be given in Chapter 5.

Ideal kink mode

As noted in Table 2.1, the ideal kink mode is driven by the current gradient. However, at higher β, the pressure gradient will also play a role. The so-called ideal β-limit at high values of β will be discussed later. The name "kink" comes from the fact that this instability tries to kink the magnetic surfaces and the plasma boundary. To describe the stability of the ideal MHD mode, the energy principle is being used: the plasma is unstable if the potential energy δW of the plasma and the magnetic field together is negative for any physically allowable perturbation ξ [2].

If m and n values of the kink mode are low (for example, 2 and 1 respectively), it may appear that it can be resonant with the rational q surface. If the value of q_a equals 2, the plasma configuration will be destroyed by this instability.

Tearing instability and magnetic islands

Since plasma has a finite resistivity, the ideal MHD model will not be valid. Near rational *q*-values, strong gradients in the magnetic field can occur that will lead to diffusion, according to Eq. (2.8). *The tearing instability* can tear magnetic surfaces apart and reconnect magnetic field lines to form *magnetic islands* along the field lines that close on themselves as a form of geometrical resonance. It is convenient to show the geometry of the magnetic field lines in a different coordinate system: *the helical coordinates and their projections*. In this system, one coordinate projection is along the helical magnetic field line that closes on itself on a rational *q*-surface. An angular coordinate is defined to be perpendicular to the helical coordinate projection:

$$\chi = \theta - \frac{n}{m}\varphi \ . \tag{2.19}$$

The equilibrium field close to the magnetic surface can be written as:

$$B_{eq} = -\left(B_\theta \frac{q'}{q}\right)_s z \ . \tag{2.20}$$

Here, $z = r - r_s$, and r_s is the radius of resonance surface, where $q_s = m/n$. For the radial magnetic field perturbation,

$$B_r = \hat{B}_r(r)\sin m\chi \ , \tag{2.21}$$

a differential equation for the field line in the angular coordinates can be written:

$$-\left(B_\theta \frac{\partial q / \partial r}{q}\right)z\,dz = r_s \hat{B}_r \sin m\chi\, d\chi \ . \tag{2.22}$$

Integration of Eq. (2.22) gives the field line equation:

$$z^2 = \frac{w^2}{8}(1 - \cos m\chi\ ) \ , \tag{2.23}$$

where *w* is the so-called width of the magnetic island:

$$w = 4\sqrt{\frac{rq\hat{B}_r}{m \, \partial q / \partial r \, B_\theta}} \ . \tag{2.24}$$

Figure 2.2 illustrates how reconnection of the field lines leads to formation of the magnetic islands. Inside the island, the magnetic field lines lie on a set of helical magnetic surfaces with the magnetic centre indicated as the O-point. The magnetic surface that bounds the island is called the separatrix. Two parts of the separatrix meet at the X-point.
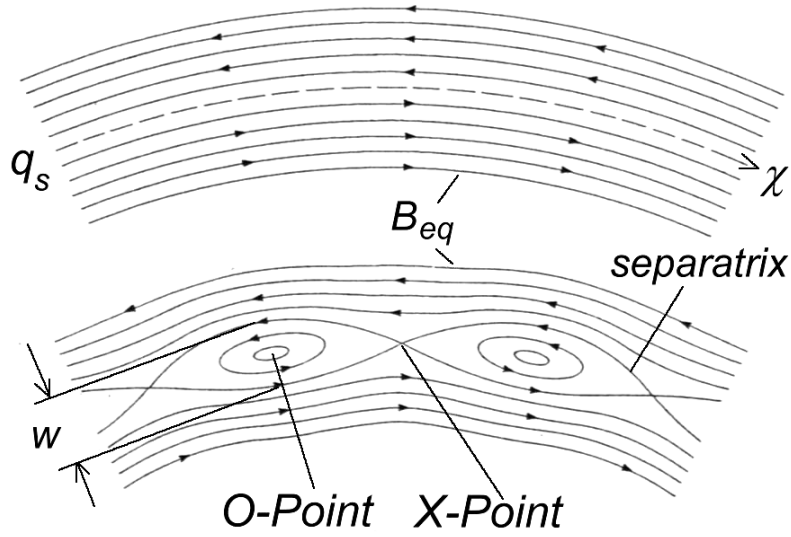
FIG. 2.2. Sketch of a magnetic island in projection of helical coordinates [2]. Graphical definition of the island width is shown. B_{eq} is the unperturbed magnetic field.

Taking the perturbed magnetic component $\vec{B}'$ into account, Eq. (2.8a) can be written in the following form:

$$-\frac{\partial \vec{B}'}{\partial t} + (\vec{B}\nabla)\vec{v} = -\frac{\eta}{\mu_0}\nabla^2 \vec{B}' \; . \tag{2.25}$$

or expressed in the flux coordinate system for the radial component [2]:

$$\gamma\psi + B'_\theta\left(\frac{m-nq}{m}\right)v_r = \frac{\eta}{\mu_0}\nabla^2\psi \; , \tag{2.26}$$

in which γ is the growth rate. As can be seen from Eq. (2.26), the second term in the left part disappears on the rational surfaces.

In the region of the magnetic island, the radial derivative of the perturbed magnetic field is dominant. Integration of Eq. (2.26) together with the matching of the perturbation between the resistive layer and the "ideal" layer outside the separatrix, gives an equation that describes the growth of the island:

$$\frac{dw}{dt} = C_1\frac{\eta}{\mu_0}\Delta' - C_2\alpha w \; . \tag{2.27}$$

In this so-called Rutherford equation, the first term in the right part is the driving term depending on ∇j that is related to the quantity Δ', and the second term gives a stabilizing effect caused by the perturbation of the "ideal" layer. Here, C_1 and C_2 are numerical constants. The influence of other terms on the island growth rate will be discussed in Chapter 5 in detail. In many cases, the second term can be neglected. If so, the tearing mode will be stable if Δ' is negative. Otherwise, it will grow.

The amplitude of the perturbed magnetic field, with respect to the unperturbed, can affect the shape of the magnetic island quite significantly. In Fig. 2.3, examples of the magnetic configuration for different $\hat{B}_r / B_\theta$ are given [7, 10]. It can be seen that a perturbation of 1 – 2% does not change the magnetic configuration too much, but a resonance perturbation of 8% almost destroys it.
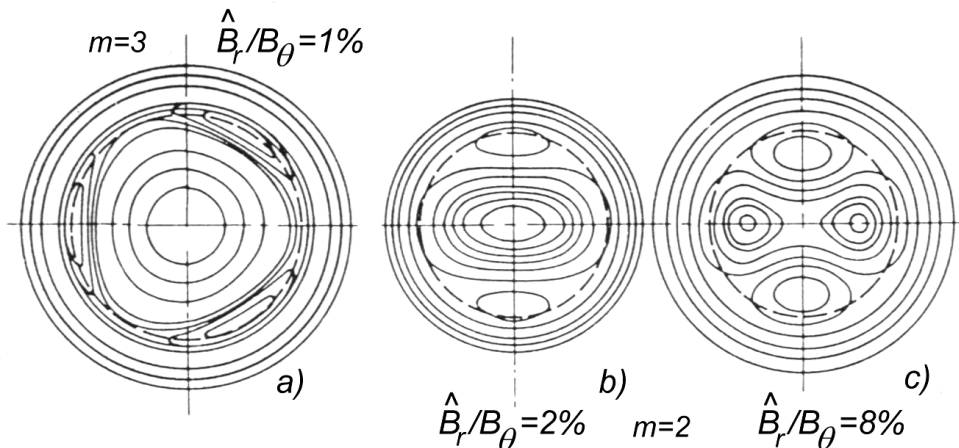

FIG. 2.3. The amplitude of the magnetic perturbation can influence the magnetic configuration. Examples of m = 3 (a) and m = 2 (b, c) islands are given for different $\hat{B}_r / B_\theta$ ratios.

It can be seen that magnetic field lines outside the separatrix form perturbed but unbroken flux surfaces. Since the O-point pushes flux surfaces away, this perturbation is similar to the ideal kink perturbation described earlier. Similar effects might take place in a precursor of the sawtooth crash, which is thought to be an internal kink ($m = 1$, $n = 1$) mode.

Internal $m = 1$ kink mode and unified $m = 1$ theory

This mode has the azimuthal number $m = 1$ and toroidal mode number $n = 1$, so its resonant surface is $q = 1$. This instability is driven by both the pressure gradient and the current density gradient. If $q_0 > 1$, the internal kink mode is stable [2, 7]. Compared to the ideal kink mode, the $m = 1$ internal kink has a displacement which is rigid within the $q = 1$ surface, but is zero outside.

If resistivity is introduced, the instability of the internal $m = 1$ kink is modified. Also pressure gradients can play a role. The theory which analyses all three effects ($\nabla j, \nabla p$ and finite resistivity) together is called *unified m=1 theory*. The result of this theory is a single dispersion relation where all three effects can dominate in different parts of the parameter window. The dispersion relation is given elsewhere in the literature [2] and will not be repeated here. In case the perturbation becomes larger than a critical value, a collapse of the plasma within the $q = 1$ radius takes place together with a reconfiguration of the local magnetic field topology. This is called the "sawtooth crash".

Sawtooth crashes are widely observed in the TEXTOR plasma centre. During the ramp up phase (see Fig. 2.4), heating raises the central temperature and pressure. During the collapse, the thermal energy within the $q = 1$ radius is released to the outer part of the

plasma in the form of a heat pulse. Outside the $q = 1$ surface, the heat pulse propagation appears as an inverted sawtooth on temperature time traces.

As shown in Fig. 2.4, the sawtooth crash has a fast precursor with $m/n = 1/1$ as the dominant mode. Depending on which term dominates in the unified $m = 1$ theory, the internal mode can be caused by either a small magnetic island or by a kink-like deformation both with $m/n = 1/1$. In Chapter 6 measurements will be discussed that points in the direction of a kink-like deformation.
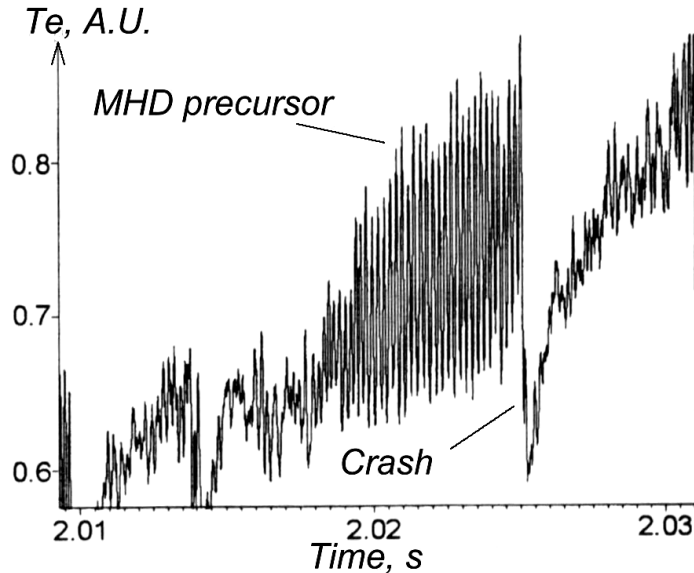

FIG. 2.4. Time trace of a sawtooth precursor in a low density ECR heated discharge at TEXTOR as measured by an ECE-Imaging channel in the equatorial midplane [11].

The most famous model to explain the sawtooth crash has been introduced by B.B. Kadomtsev in 1976 [12, 2]. His model includes a fast magnetic reconnection inside and outside $q = 1$. This reconnection leads to a redistribution of energy and particles and, finally, sets $q_0 > 1$. The evolution of the sawtooth crash by the Kadomtsev model is shown in Fig. 2.5. However, this model cannot explain experimental observations made on different tokamaks. As has been shown for the first time by Soltwisch, q_0 remains below 1 even after a crash [13]. Moreover, according to the Kadomtsev model, the collapse time scales with $r_{q=1}^{3/2}$ and with η^{-1}, where $r_{q=1}$ is the radius of $q = 1$ surface. Based on this, one would expect a longer collapse time for a big tokamak with low resistivity like JET, compared to that on smaller machines with a higher resistivity. However, the experimentally observed collapse times on different sized machines are comparable. Up to now, no reliable model for the sawtooth crash has been introduced.

Modes driven by pressure gradient

Hot plasma with diamagnetic properties is being pushed out towards a lower magnetic field. In ideal MHD, for the magnetic field that decreases to the periphery, magnetic tubes with the hotter plasma (and therefore higher pressure) inside will try to exchange their magnetic field lines with tubes that are adjacent but contain cooler plasma (and therefore lower pressure). This kind of instability is called the *interchange mode*

instability and has been first observed in open magnetic traps [7]. Shear is the stabilizing factor for this instability.
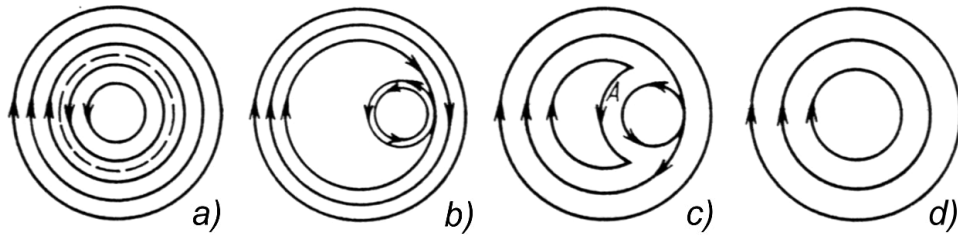

FIG. 2.5. Development of the sawtooth instability following the Kadomtsev model. In the beginning, the q = 1 surface is shown by a dashed line (a). Reconnected flux surfaces form an island (b), and, thus, the magnetic field in the region "A" increases, which leads to the displacement of the q = 1 region (c). This process continues until q is more than 1 (d).

The theoretical stability criterion for a tokamak is called the Mercier criterion [2, 14], which is analogue to the Suydam criterion for cylindrical plasmas:

$$\frac{rB_\varphi^2}{8\mu_0}\left(\frac{\partial q/\partial r}{q}\right)^2 > -\frac{\partial p}{\partial r} + \frac{\partial p}{\partial r}q^2 \ . \tag{2.28}$$

The second term in the right part represents a stabilizing contribution from the *average curvature* of the toroidal magnetic field. The condition of $q > 1$ is enough to stabilize this instability, as long as the pressure gradient is small. However, in high β plasmas interchange modes can develop.

If β is high (1 – 10%), another kind of pressure gradient driven instability with *n* > 1, the so-called *ballooning mode*, can develop at the low field side of the tokamak, where the direction of the pressure gradient is opposite to the direction of the major radius and therefore destabilizing. More information on interchange and ballooning modes can be found elsewhere in the literature [2, 7, and 15].

MHD stability limits. Neoclassical tearing modes

1. The q_a-limit.

Operation of a tokamak can be limited by any of the above-mentioned MHD instabilities. The accessible range is restricted by the fact that the safety factor at the edge, q_a, cannot be smaller than 2. From this, an upper boundary for the plasma current, which depends on the toroidal magnetic field, can be defined.

2. The ideal β-limit.

For a high performance of the tokamak, β defined by Eq. (2.16) has to be large. The maximum pressure that can be confined by a given magnetic field has been calculated by Troyon [16], with ideal MHD instabilities, the Mercier criterion and ballooning modes all taken into account. The stability limit for a given configuration can be written:

$$\beta_{max}^{Troyon} = 0.14 \frac{a}{R_0 q_a} \ .$$ (2.29)

Often, it is more convenient to use the following expression for Eq. (2.29):

$$\beta^* = \beta_N \frac{I}{Ba} \ ,$$ (2.29a)

in which β_N is the so-called normalized β, and I is in MA. According to Troyon, β_N should be 2.8.

In tokamak experiments, however, stationary discharges are limited to a lower value of β [16]. This can be explained by the onset of so-called *neoclassical tearing modes (or NTMs)*.

The growth rate of these modes is described by the generalized Rutherford equation [9, 17]:

$$\frac{\tau_{res}}{r_{m/n}} \frac{dw}{dt} = r_{m/n} \Delta'(w) + r_{m/n} \beta_p \left(a \left(\frac{r_{m/n}}{R_0} \right)^{\frac{1}{2}} \frac{L_q}{L_p} \frac{w}{w^2 + w_0^2} - b \left(\rho_{p,i} \frac{L_q}{L_p} \right)^2 g \left(\frac{r_{m/n}}{R_0} \right) \frac{1}{w^3} \right).$$ (2.30)

In addition to the tearing parameter Δ', two pressure driven parameters are introduced into Eq. (2.30). The first term is destabilizing and originates from the loss of bootstrap current in the island, due to the flattening of the pressure profile. The second term is stabilizing and comes from the polarization current due to the drifts of the ions, when the island moves in the plasma. In Eq. (2.30), the quantities are defined as follows: $\tau_{res} = \mu_0 r_{m/n}^2 / (1.22\eta)$ is the resistive time scale, $r_{m/n}$ is the radius of the rational surface of the mode with numbers *m* and *n*, *a* and *b* are numerical constants, *w* is the island width, $\rho_{p,i}$ is the ion gyroradius in the internal poloidal field, $L_p = p/p'$ and $L_q = q/q'$ are the gradient scale lengths of the pressure and safety factor profiles, and $w_0 \propto (\chi_\perp / \chi_\parallel)^{1/4}$ gives a threshold island width below which the flattening of the profiles and, thus, the loss of bootstrap current is reduced. The function *g* depends on the ion collision frequency normalized to the diamagnetic drift frequency. It should be noted that the NTM develops in the region with a highly reduced collisionality. The interesting properties of the NTMs are that they can grow even if $\Delta' < 0$, and the growth requires a minimum island size, a so-called *seed island.* Such seed island can be created by other independent MHD instabilities like a sawtooth crash that acts as a trigger for the NTM. Figure 2.6 shows electron density and temperature time traces as measured by a far-infrared interferometer and a 3rd harmonic ECE channel, respectively. In this shot, an NTM is present immediately after a sawtooth-like crash has occurred.

NTMs cause a serious limitation of the energy confinement in tokamaks. Stabilization of NTMs (for example, by Non-Inductive Current Drive) will be a very important issue for ITER tokamak [18, 19].

3. Density limit.

If impurity radiation losses at the plasma edge are high, a density limit disruption may occur. If the density is increasing, more energy will be lost by radiation, resulting in a temperature drop at the plasma edge and a change in resistivity. Then, a destabilization of the tearing modes is possible because Δ' becomes positive when the cold radiative layer touches the $q = 2$ surface. The ion effective plasma charge Z_{eff}, which is a measure of the impurity content in the plasma, can strongly influence the impurity radiation losses. By applying additional heating, it is possible to extend the operational range.

Some aspects of disruption avoidance and mitigation will be treated in Chapter 5.
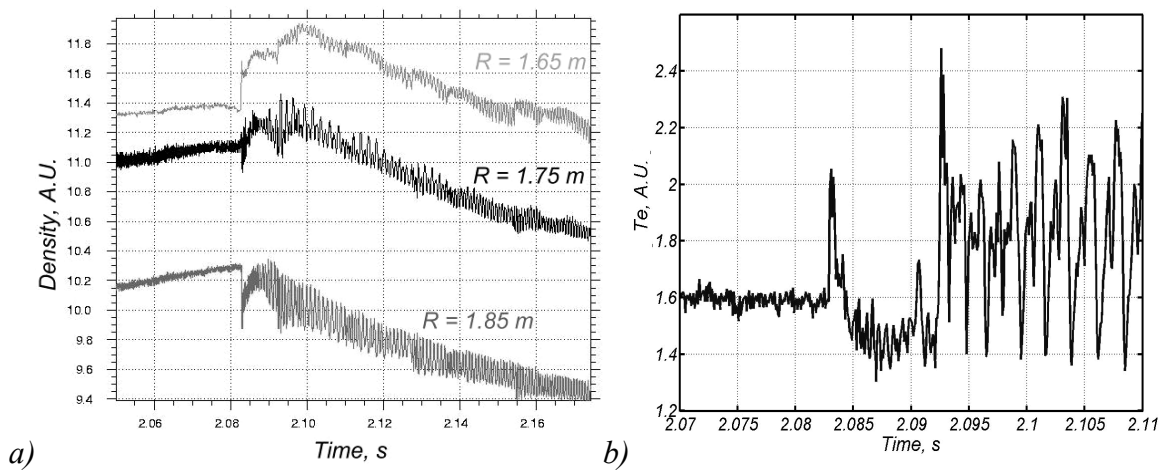

a) b)

FIG. 2.6. An example of the density (a) and temperature (b) time traces, as measured by an interferometer (at three radial positions) and a 3rd harmonic ECE channel, for a TEXTOR shot in which m/n = 3/2. The NTM has been created after a sawtooth-like event at about 2.083 s. At this time, the central density $n_e^0 = 9.5{\times}10^{19}\ m^{-3}$.

References

[1]   D.A. Frank-Kamenetsky, *Plasma, the Fourth Aggregate State*, Moscow (1996) (in Russian).

[2]   J. Wesson, *Tokamaks*, Clarendon Press, Oxford (1997).

[3]   A. Alexandrov, L. Bogdankevitch, A. Rukhadze, *Basics of Plasma Electrodynamics*, Moscow (1978) (in Russian).

[4]   V.D. Shafranov, J. Exper. Theor. Phys. **33**, 710 (1957) (in Russian), Sov. Phys. JETP **6**, 545 (1958).

[5]   H. Soltwisch, Plasma Phys. Control. Fusion **34**, 1669 (1992).

[6]   L. Spitzer, R. Härm, Phys. Rev. **89**, 977 (1953).

[7]   S.V. Mirnov, *Physical Processes in Tokamak Plasmas*, Moscow (1983) (in Russian).

[8]   I.H. Hutchinson, *Principles of Plasma Diagnostics*, Cambridge University Press (1987).

[9]   H.R. Koslowski, Trans. Fusion Technology **37**, 85 (2000).

[10]   D.C. Robinson, K. McGuire, Culham Report CLM-P553 (1979).

[11]   A.J.H. Donné *et al.*, Rev. Sci. Instrum. **72**, 1046 (2001).

[12]   B.B. Kadomtsev, Fizika Plasmy **1**, 710 (1975) (in Russian), Sov. J. of Plasma Phys. **1**, 389 (1976).

[13]   H. Soltwisch, Rev. Sci. Instrum. **59,** 1599 (1988).

[14]   C. Mercier, Nucl. Fusion **1**, 47 (1960).

[15]   V.D. Shafranov, E.I. Yurchenko, J. Exper. Theor. Phys. **3**, 1157 (1967) (in Russian).

[16]   F. Troyon *et al.*, Plasma Phys. Control. Fusion **26**, 209 (1984).

[17]   O. Sauter *et al.*, Phys. Plasmas **4**, 1654 (1997).

[18]   G. Giruzzi *et al.*, Nucl. Fusion **39**, 107 (1999).

[19]   G. Giruzzi, M. Zabiego, Fusion Eng. Design **53**, 43 (2001).

Chapter 3

Principles of ECE

Charged particles in a plasma can be subject to natural oscillations. Charged particles gyrate around the magnetic field lines due to the Lorentz force. This force is always perpendicular to the local magnetic field direction and to the particle velocity vector (see Fig. 3.1). If the particle is an electron, its rotation frequency ω_{ce} is called the *electron cyclotron frequency*:

$$\omega_{ce} = 2\pi f_{ce} = \frac{eB}{\gamma m_e}.$$ (3.1)

Here, f_{ce} is a frequency in Hz, e and m_e are the electron charge (in *Coulomb*) and the rest mass (in *kg*) respectively, B is the absolute value of the local magnetic field in *T*, and $\gamma = 1/\sqrt{1 - v^2/c^2}$ is the relativistic Lorentz factor. For non-relativistic plasmas ($v \ll c$), one can assume γ to be equal to 1.

The radius of the circular rotation is called the *Larmor radius*:

$$\rho_{Le} = \frac{\gamma m_e v_\perp}{eB},$$ (3.2)

where $v_\perp$ is the velocity component perpendicular to $\vec{B}$. Since the electron gyration is periodic, it emits radiation in a series of harmonics:

$$\omega_{cen} = \frac{n\omega_{ce}}{1 - \frac{v_\parallel}{c}\cos\theta}.$$ (3.3)

Here, n is a harmonic number, $v_\parallel$ is the velocity component parallel to $\vec{B}$, θ is the angle between the line of observation and $\vec{B}$. The term $(1 - \frac{v_\parallel}{c}\cos\theta)$ is called *the Doppler shift*. For $\theta \neq 90^0$, one speaks of oblique ECE observation. If $\theta = 90^0$, Eq. (3.3) can be rewritten as:

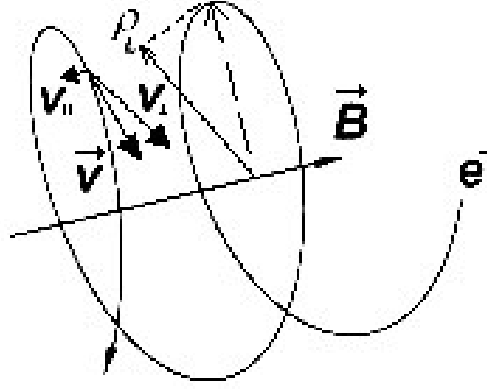$$\omega_{cen} = n\omega_{ce} = 2\pi n f_{ce}.$$ (3.3a)

FIG. 3.1. Gyration of an electron around a magnetic field line. The rotation direction is clockwise, seen in the direction of $\vec{B}$. The Larmor radius is indicated as ρ_L.

In practice, one will always encounter the situation where the Doppler and/or relativistic shift cannot be completely neglected (e.g. because of the antenna pattern). The ensemble of electrons will give a line emission around the frequency given by Eq. (3.3) but shifted and broadened by the velocity distribution. The broadenings of the emission coefficient $j(\omega)$ (see Section 3.2 for details) due to the relativistic and Doppler effects can be approximated by [1]:

$$\Delta f_{cen}^{rel} = nf_{ce}(\frac{v_{Te}}{c})^2 \ , \tag{3.4a}$$

$$\Delta f_{cen}^{Doppler} = nf_{ce}\frac{v_{Te}}{c}|N_r \cos\theta| \ , \tag{3.4b}$$

where N_r is the refractive index. The relativistic effect not only cause a broadening, but also a shift towards lower frequencies[1]. The Doppler broadening has a symmetrical Gaussian shape. The relativistic broadening can be substantial: at TEXTOR, electron temperatures of 5 keV have been created; the relativistic broadening is typically 1 GHz, to be compared to a typical "cold" emission frequency of 100 GHz.

3.1   Dispersion relation

The macroscopic electromagnetic field in the plasma can be described by the Maxwell equations (2.1) – (2.4). For a plasma with the average kinetic energy of its particles much higher than their potential energy, the relation between $\vec{j}$ and $\vec{E}$ can be found from the kinetic equation [2, 3]:

$$\frac{\partial f_\alpha}{\partial t} + \vec{v}\frac{\partial f_\alpha}{\partial \vec{r}} + \frac{e_\alpha}{m_\alpha}\left\{\vec{E} + \frac{1}{c}\left[\vec{v}\times\vec{B}\right]\right\}\frac{\partial f_\alpha}{\partial \vec{v}} = \left(\frac{\partial f_\alpha}{\partial t}\right)_{coll} , \tag{3.5}$$

---

[1] Interpretation of ECE measurements in presence of fast electrons will be given in Chapter 7.

where $f_\alpha(\vec{v},t)$ is the distribution function of the plasma particles of sort α. The term in the right part of the equation describes the change of the distribution function due to collisions and is called the *collision integral*.

The current density for a known distribution function (for example, a Maxwellian) is defined as:

$$\vec{j} = \sum_\alpha e_\alpha \int \vec{v} f_\alpha(v) d\vec{v}. \tag{3.6}$$

To describe the propagation of microwaves through the plasma, often the so-called *cold plasma approximation* is used. In this approximation, the plasma pressure is assumed to be much less than the magnetic pressure (see Eq. (2.16)),

$$\beta << 1, \tag{3.7}$$

and the thermal motion of the particles can be neglected. Under the assumption of a homogeneous plasma and small enough wave fields, the relation between current density and electric field (Ohm's law) can be written as:

$$\vec{j}(\vec{k},\omega) = \sigma(\vec{k},\omega) \cdot \vec{E}(\vec{k},\omega), \tag{3.6a}$$

where $\vec{k}$ is the wave vector, σ is the conductivity of the plasma that is a tensor in case of anisotropic plasma. From the Maxwell equations (2.1 – 2.2) and taking Eq. (3.6a) into account, a *dispersion relation* can be derived [2]:

$$k^2 \vec{E} - \vec{k}(\vec{k}\vec{E}) - (\omega^2/c^2)\vec{D} = 0, \tag{3.8}$$

where $\vec{D} = \bar{\varepsilon}\vec{E}$ is the electrical induction vector, $\bar{\varepsilon}$ is the dielectric tensor (permittivity), $\vec{E}$ is the vector of the wave electric field. In the cold plasma approximation, the dielectric tensor $\bar{\varepsilon}$ can be written in the following matrix form [3]:

$$\bar{\varepsilon} = \begin{bmatrix} \varepsilon & ig & 0 \\ -ig & \varepsilon & 0 \\ 0 & 0 & \eta \end{bmatrix}, \tag{3.9}$$

where $\varepsilon = 1 - \sum_j \dfrac{\omega_{pj}^2}{\omega^2 - \omega_{cj}^2}$, $g = -\sum_j \dfrac{\omega_{pj}^2 \omega_{cj}}{\omega(\omega^2 - \omega_{cj}^2)}$, $\eta = 1 - \sum_j \left(\dfrac{\omega_{pj}^2}{\omega^2} \right)$, j refers to the sort of

particle. If the ion motion is neglected, one gets $\varepsilon = 1 - \dfrac{\omega_{pe}^2}{\omega^2 - \omega_{ce}^2}$, $g = -\dfrac{\omega_{pe}^2 \omega_{ce}}{\omega(\omega^2 - \omega_{ce}^2)}$, and

$\eta = 1 - \dfrac{\omega_{pe}^2}{\omega^2}$. In these equations, the so-called electron and ion plasma frequencies, ω_{pe}

and ω_{pi}, appear. These are natural oscillation frequencies that find their origin in spatial displacements of the electron or ion population with respect to each other. The resulting

charge will pull back these displaced populations, and oscillations occur. For the electrons, it is defined as [4]:

$$\omega_{pe} = \sqrt{n_e e^2 / \varepsilon_0 m_e} \quad , \tag{3.10}$$

where e and m_e are the electron charge and the rest mass respectively, n_e is the local electron density, and ε_0 is the dielectric permittivity in vacuum. Any local perturbation of the electron density, with respect to the undisturbed ion density, will be constrained within the distance called *Debye radius* r_{De}:

$$r_{De} = v_{Te} / \omega_{pe} = \sqrt{\varepsilon_0 T_e / e^2 n_e} \quad , \tag{3.11}$$

where T_e is the electron temperature in *keV*, and v_{Te} is the electron thermal velocity, adopting a Maxwellian electron velocity distribution.

Because the magnetic field geometry and plasma properties in a tokamak are not trivial, the solution of the problem of the wave propagation is a quite complicated task. This problem can be simplified if one assumes that the plasma is homogeneous in a finite local volume, and a *geometrical optics approximation* can be applied. In this approximation, the wave field can be written as:

$$\vec{E}(\vec{r},t) = E(x)\exp(ik_y y + ik_z z + i\int_x k_x(x')dx' - i\omega t), \tag{3.12}$$

where $\vec{E}(x)$ is the wave amplitude and $k_x(x)$ is the projection of the wave vector to the *x* axis. The solution of the dispersion relation (3.8) in this approximation is the so-called *Appleton-Hartree formula* [5]:

$$N_r^2 = 1 - \cfrac{\left(\dfrac{\omega_{pe}}{\omega}\right)^2 \left(1 - \left(\dfrac{\omega_{pe}}{\omega}\right)^2\right)}{1 - \left(\dfrac{\omega_{pe}}{\omega}\right)^2 - \dfrac{1}{2}\left(\dfrac{\omega_{ce}}{\omega}\right)^2 \sin^2\theta \pm \left[\left(\dfrac{1}{2}\left(\dfrac{\omega_{ce}}{\omega}\right)^2 \sin^2\theta\right)^2 + \left(1 - \left(\dfrac{\omega_{pe}}{\omega}\right)^2\right)^2 \left(\dfrac{\omega_{ce}}{\omega}\right)^2 \cos^2\theta\right]^{\frac{1}{2}}}. \tag{3.13}$$

One should, however, note that the cold plasma approximation fails close to the position where the wave becomes resonant. For $N_r^2 < 0$, the plasma is opaque for the microwaves, and the value of N_r^2 determines the depth of the wave penetration layer (the so-called *skin layer*): $\delta \sim c / \omega |N_r|$. For $N_r^2 > 0$, there are five wave branches that exist in a magnetized plasma.

Two wave types can be distinguished with propagation vector parallel or perpendicular to the wave electric field. The first is of electrostatic and the second is of electromagnetic nature. Let us first discuss the **perpendicular propagation** ($\vec{k} \perp \vec{B}_0$, $\theta = 90^0$) of the waves of both origins.

In the case of electrostatic waves, with the wave vector $\vec{k}$ parallel to the wave electric field vector $\vec{E}$, waves have a resonance at:

$$\omega_{UH}^2 = \omega_{pe}^2 + \omega_{ce}^2 \ , \tag{3.14}$$

where ω_{UH} is the so-called *Upper Hybrid resonance* frequency. Another kind of electrostatic oscillation in the plasma may be resonant at the so-called *Lower Hybrid resonance* frequency ω_{LH} :

$$\omega_{LH}^2 = \omega_{ce}^2 \omega_{ci}^2 \left(1 + \frac{\omega_{ci}^2}{\omega_{pi}^2} \right) \bigg/ \left(1 + \frac{\omega_{ce}^2}{\omega_{pe}^2} \right), \tag{3.15}$$

where ω_{ci} and ω_{pi} are the ion cyclotron resonance and plasma frequencies, respectively.

For electromagnetic waves propagating perpendicular to the magnetic field but with the polarization of the electric field is parallel to the magnetic field (e.g., $\vec{k} \perp \vec{E} \parallel \vec{B}_0$), the dispersion relation (3.13) can be written as:

$$N_r^2 = \frac{c^2 k^2}{\omega^2} = 1 - \frac{\omega_{pe}^2}{\omega^2} \ , \tag{3.16}$$

which is similar as for the case when $B_0 = 0$. This type of wave is called *Ordinary mode*, or simply *O-mode*. A cut-off for the O-mode occurs when $\omega = \omega_{pe}$ ($N_r^2 = 0$), so an O-mode wave with a lower frequency cannot propagate through the plasma. This wave mode does not depend on the magnetic field.

If the polarization of the electric field is perpendicular to the magnetic field ($\vec{k} \perp \vec{E} \perp \vec{B}_0$), $\vec{B}_0$ influences the electron motion. The dispersion relation (3.13) in this case is given by:

$$N_r^2 = 1 - \omega_{pe}^2 (\omega^2 - \omega_{pe}^2) / \omega^2 (\omega^2 - \omega_{UH}^2) \ , \tag{3.17}$$

This is the so-called *eXtraordinary mode*, or *X-mode*, which depends amongst others also on the magnetic field. When $N_r \to \infty$ ($k \to \infty$), this mode has a resonance at ω_{UH} . Cut-off frequencies (when $N_r \to 0$) can be defined as follows:

$$\omega_\pm = \frac{1}{2} \left[\pm \omega_{ce} + \left(\omega_{ce}^2 + 4\omega_{pe}^2 \right)^{\frac{1}{2}} \right]. \tag{3.18}$$

Here, ω_+ and ω_- are the upper and lower cut-off, respectively.

The resonance and cut-off frequencies split the X-mode into two branches, the fast and the slow X-mode. At the cut-off frequencies, waves cannot propagate through the plasma and will be reflected. At the resonance frequencies, they could be absorbed, but also they can be converted to so-called Electron Bernstein waves (EBW) before they reach the resonance location [6]. This conversion is strongly dependent on density, temperature and local magnetic field. However, this type of waves is not relevant for any measurements described in this thesis. In Fig. 3.2, the dependence of the squared refraction index for wave propagation perpendicular to the magnetic field ($\theta = \pi/2$) is shown. The dispersion diagram for several wave branches is given in Fig. 3.3.

For **wave propagation parallel** to the magnetic field ($\vec{k} \parallel \vec{B}_0, \theta = 0^0$), one gets two possible solutions. If the polarization of the electric field is perpendicular to the magnetic field ($\vec{E} \perp \vec{B}_0$), the dispersion relation can be written as:

$$N_r^2 = 1 - \frac{\omega_{pe}^2 / \omega^2}{1 - \omega_{ce}/\omega} \quad \text{(R-wave)}, \qquad (3.19)$$

$$N_r^2 = 1 - \frac{\omega_{pe}^2 / \omega^2}{1 + \omega_{ce}/\omega} \quad \text{(L-wave)}, \qquad (3.20)$$

where the R-wave and L-wave are so-called *right-handed* and *left-handed circularly polarized waves*, respectively [7]. Since the R-wave is rotating in the same direction as the plasma electrons, it has its resonance frequency at ω_{ce} and the cut-off at $\omega = \omega_+$. For the L-wave, a cut-off occurs at $\omega = \omega_-$. A schematic view of the different wave types in plasma is shown in Fig. 3.4.
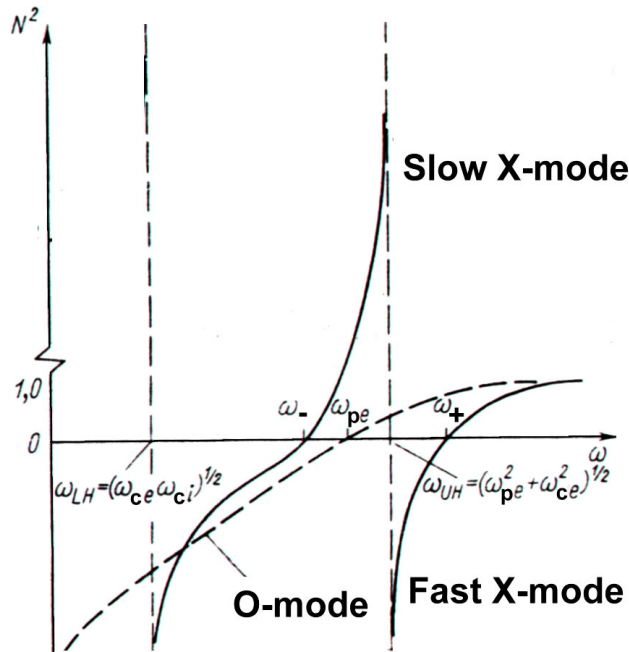

FIG. 3.2. The dependence of the squared refraction index on the frequency for $\theta = \dfrac{\pi}{2}$ *[7].*

For the polarization of the electric field parallel to the magnetic field ($\vec{E} \parallel \vec{B}_0$), one gets an electrostatic plasma oscillation with frequency ω_{pe}.
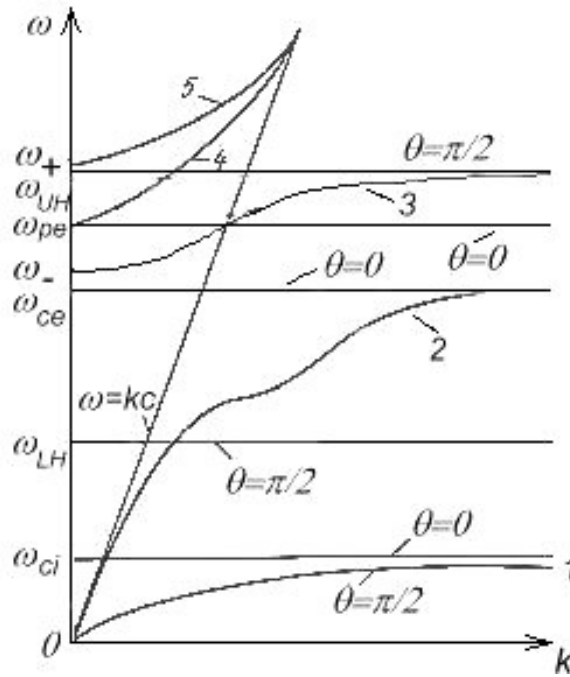
FIG. 3.3. The dispersion diagram for several wave branches, two ordinary (1,4) and three extraordinary modes (2,3,5) are shown [7]: 1, 2 – Alfven and fast magnetosonic, respectively (given for a general reference only), 3 – slow extraordinary, 4 – fast ordinary, 5 – fast extraordinary. Two extreme cases are given, for perpendicular ($\theta = \pi/2$) and parallel ($\theta = 0$) wave propagation, with respect to the magnetic field.
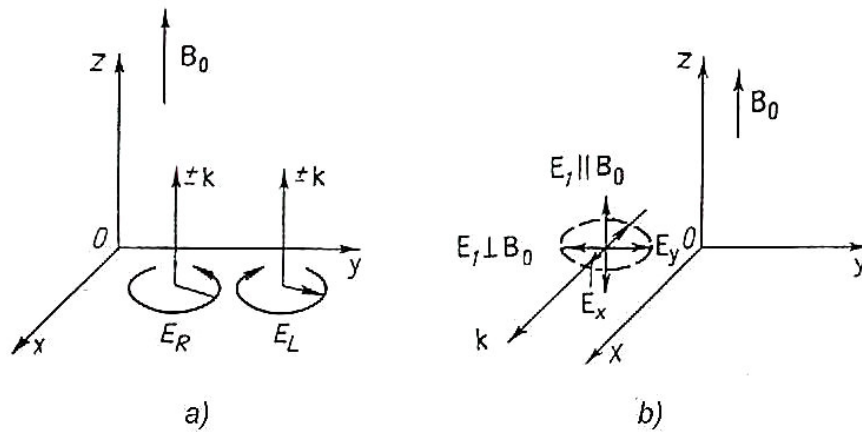

FIG. 3.4. Schematic view of the different wave types in the plasma for parallel ($\vec{k} \parallel \vec{B}_0$, $\theta = 0^0$) (a) and perpendicular ($\vec{k} \perp \vec{B}_0$, $\theta = 90^0$) (b) propagation, with respect to the external magnetic field B_0 [7].

3.2 Wave accessibility in TEXTOR plasmas

The differential radiation transport equation for a single ray, which takes the emission and absorption along an observation line into account, can be written in the following form [8]:

$$\frac{d}{ds}\left[\frac{I(\omega)}{N_r^2}\right] = \frac{1}{N_r^2}\left[-\alpha(\omega)I(\omega) + j(\omega)\right], \tag{3.21}$$

where N_r is the plasma ray refractive index described above, $I(\omega)$ is the ECE intensity, $\alpha(\omega)$ is the absorption coefficient, $j(\omega)$ is the emission coefficient, s is a coordinate along the ray trajectory throughout the plasma volume. For a proper analysis of ECE data, the determination of the absorption coefficient $\alpha(\omega)$ and the emission coefficient $j(\omega)$ is important. The spontaneous emission coefficient η of a single electron perpendicular to the magnetic field is given by the Schott-Trubnikov formula [9]:

$$\eta_n(\omega) = \frac{e^2\omega^2}{8\pi^2\varepsilon_0 c}\left[\beta_\parallel^2 J_n^2(n\beta_\perp) + \beta_\perp^2 J_n'^2(n\beta_\perp)\right]\delta(\omega_n - \omega), \tag{3.22}$$

where J_n and J_n' are the Bessel function of the nth order and its derivative, n is the harmonic number of the ECE radiation, $\beta_\parallel = v_\parallel/c$ and $\beta_\perp = v_\perp/c$ are normalized velocities parallel and perpendicular to the magnetic field, and γ is the relativistic factor (see Eq. 3.1). The first and the second terms in brackets are for the O- and X-mode ECE, respectively. An integration of Eq. (3.22) over the electron distribution function $f(\vec{v},\vec{r})$ gives the following relation for the emission coefficient:

$$j(\omega) = \sum_n \int d\vec{v} f(\vec{v},\vec{r})\eta_n(\omega). \tag{3.23}$$

Integration of Eq. (3.21) along the ray trajectory gives the amount of radiation from the plasma at frequency ω:

$$I(\omega) = I_{incident}(\omega)e^{-\tau} + Q(\omega)(1 - e^{-\tau}). \tag{3.21a}$$

Here, $I_{incident}(\omega)$ is the intensity of incident radiation at the start point of the ray trajectory, $Q(\omega)$ is the emission intensity from the source, $\tau = \tau(\omega) = \int_s \alpha(\omega)ds$ is the so-called *optical thickness*, or *optical depth*. If the plasma is Maxwellian and optically thick ($\tau \gg 1$), its emission can be described by the equation for black body radiation in the Rayleigh-Jeans limit:

$$I_{BB}(\omega, T_e) = \frac{\omega^2}{8\pi^3 c^2}k_B T_e, \tag{3.24}$$

where k_B is the Boltzmann constant, T_e is the electron temperature. This is the base for using ECE for the electron temperature measurements.

One should realize, however, that the plasma in a tokamak is not always optically thick: for example, TEXTOR plasmas are almost always optically thick for the 2nd harmonic ECE radiation, but optically thin ($\tau \leq 1$) for the 3rd harmonic radiation. For optical thin radiation one should realize that microwaves can be reflected from the tokamak walls, so the wall reflection coefficient ρ_{refl} should be taken into account giving a contribution to $I_{incident}$ in Eq. (3.21a):

$$I(\omega,T_e)=I_{BB}\frac{(1-e^{-\tau})}{(1-\rho_{refl}e^{-\tau})}=\frac{\omega^2}{8\pi^3c^2}k_BT_e\frac{(1-e^{-\tau})}{(1-\rho_{refl}e^{-\tau})} \ . \tag{3.25}$$

Generally, the optical thickness τ is a function of the local temperature and density, as well as the wave polarization and the tokamak geometry. For a circular tokamak geometry (major radius R_0, minor radius a, observation in X-mode under $\theta = 90^0$ in the equatorial plane), and for a magnetic field B_φ which is strongly dominated by the vacuum toroidal magnetic field, $B_\varphi(R) = B_{\varphi 0}R_0 / R$, the value of τ can be approximated as [1]:

$$\tau_n^X = 9.5\cdot 10^{12}\frac{(R_0 + r)^2 n_e\left[n^{2n-2}(9.78\cdot 10^{-4}T_e)^{n-1}\right]}{10R_0B_\varphi(R)(n-1)!} \ , \tag{3.26}$$

where $n \geq 2$ is the harmonic number, r is the radial ($-a \leq r \leq a$) position in cm, T_e and n_e are the local electron temperature in keV and density in cm^{-3} respectively.

For the 1st harmonic O-mode, the optical thickness can be approximated as:

$$\tau_{n=1}^O = 9.8596\frac{1.16\cdot 10^4 k_BT_e}{m_ec^2}\frac{R_0\omega_{ce}}{2\pi c}\frac{\omega_{pe}^2}{\omega_{ce}^2}\sqrt{1-\frac{\omega_{pe}^2}{\omega_{ce}^2}} \ . \tag{3.27}$$

Some typical values of $\tau_{n=2,3}^X$, as well as the optical thickness for the 1st harmonic O-mode for the different plasma parameters in TEXTOR, are given in Fig. 3.5.

In Fig. 3.6, the wave frequencies for the different harmonics of ECE radiation are given for the same plasma parameters in TEXTOR as in Fig. 3.5. The 1st harmonic X-mode is not accessible in any tokamak due to the upper cut-off at ω_+. For the case that ECE radiation is measured at the Low Field Side (LFS)), the radiation at the 2nd harmonic X-mode can be used to evaluate the electron temperature at different plasma positions, provided that the electron density is not too high. Otherwise, the wave frequency becomes lower than ω_{pe}, and the cut-off is reached (dark shaded areas in Fig. 3.6). One should also take into account that there is a certain frequency range limit due to the 2nd and 3rd harmonics overlap at the higher frequencies (light shaded). The 3rd harmonic ECE is also available for detection, although one always needs to correct the measured radiation temperature for the optical thickness and wall reflections. In TEXTOR, only 2nd and 3rd harmonic X-mode ECE radiation is being used for the electron temperature measurements.

It is also necessary to mention that fast (non-thermal) electron populations with energies up to tens of keV can significantly change the ECE measurements. These non-thermal electrons appear in the low-density ($n_e < 10^{19}$ m^{-3}) regimes in TEXTOR, and their effect can be enhanced by the additional heating methods, such as Electron Cyclotron Resonance Heating (ECRH), Neutral Beam Injection (NBI) and Ion Cyclotron Resonance Heating (ICRH). The velocity distribution for these electrons deviates from a Maxwellian,

and they show a high-energy tail in the velocity distribution. The emission from the non-thermal electrons is downshifted to lower frequencies or, in different words, contributes to the emission at frequencies resonant at the LFS of the tokamak. In this case, ECE diagnostics measure the radiation temperature T_e^{rad}, which consists of both the local thermal and non-local non-thermal radiation. If the local optical thickness is high enough, i.e. in practice when $n_e > 10^{19} m^{-3}$, the latter contibution is absorbed and T^{rad} becomes equal to the local T_e.

Detailed analysis of the ECE emission spectra in presence of non-thermal electrons will be given in Chapter 7.
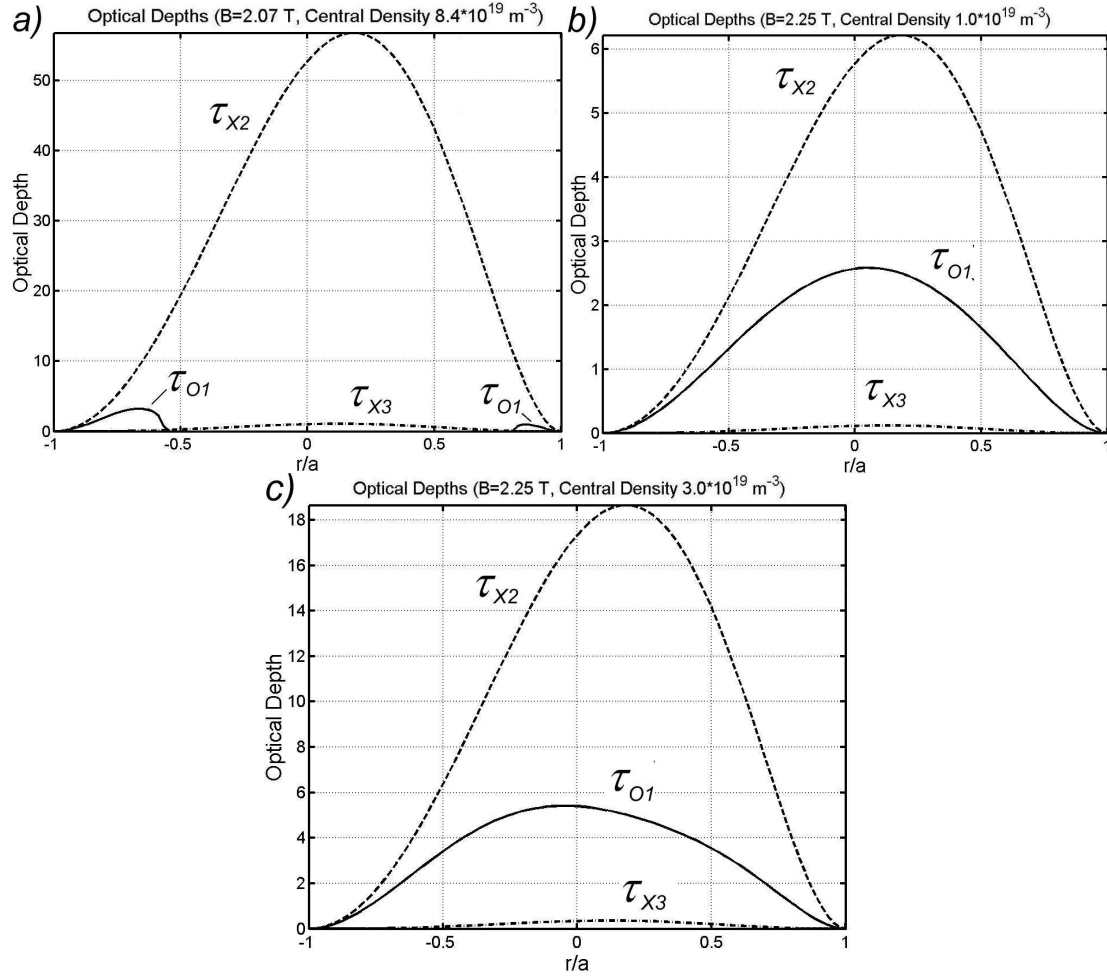

FIG. 3.5. Optical thickness τ as a function of the normalized minor radius for the 2nd and 3rd harmonic ECE X-mode and the 1st harmonic O-mode for different TEXTOR plasma parameters. Here, a) is a Radiative Improved (RI)-mode regime with $B_0 = 2.07$ T and a central electron density $n_{e0} = 8.4 \cdot 10^{19}$ m^{-3}, b) is a low density "slide-away" discharge with $B_0 = 2.25$ T and $n_{e0} = 1 \cdot 10^{19}$ m^{-3}, c) is the "standard" TEXTOR Ohmic regime with $B_0 = 2.25$ T and $n_{e0} = 3 \cdot 10^{19}$ m^{-3}. For all cases, a central electron temperature $T_e^0 = 2$ keV is assumed.
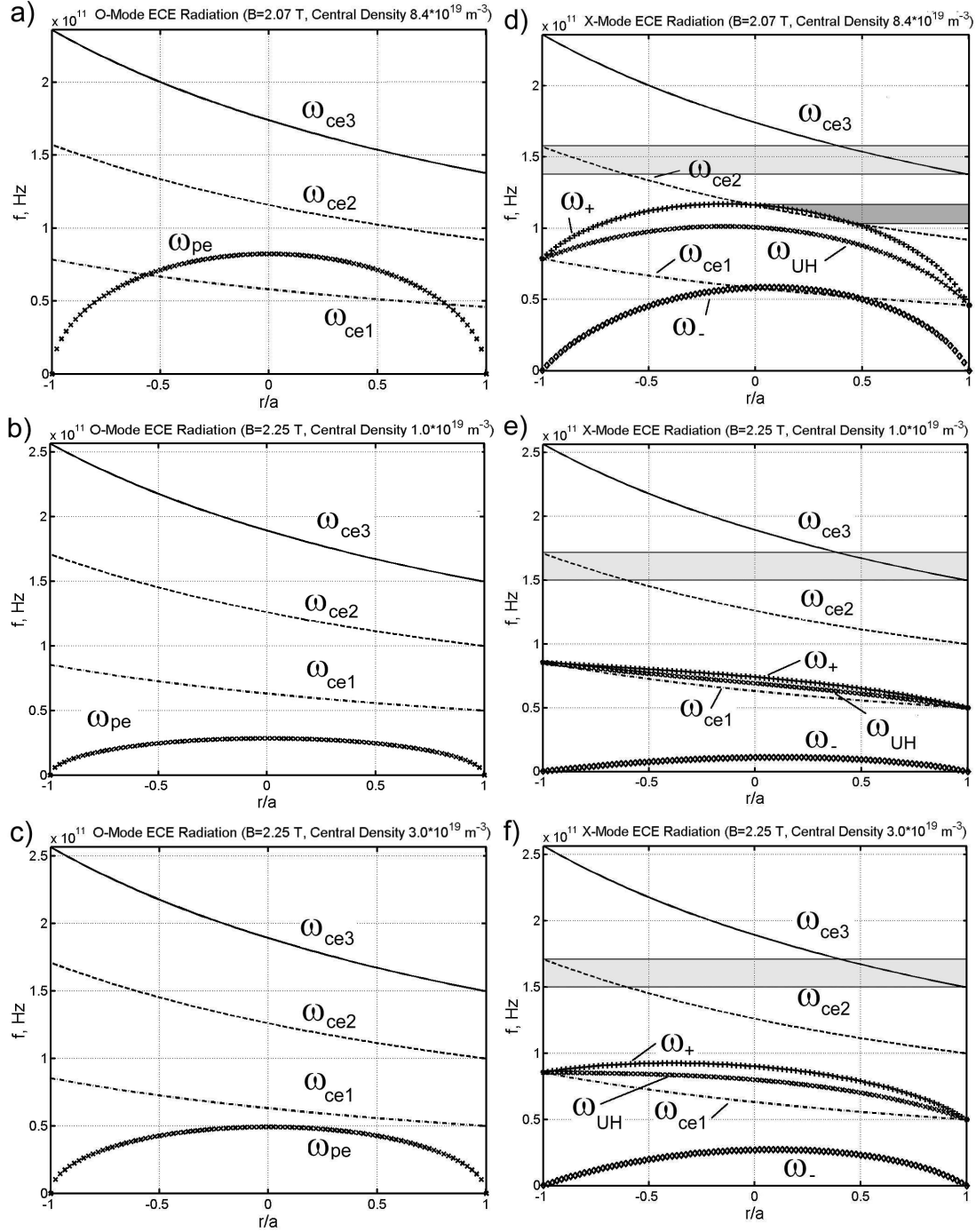
FIG. 3.6. Typical resonance and cut-off frequencies for the same TEXTOR plasma parameters as in Fig. 3.5: a), b) and c) – for the O-mode radiation, d), e) and f) – for the X-mode radiation. Frequency overlap between 2nd and 3rd harmonics (light shaded) and the cut-off range for the 2nd harmonic (dark shaded) are shown only for the X-mode. For these calculations, a parabolic density profile is assumed.

References

[1]   M. Bornatici *et al*., Nucl. Fusion **23**, 1153 (1983).

[2]   V. Golant, V. Fedorov, *RF Plasma Heating in Toroidal Fusion Devices*, Consultants Bureau, New York (1989).

[3]   L. Spitzer, *Physics of Fully Ionized Gases*, Interscience Publishers Ltd., London (1956).

[4]   L. Artsimovitch, R. Sagdeev, *Plasma Physics for Physicists*, Moscow (1975) (in Russian).

[5]   E.V. Appleton, J. Inst. Elect. Eng. (London) **71**, 642 (1932).

[6]   G. Taylor *et al*., in Proc. of the 12th Joint Workshop on ECE and ECRH, p. 4 (Aix-en-Provence, May 13-16, 2002), edited by G. Giruzzi (World Scientific, Singapore, 2002).

[7]   I. Gekker, *Strong Electromagnetic Fields in Plasma*, Moscow (1988) (in Russian).

[8]   G. Bekefi, *Radiation Processes in Plasmas*, John Wiley & Sons Inc., New York (1966).

[9]   B.A. Trubnikov, Doklady Sov. Phys. **3**, 136 (1958).

Chapter 4

ECE on TEXTOR

The TEXTOR tokamak (R_0 = 1.75 m, a = 0.46 m, B_t < 2.9 T) is equipped with a wide variety of diagnostics. Plasma core parameters are amongst others measured by means of various microwave and Soft X-Ray (SXR) diagnostics, as well as by a high-resolution multi-point Thomson Scattering (TS) system. Microwave diagnostics, like Electron Cyclotron Emission (ECE) systems and reflectometers, allow us to study the electron temperature and density evolution in time with a good spatial and temporal resolution. ECE diagnostics will be widely used for the analysis in this thesis. They will be described in detail in this Chapter. Also, a short description of the Thomson scattering system and the reflectometers will be given. In the end, some aspects of temperature fluctuation measurements in hot magnetized plasma by means of the correlation ECE technique will be treated.

4.1   Diagnostics set-up

ECE diagnostics on TEXTOR cover the frequency range of 98 − 180 GHz. There are two heterodyne radiometers, three fast spectrometers, one vertical imaging system, and a combined 2nd-3rd harmonic radiometer available for extensive ECE radiation measurements. A detailed description of the various systems is given below. Their main parameters are given in Table 4.1.

4.1.1 11-channel heterodyne radiometer and fast spectrometers

Electron temperature profiles at TEXTOR are routinely measured by an 11-channel heterodyne radiometer, which diagnoses the 2nd harmonic X-mode in the frequency range from 105 to 145 GHz (see Fig. 4.1). ECE emission is received from the Low Field Side (LFS) and the High Field Side (HFS) by separate antennas. This has been done in order to avoid the 2nd and 3rd harmonics overlap at the HFS, as has been described earlier. The LFS horn and the HFS parabolic antennas are located 2 cm below and exactly in the equatorial plane, respectively. The IF bandwidth of each channel is 200 MHz, and the sampling rate is up to 25 kHz (but by default it is 10 kHz). This radiometer is absolutely calibrated by means of a hot source.

Two fast 6-channel spectrometers (104 - 114 GHz and 125 − 130 GHz) are using a parabolic antenna. A third 6-channel spectrometer (133 − 148 GHz) is using a horn antenna at the same toroidal location as the 11-channel radiometer, but 2 cm above the equatorial midplane. The sampling rate of these systems can be up to 2 MHz, although, for most measurements this value is typically set to 50 kHz. The spectrometers make it possible to study m = 2 and m = 1 modes both at the HFS and the LFS, and are cross-calibrated versus the 11-channel radiometer. Both the 11-channel radiometer and the fast spectrometers are described in detail in [1].

Table 4.1. ECE diagnostics at TEXTOR.

	T_e-Profile Radio-meter	Spectro-meters	2nd/3rd Har-monic Radio-meter	16-Channel Tunable Radio-meter	ECE-Imaging Vertical System
# channels	11	3 x 6	4/4	16	16
Frequency range (GHz)	105, 107, 109, 112, 115 (5)* 145	104 (2) 114 125 (1) 130 133 (3) 148	111-120 166 - 180	98 (3) 146	114
IF band-width (MHz)	200	200 400	200	200 450	550
Typical Sampling rate (kHz)	10	25-1000	10	100-2000	100-2000

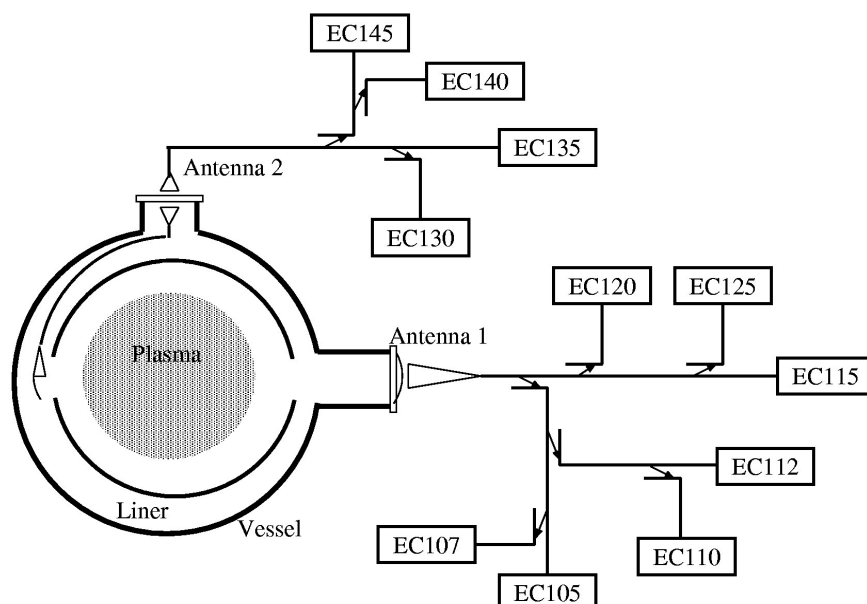* In brackets, a step in frequency is shown.

FIG. 4.1. Schematic view of the 11-channel radiometer at TEXTOR.

4.1.2 The combined 4-channel second-third harmonic radiometer

The main ECE diagnostic tool for fast electron measurements on TEXTOR is a new combined second (110.7, 113.3, 116.7, and 120 GHz) and third (166, 170, 175, and 180 GHz) harmonic X-mode system. This allows simultaneous measurement of second and third harmonic radiation from four radial positions in the plasma. The spectral bandwidth of each channel is 200 MHz. Qualitative information about the velocity distribution of non-thermal electrons can be obtained from a comparison of the optically thick second and optically thin third harmonic spectra. This radiometer can in principle be used to measure temperature fluctuations by correlation techniques, provided their frequency is below 5 kHz (see Section 4.2.1).

The plasma millimetre-wave emission is received by a parabolic antenna located in the equatorial plane at the LFS of the vacuum vessel. To avoid reflections from the opposite wall, graphite beam dumps are used. A notch filter at 110 GHz is installed to protect the mixers from gyrotron radiation used for Electron Cyclotron Resonance Heating (ECRH) (Fig. 4.2). A 10 dB directional coupler with an insertion loss of less than 1.3 dB is used to separate the RF power between the second harmonic and the third harmonic branch. Since both systems view the plasma through the same antenna, and because the frequencies of the second harmonic systems are exactly 2/3 of those of the third harmonic system, they observe the same electron population.
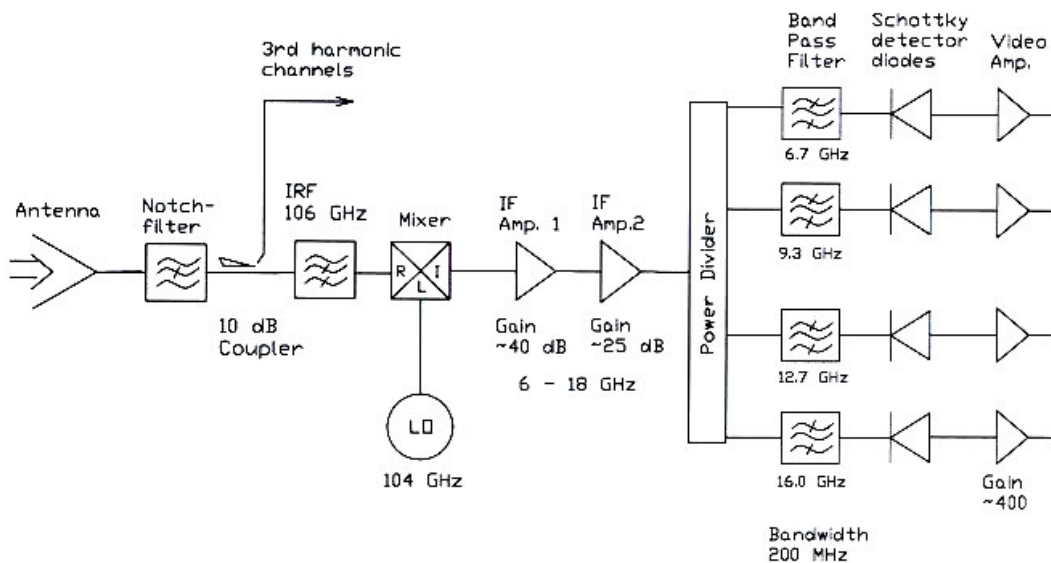

FIG. 4.2. Second harmonic branch of the four-channel heterodyne ECE radiometer.

The power coupled to the second harmonic section is passed through an image rejection (high pass) filter (IRF) (106 GHz) to suppress the lower side band. Then it is fed to a double-balanced mixer, where it is down converted by means of a 104 GHz Gunn oscillator (10 mW output) to an IF-band of 6-18 GHz. Two cascaded IF amplifiers provide a total IF gain of about 65 dB. The intermediate signals are split in to four branches using a power divider (insertion loss is about 7 dB), then it is band-pass filtered to IF frequencies of 6.7, 9.3, 12.7 and 16 GHz with a bandwidth of 200 MHz. After that, the signals are fed to Schottky diodes for detection. The resulting signal is conditioned by video amplifiers

with a gain of 400 and a bandwidth of 10 kHz. The principal scheme for different filter types is given in Fig. 4.3 [2].

The receiver noise temperature [3] was measured to be about 1.5 eV, in agreement with the calculations:

$$T_r = \frac{T_{hot} - YT_{cold}}{Y - 1} \approx 18000 \text{ K} \approx 1.5 \text{ eV}, \tag{4.1}$$

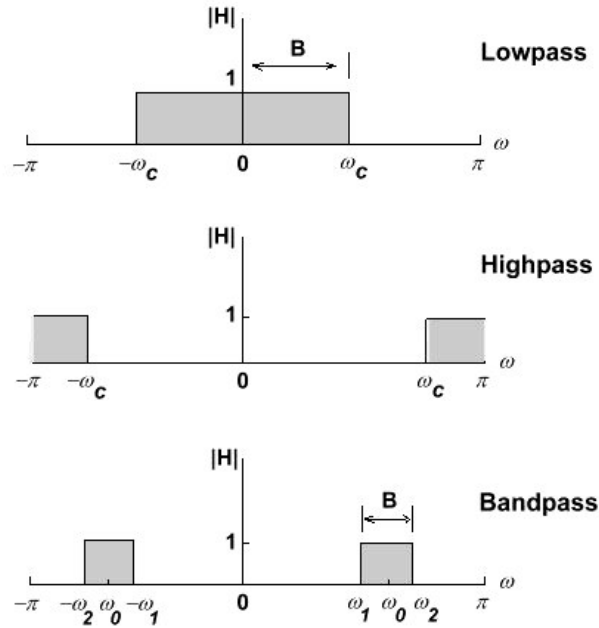where T_{hot} = 300 K, T_{cold} = 77 K (Li N_2), Y = P_{hot} / P_{cold} = 1.012.

FIG. 4.3. Magnitude responses |H| for some ideal frequency-selective filters: lowpass, highpass and bandpass. "Passing" frequencies are shaded [2].

Although a cross-calibration is made with respect to the absolutely calibrated 11-channel heterodyne radiometer for every discharge, the minimum detectable electron temperature with the four-channel second harmonic system is typically several tens of eV. The reason for this is that the noise temperature of the total system increases by the losses in the front end, which were not included in the measurements of the noise temperature.

4.1.3 The 16-channel frequency tuneable heterodyne radiometer

The main part of this diagnostic is derived from the 20-channel radiometer that was used on the late RTP tokamak [4], and has been described in detail in [5]. However, there were some minor design changes, compared to the description given in [5]. The scheme of the new 16-channel frequency-tuneable heterodyne system is given in Fig. 4.4. The system is installed at the same toroidal position as two of the high-resolution six-channel spectrometers.
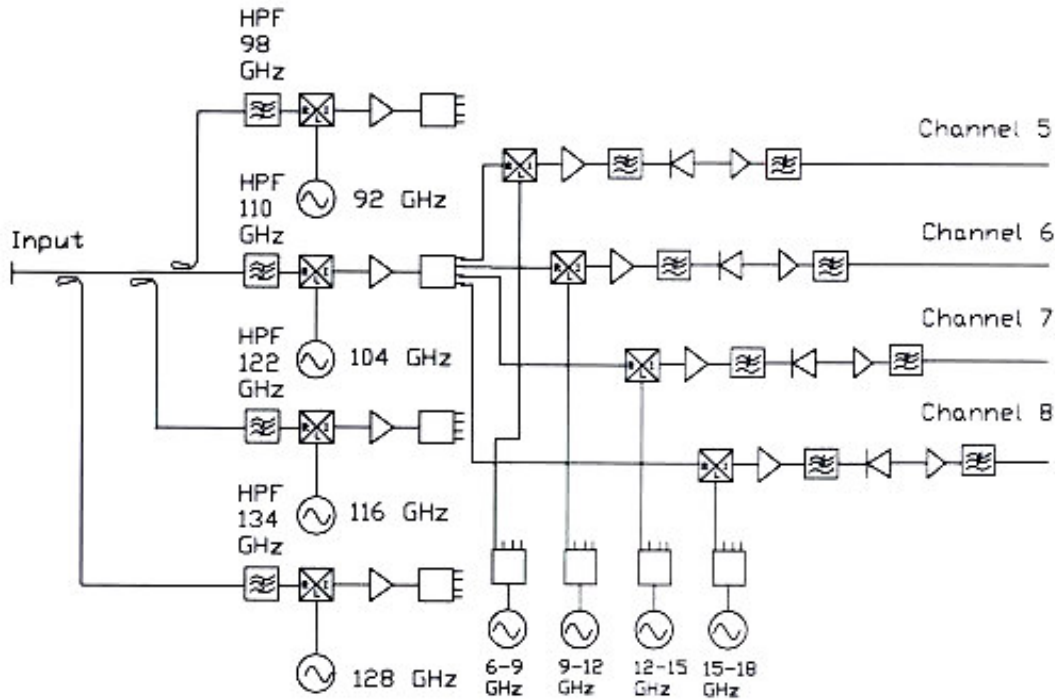
FIG. 4.4. Schematic view of the 16-channel tuneable heterodyne radiometer. The second down-conversion stage is only shown for channel 5 – 8 for reasons of clarity.

The overall spectral range of the radiometer is 48 GHz, from 98 to 146 GHz, divided over 16 channels with a bandwidth of 3 GHz each. The RF signal from the antenna is split into four branches by directional couplers. Each branch transmits the signal to a front end for down-conversion of the RF signal to an IF range of 6-18 GHz. By using different local oscillators (LO) with frequencies of 92, 104, 116 and 128 GHz the IF ranges for each branch correspond to different parts of the input radiation spectrum. High pass filters are used at the input of the mixers to suppress the lower side-band (similar as in the combined second-third harmonic four-channel system). In the IF-stage, after the first down-conversion, the signals are amplified and split into four branches by coaxial power dividers, followed by a second down-conversion step to shift the frequency further down to a frequency band of 0 to 1.6 GHz for each channel by double side-band mixing. To do this, four LOs are required with different frequencies, to cover the input frequency band of 6 to 18 GHz. The result is a total amount of four times four is 16 signals. The YIG-tuned oscillators make it possible to tune the central frequency over 3 GHz. The tuning bandwidth enables for neighbouring channels to overlap each other, to aid the measurement of electron temperature fluctuations and their correlation lengths. The signals are amplified, low-pass filtered and detected by zero-bias Schottky detectors after the second down-conversion stage. The cut-off frequency of 200 or 450 MHz of the low-pass filters (LPF) can be chosen. In the future, it will be possible to change it from 1.5 GHz down to 200 MHz in five steps. The output voltage of the detector is amplified with a programmable video amplifier (0-36 dB). Then, the signals are filtered with a 100 kHz, 300 kHz, 500 kHz or 1 MHz LPF and sampled with a maximum sampling rate of 2 Msa/sec.

The total gain of the radiometer, from waveguide input to detector input is about 45 dB. The sensitivity of the radiometer is approximately 2.2×10^7 V/W, with a detector

sensitivity of 700 V/W. The noise equivalent temperature T_{noise}, referred to the input of the receiver is about 2 eV. However, since the 16-channel radiometer is using the same antenna as the two six-channel spectrometers, additional losses of about 10 dB have to be taken into account, due to waveguide losses and the directional couplers to redirect part of the RF signal to the spectrometers. The receiver noise temperature, referred to the antenna input, is 20 eV. The error ΔT on the temperature measurement, due to receiver noise, can be estimated using the following formula [3]:

$$\Delta T = T_{noise} \sqrt{\frac{2B_v}{B_{IF}}} \quad , \qquad\qquad (4.2)$$

where B_v is the video bandwidth, and B_{IF} the IF bandwidth. For B_v = 1 MHz, B_{IF} = 200 MHz and T_{noise} = 20 eV, one finds an error in the temperature measurement of ΔT = 2 eV. The possibility to tune the central frequency of the channels makes it possible to study the level of electron temperature fluctuations in TEXTOR plasmas. Correlation lengths can be deduced by varying the different frequencies, and thus the distance between two neighbouring channels. It is also possible to determine cross-correlation between the 12 fixed channels of the two spectrometers and the 16 tuneable channels of the new system. However, at the time of writing this thesis, it was not yet possible to tune the frequencies of the channels and, thus, no cross-correlation measurements were done with the 16-channel heterodyne radiometer.

4.1.4 ECE-Imaging diagnostic on TEXTOR

The ECE-Imaging system that has been installed at TEXTOR, in collaboration with UC Davis (USA), features 16 channels [6]. It is measuring along a vertical chord at 114 GHz with a sampling rate up to 2 MHz, ranging from –0.1 to 0.13 m with respect to the equatorial plane. The measured beam waist (Full Width at Half Maximum – FWHM) in the focal plane of the system is about 1.3 cm in the Z-direction (i.e. the E-plane) for the central channels. It increases to 2 cm for the edge channels due to spherical aberrations and edge diffraction due to the limited port size. The scheme of the system is shown in Fig. 4.5.

The default vertical viewing chord position of the ECE-Imaging system is designed to lie on top of the Thomson scattering viewing chord. This is used for the calibration of the ECE-Imaging system.

Together with the 16-channel tuneable frequency heterodyne ECE radiometer, ECE-Imaging is a key diagnostic to measure electron temperature fluctuations and correlation lengths in different heating regimes. Some theoretical aspects of the temperature fluctuation measurements will be given in Section 4.2 of this Chapter, and experimental results will be presented in Chapter 6.

After the DED shutdown, the ECE-Imaging system will be combined with a new Microwave Imaging Reflectometer (MIR) to allow for simultaneous temperature and density fluctuation measurements at the same location in the plasma [7]. A new antenna array with a wide bandwidth will enable broad frequency operation from 125 to 135 GHz, so that simultaneous measurements of temperature profiles and fluctuations in 8 horizontal × 16 vertical sample volumes of about 1 cm × 1 cm × 5 cm (toroidally) will become possible.
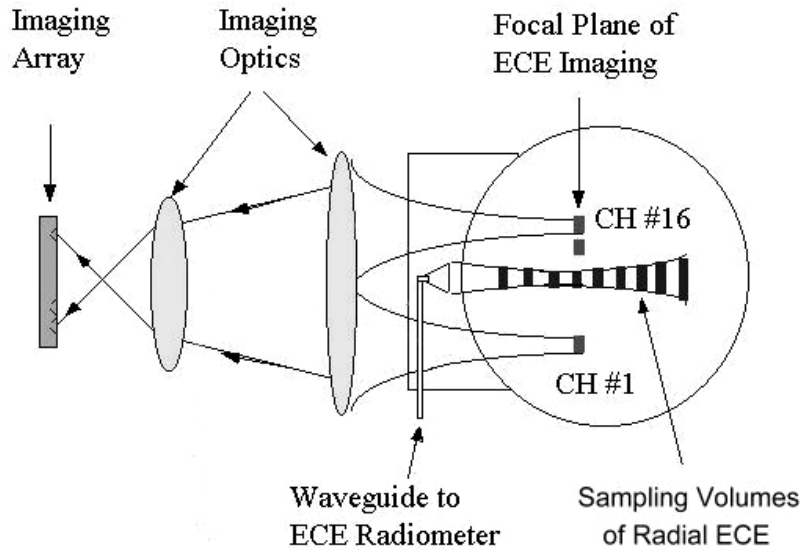
FIG. 4.5. A schematic view of the ECE-Imaging system. Sampling volumes of the radial
ECE diagnostic are given for comparison.

4.1.5 Other diagnostics at TEXTOR

Reflectometers

To study the electron density profile evolution as well as coherent and broadband
density fluctuations, a 10-channel pulsed radar reflectometer is being used [8]. It is based
on the measurement of the time-of-flight of short (~ 1 ns) microwave pulses, which are
reflected in the plasma at density layers where the microwave frequency equals the local
plasma frequency (for the O-mode polarization). Because of the very short time (less than
10 ns) the pulse travels through the plasma, density fluctuations can be regarded as frozen.

The accuracy of 74 ps in time-of-flight corresponds to 11 mm radial accuracy
when reflecting in vacuum. In plasmas, due to the lower group velocity of the pulse, the
accuracy will typically be higher. It can be further improved by averaging subsequent
pulses: the average over 4 pulses yields an accuracy of 5 mm in vacuum.

The pulse radar diagnostic is very well suited for studies of local macroscopic
density perturbations of the density profile, in particular, in presence of large MHD
islands.

Recently, an amplitude modulated O-mode reflectometry system for the
measurement of plasma turbulence properties has been installed [9]. The frequency is
tuneable in the range of $26 - 37$ GHz, which corresponds to the electron density range of
$0.8 - 1.6 \times 10^{19}$ m^{-3}. The system measures simultaneously the *sin* and *cos* component of the
reflected wave for two channels allowing determination of the amplitude and the phase of
the reflected wave. The sampling rate of the reflectometer is 500 kHz.

Thomson scattering

A double-pulse multi-point Thomson scattering system has been installed to
measure the electron temperature and density profile along a full vertical chord through
the plasma [10]. A 25 J ruby laser is used as source. The time separation between the two

$10 - 12$ J laser pulses can be varied from 50 to 500 μs. The laser chord is located 90 mm toward the LFS with respect to the machine axis. The full vertical chord of 900-mm length is resolved into 120 spatial positions of 7.5 mm each. The spectrum at each position is resolved into 80 wavelength channels.

To make a proper estimate for the accuracy of the system, one should pay attention to the statistical properties of the data due to the low signal intensities. This means that the small-scale structures seen on the raw temperature profile do not appear to be generally significant, except for the large MHD effects [11]. The raw electron temperature profiles obtained by the Thomson scattering diagnostic need to be corrected because of the topology of the system. The smoothed Thomson scattering profiles are generally in good agreement with those obtained by ECE.

Spectroscopy

Other diagnostics that have been used to obtain results presented in this thesis are the Charge Exchange Recombination Spectroscopy system (CXRS) and the VUV/XUV Survey Poor Resolution Extended Domain (SPRED) overview spectrometer [12]. CXRS allows to measure ion temperature and toroidal rotation velocity profiles. The system monitors the carbon line C^{IV} at 529.0 nm and utilizes the neutral heating beam.

A VUV/XUV spectrometer is used to study the relative concentrations and the transport behaviour of low- and medium-Z plasma impurities from helium to copper.

In Fig. 4.6, a schematic overview of the diagnostics essential for this thesis is given.
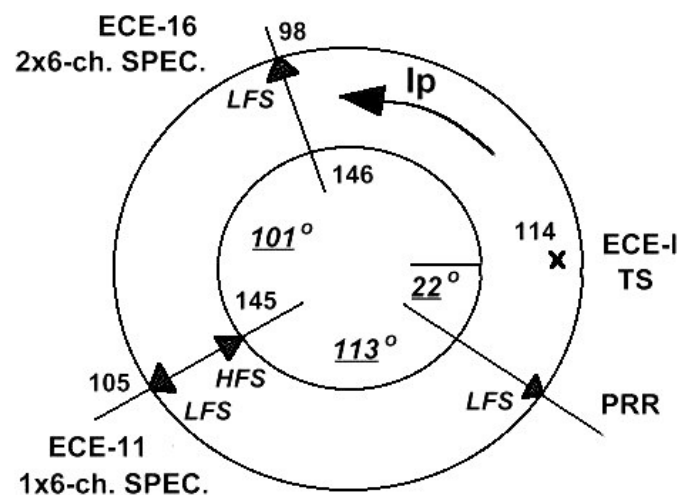

FIG. 4.6. A schematic (top) view of the TEXTOR ECE diagnostics: the 11-channel radiometer (ECE-11) and 16-channel system (ECE-16) are located at approximately 135° and 236°, with respect to the location of the ECE-Imaging (ECE-I). Also the locations of the pulsed radar reflectometer (PRR) and the Thomson Scattering (TS) system are indicated. The toroidal separation in degrees between different diagnostic ports is shown, as are the frequencies of the various ECE systems and the locations of their antennas (dark triangles).

4.1.6 Some aspects of cross-calibration of ECE diagnostics

Since information about the absolute electron temperature in plasma is essential, the proper calibration of the ECE diagnostics is very important. However, this is not a trivial procedure. One should take various effects into account when one performs cross-calibration of the diagnostics. Some ECE systems on TEXTOR (16-channel radiometer and 4+4-channel radiometer) are absolutely calibrated by means of a hot-cold source. Nevertheless, due to the LO's non-stable behaviour and/or non-linearity of the video amplifiers at different input power levels, the obtained calibration factors for ECE channels may vary even from shot to shot. To avoid this, cross-calibration versus another diagnostic with known stable calibration function is required. At TEXTOR, the 11-channel ECE radiometer and the Thomson scattering system are being used for cross-calibration of other ECE diagnostics. Some important aspects of cross-calibration will be discussed below.

Electron temperature as measured by 11-channel ECE radiometer and Thomson scattering

To see if the electron temperature measured by these diagnostics is in agreement, one should take the following aspects into consideration:

1. *Thomson scattering measures along a vertical chord of 90 cm length, at a radial position of 9 cm towards LFS. The 11-channel ECE radiometer is a radial system located 135° away from Thomson scattering in the toroidal direction. A coordinate transformation is needed for proper comparison. The radial plasma displacement and Shafranov shift should be included into the transformation, as has been discussed in Chapter 2 (see Eqs. 2.11 – 2.12).*
2. *To ensure that the temperature profile is smooth, it should not be perturbed by large MHD mode activity in the plasma.*
3. *For temperatures measured by ECE, corrections for optical depth (at low densities), cut-offs (at higher densities) and for magnetic field are needed.*
4. *The Thomson scattering temperature profile should be smoothed and corrected for the magnetic topology.*
5. *It is necessary to realise that the sample volume (spot size) of the ECE channels is much larger than the one of Thomson scattering. Moreover, it is generally different for E (horizontal) and H (vertical) planes and depends strongly on antenna pattern and the local magnetic field value.*

For the 16-channel heterodyne radiometer, the beam is focussed at $R = 2$ m, and the spot size at this location equals to 0.8 cm in the H-plane. At the HFS, the spot size increases up to 5 cm. For the 11-channel radiometer, the vertical spot size approximately equals to 4 cm at all radial positions.

From Fig. 4.7, one can conclude that the electron temperature profile as measured by the 11-channel ECE radiometer is in agreement with the smoothed and corrected one obtained by Thomson scattering. A certain discrepancy between the HFS ECE channels and the Thomson scattering profile can be explained by too simplified a model used for the coordinate transformation.

Cross-calibration of the ECE-Imaging system and 16-channel heterodyne radiometer

The ECE-Imaging system is cross-calibrated versus the smoothed and corrected Thomson scattering profile. For this purpose, a magnetic field of 2.14 T is chosen, so that the lines of sight of both diagnostics coincide. The calibration is usually performed at a line-averaged electron density of $3 - 3.5 \times 10^{19}$ m^{-3}, in the Ohmic phase of the discharge [7].
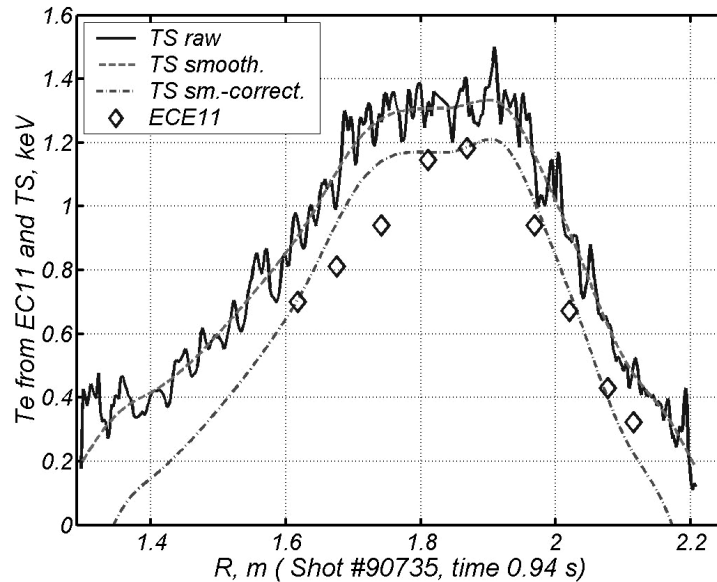

FIG. 4.7. Comparison of the electron temperature as measured by ECE (diamonds) and Thomson scattering (solid line for the raw, dotted line for the smoothed, and dash-dotted for the corrected data). The magnetic field B ~ 2.23 T, line averaged density $n_e = 3 \cdot 10^{19}$ m^{-3}, and the Shafranov shift is about 8 cm.

In Table 4.2, an example of calibration factors for the 16-channel radiometer, obtained from the cross-calibration versus Thomson scattering and the 11-channel ECE radiometer are given for different magnetic field values. Only fully operational channels are listed. Note how calibration factors for different channels are sensitive to the change in magnetic field and averaged electron density, so calibration shots are needed for each experimental session.

Calibration of the 3rd harmonic ECE channels

As has been described in Section 4.1.2, the second harmonic ECE channels of the 4+4-combined 2nd − 3rd harmonic radiometer are absolutely calibrated by means of a hot-cold source. However, calibration of the 3rd harmonic channels is not straightforward. For most of TEXTOR scenarios, the plasma is optically thin for the 3rd harmonic ECE (see Chapter 3). Thus, the measured temperature is the radiation temperature. The only possibility for cross-calibration is in high-density discharges with $n_e = 5\text{-}8 \times 10^{19}$ m^{-3}, for example, during the so-called Radiative Improved Mode (RI-mode). Then, the 2nd harmonic ECE emission is not in cut-off yet, and at the same time, the plasma is optically thick enough for the 3rd harmonic ECE to derive a real temperature from it. Some aspects of proper evaluation of the electron temperature from measurements in optically thin plasmas will be given in Chapter 7.

Table 4.2. Calibration factors for some channels of the 16-channel ECE radiometer obtained by cross-calibration versus Thomson scattering and 11-channel ECE radiometer.

ECE Channel	B_t = 2.14 T, n_e=3·10^{19} m^{-3}		B_t = 2.4 T, n_e=2.2·10^{19} m^{-3}	
	vs. Thomson Sc.	vs. 11-ch. ECE	vs. Thomson Sc.	vs. 11-ch. ECE
98 GHz	50.5	No corresponding channel	Out of plasma	Out of plasma
101 GHz	38	No corresponding channel	Out of plasma	Out of plasma
104 GHz	56	No corresponding channel	Out of plasma	Out of plasma
107 GHz	56	58	No data	No data
113 GHz	77	69	80	74
116 GHz	126	105	105	105
119 GHz	173	175	180	190

4.2 Principles of electron temperature fluctuation measurements

Studies of broadband temperature fluctuations played an important role in the TEXT, RTP, and W7-AS fusion devices, since they are thought to be related to turbulent transport in magnetically confined plasmas [13, 14, 15, 16]. In [13], the possibility that high-frequency electrostatic turbulence can account for the measured electron heat transport in the plasma core has been investigated. It has been found that short wavelength electrostatic turbulence (with poloidal wave number > 1 cm^{-1}) can be responsible for the transport. Studies of plasma edge fluctuations in different devices (tokamaks and stellarators), using various diagnostics suggest a close connection between core/edge plasma turbulence and the associated turbulent transport [17].

In TEXTOR, plasma transport properties can be strongly influenced by the presence of MHD modes, transport barriers and other phenomena. Moreover, one would expect that transport properties would also depend whether or not additional heating is applied. To study the role of electron temperature fluctuations in turbulent transport throughout the plasma, various ECE correlation diagnostics are being used. A short description of these diagnostics, as well as of different analysis methods that have been used to evaluate fluctuation spectra, will be given in this Chapter.

4.2.1 Theoretical principles of correlation measurements

The optically thick ECE signal *S(t)*, as measured by each radiometer channel, consists of an average $\bar{S}$ and a fluctuation $\tilde{S}$ part that are proportional to the average plasma temperature $\bar{T}_e$, and to its fluctuating component $\tilde{T}_e$ plus the statistical radiation noise (also referred to as: intensity fluctuations, thermal noise, wave noise, or photon noise) $\tilde{N}$. The radiation noise has nothing to do with the electron temperature and "real" temperature fluctuations:

$$S(t)=\bar{S}+\tilde{S}\sim\bar{T}_e+\tilde{T}_e+\tilde{N} \ . \tag{4.3}$$

As has been described in Section 4.1.3 of this Chapter, Eq. (4.2) limits the relative fluctuation level in measurements with a single detector. In terms of the output signal, it can be written as follows:

$$\frac{\widetilde{S}_{RMS}}{\overline{S}} = \sqrt{\left(\frac{2B_v}{B_{IF}}\right)} \quad , \tag{4.4}$$

where $\widetilde{S}_{RMS}$ is the root mean square* amplitude of the signal fluctuation. For some TEXTOR ECE diagnostics, relative fluctuation levels are given in Table 4.3.

It can be seen that by increasing B_{IF} or reducing B_v one can reduce the relative fluctuation level that can be measured. It is important to mention that the increase of B_{IF} deteriorates the spatial resolution, whereas a reduction of B_v causes a decrease in the time resolution. For this reason, the 4-channel 2nd-3rd harmonic radiometer is not capable to measure fluctuations with frequencies above 5 kHz (the so-called Nyquist frequency [3,18]), despite it has the best relative fluctuation level of about 1%.

Table 4.3. An example of some relative fluctuation levels for different ECE diagnostics at TEXTOR. Diagnostic parameters are taken from Table 4.1 (see Section 4.1).

ECE diagnostic	B_v	B_{IF}	$\dfrac{\Delta\widetilde{S}_{e,RMS}}{\overline{S}_e}$, %
16-channel heterodyne radiometer	*300 kHz (1 MHz)*	*200 MHz*	*5.4 (10)*
ECE-Imaging	*200 kHz*	*200 MHz*	*4.4*
6-channel spectrometers	*100 kHz (1 MHz)*	*400 MHz*	*2.2 (7)*
4-channel combined 2nd-3rd harmonic radiometer	*10 kHz*	*200 MHz*	*1*

To measure the average amplitude of temperature fluctuations in tokamak plasmas of smaller than 1 - 2%, one needs to get rid of the thermal noise $\widetilde{N}$ [13]. This can be achieved by cross-correlation of two ECE signals whose temperature fluctuations are correlated while the noise fluctuations are uncorrelated. One possibility is to observe the same plasma volume from two different directions, another by using two sample volumes that only partly overlap. Mathematically, the correlation between two signals is the measure of the degree to which the two signals are similar [3]. For two real signal sequences $x(n)$ and $y(n)$ with finite length, the cross-correlation sequence $r_{xy}(l)$ can be defined as:

---

* The root mean square of a discrete signal $X(1:N)$ can be approximated as: $X_{RMS} = \sqrt{\dfrac{1}{N}\sum_{i=1}^{N} X_i^2}$.

$$r_{xy}(l) = \sum_{n=i}^{N-|k|-1} x(n)y(n-l) \ , \tag{4.5}$$

where l is the time shift (or *lag*) parameter, $i = 1$, $k = 0$ for $l \geq 0$, and $i = 0$, $k = l$ for $l < 0$. To identify the common normalized temperature fluctuation for two ECE signals $S_1(t)$ and $S_2(t)$, as described by Eq. (4.3), the cross-correlation sequence at zero time lag can be written as:

$$r_{12} \propto \overline{(S_1 - \overline{S}_1)(S_2 - \overline{S}_2)} = \overline{\widetilde{T}_{e1}\widetilde{T}_{e2}} + \overline{O}(\widetilde{N}_1, \widetilde{N}_2) \ , \tag{4.6}$$

where the second term is small, compared to the first one, if care is taken that S_1 and S_2 are not exactly the same signals. If $T_{e1} = T_{e2} = T_e$, it is possible to get the normalized temperature fluctuation amplitude, after normalizing Eq. (4.6) to the mean signal level [13]:

$$\frac{\widetilde{T}_{e,RMS}}{\overline{T}_e} = \sqrt{\frac{r_{12}}{\overline{S}_1 \overline{S}_2}} \ . \tag{4.7}$$

The statistical noise level can be defined as follows [13, 19, 20]:

$$\Delta\left(\frac{\widetilde{T}_{e,RMS}}{\overline{T}_e}\right) = \sqrt{\frac{\Delta r_{12}}{\overline{S}_1 \overline{S}_2}} = \frac{1}{\sqrt[4]{M}} \sqrt{\frac{\sigma_1}{\overline{S}_1} \frac{\sigma_2}{\overline{S}_2}} \ , \tag{4.8}$$

where σ_1 and σ_2 are the standard deviations of $\widetilde{S}_1$ and $\widetilde{S}_2$, and M is the total number of samples. It is clear that a long sampling time is required to reduce the statistical error below the coherent temperature fluctuation amplitude. For example, to resolve fluctuations with an amplitude of 2% with a resolution of 0.3%, and taking ratio $\sigma_i/\overline{S}_i \sim 5\%$ (as it is, for example, for the 16-channel frequency tuneable radiometer), one gets $M \sim 8\times10^5$ samples. At a sampling rate of 400 kHz (for fluctuations with typical frequencies below 200 kHz), the sampling needed is about 0.2 s.

It is necessary to remark that the cross-correlation method does not require ECE signals to be absolutely calibrated. Besides the *rms* estimation of the fluctuations given by Eq. (4.7), it is useful to calculate the *cross-spectral density* for two discrete signals, x and y [23, 24, 25]:

$$S_{xy}(\omega) = \sum_{m=-\infty}^{m=+\infty} r_{xy}(m)e^{-j\omega m} \ , \tag{4.9}$$

where $\omega = 2\pi f$. This is the inverse Fourier transform of the cross-correlation function. Since real signals have finite length, only an *estimation* of the cross-spectral density is possible: the more samples a signal consists of, the more accurate the estimation is. The one-sided cross-spectral density can be written as:

$$S_{xy}(\omega) = |S_{xy}(\omega)| e^{-j\varphi(\omega)} \ , \tag{4.10}$$

where $\varphi(\omega)$ is the cross-phase between signals x and y, and $|S_{xy}(\omega)|$ is the amplitude of the cross-spectral density.

In practice, it is useful to normalize the correlated power by the total power. This is the so-called coherence between signals x and y [23, 24, 25, 26]:

$$C_{xy}(\omega) = \frac{|S_{xy}(\omega)|^2}{S_{xx}(\omega)S_{yy}(\omega)} \ . \tag{4.11}$$

Here, S_{xx} and S_{yy} are power spectra of signals x and y, respectively. The coherence is constrained between 0 and 1.

4.2.2 Experimental schemes for temperature fluctuation measurements

As has been shown earlier, it is not possible to get rid of the thermal noise completely, but a relatively long sampling time can reduce the statistical error by a factor of $\sim 1/M^{1/4}$. There are several schemes that allow the decorrelation of thermal noise with sufficiently low statistical error. In this Section, only methods that are relevant for TEXTOR diagnostics will be described. A complete overview of different methods for the thermal noise decorrelation is given elsewhere in the literature [13, 15, 16, 20, 21].

Correlation technique with a single line of sight

For two neighbouring channels (radial position $r_1 \neq r_2$) of a radiometer with a single line of sight, temperature fluctuations are partly correlated if the correlation length of these "true" fluctuations is sufficiently large. The thermal noise is uncorrelated and will not contribute to the fluctuation spectrum. It is possible to choose two separated ECE frequency bands such that the two corresponding radial positions r_1 and r_2 are still coincident within the natural line width of ECE [13,15]. In other words, disjoint frequencies are coming from the same sample volume to observe coherent temperature fluctuations (see Fig. 4.8). This scheme has been firstly developed and realized at TEXT-U tokamak [22]. The 16-channel frequency tuneable heterodyne radiometer at TEXTOR will utilize the same method. However, on the moment of writing this thesis, no results were yet available with this diagnostic due to the absence of YIG-tuned oscillators.

As has been discussed already in Section 4.1 of this Chapter, the poloidal separation between ECE-Imaging channels is about 1 - 1.5 cm, and the observation spot is for each channel is in order of 1.3 – 2 cm. This makes the system a powerful tool for the study of sufficiently large temperature fluctuations and enables to measure correlation lengths in the poloidal direction. However, for the work presented in this thesis, the ECE-Imaging system was equipped with a single Backward Wave Oscillator (BWO). The noise generated by this BWO will be correlated for any combination of channels. Nevertheless, it will be shown in Chapter 6 that "true" temperature fluctuations with a relatively large correlation length are still detectable by cross-correlation between adjacent channels of the ECE-Imaging system.
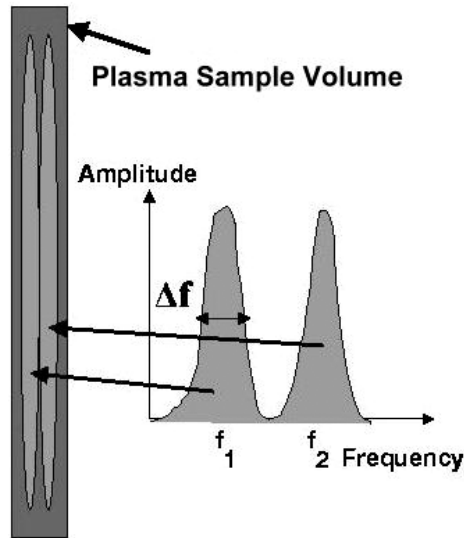
FIG. 4.8. Graphical interpretation of the thermal noise decorrelation method with a single line of sight technique.

Autocorrelation function of a single channel

As has been shown in [13], even with a single line of sight and a single channel the spectrum can be evaluated from the autocorrelation function $r_{11}(S_1(t), S_1(t + \tau))$ under certain assumptions. If the spectrum of the "true" temperature fluctuations is limited and differs in shape from the thermal noise, they can be separated in the autocorrelation function. The thermal noise generates a peaked autocorrelation function around time lag $\tau = 0$. It has a half width of $\sqrt{\ln 2 / \pi}/B_\nu$. This peak should be subtracted from the autocorrelation function, and a Fourier transform should be applied to the remainder. The resulting spectrum can be used for temperature fluctuation studies. This scheme can be used by any of the ECE systems at TEXTOR with a post-detection bandwidth much larger than the width of the temperature fluctuation spectrum.

Examples of autocorrelation power spectra of the TEXTOR ECE signals with and without ECRH are shown in Fig. 4.9. During ECRH, the spectrum shows a slope ($S^2(f) \sim f^{-a}$) of the kind seen at the TJ-II stellarator [27], although the exponent seems to be somewhat smaller. The difference between Ohmic and ECRH phases might be attributed to a difference in the Doppler shift. However, no measurement of the plasma rotation has been made for this shot. Note: the power absorption of all heating methods (Ohmic, ECRH, NBI, ICRH, etc.) increases with higher temperatures. Therefore, a small fluctuation in temperature can be non-linearly amplified by the heating, leading to modification of the temperature profiles and a change in the local turbulence characteristics like power spectra.
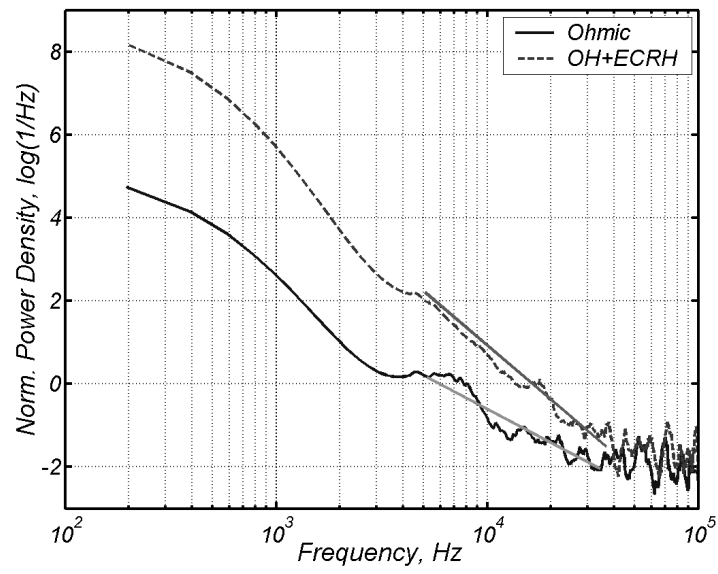
FIG. 4.9. Difference in normalised power spectra for Ohmic and ECRH regimes. Straight lines give a difference in a slope between two heating regimes.

References

[1]   G. Waidmann *et al*., Rev. Sci. Instrum. **68**, 492 (1997).

[2]   J.G. Proakis, D.G. Manolakis, *Digital Signal Processing*, Prentice Hall, New Jersey (1996).

[3]   H.J. Hartfuss, T. Geist and M. Hirsch, Plasma Phys. Control. Fusion **39**, 1693 (1997).

[4]   J.F.M. van Gelder *et al*., Rev. Sci. Instrum. **66**, 418 (1995).

[5]   V.S. Udintsev *et al*., Rev. Sci. Instrum. **72**, 359 (2001).

[6]   B.H. Deng *et al*., Rev. Sci. Instrum. **72**, 368 (2001).

[7]   M.J. van de Pol *et al*., in Proc. of the 12th Joint Workshop on ECE and ECRH, p. 203 (Aix-en-Provence, May 13-16, 2002), edited by G. Giruzzi (World Scientific, Singapore, 2002).

[8]   J.C. van Gorkom *et al*., Rev. Sci. Instrum. **72**, 336 (2001).

[9]   A. Krämer-Flecken *et al*., in Proc. of the 28th EPS Conf. on Control. Fusion and Plasma Phys., Madeira, Portugal, Eur. Conf. Abstr. Vol. **25**A, 1393 (2001).

[10]   C.J. Barth *et al*., Rev. Sci. Instrum. **72**, 1138 (2001).

[11]   B.Ph. van Milligen *et al*., Rev. Sci. Instrum. **74**, 3998 (2003).

[12]   A.J.H. Donné *et al*., Rev. Sci. Instrum. **72**, 1046 (2001).

[13]   G. Cima *et al*., Phys. Plasmas **2**, 720 (1995).

[14]   S. Sattler, H.J. Hartfuss, Plasma Phys. Control. Fusion **35**, 1285 (1993).

[15]   H.J. Hartfuss, M. Häse, in Proc. of the 10th Joint Workshop on ECE and ECRH, p. 119 (Ameland, April 6-11, 1997), edited by Tony Donné and Toon Verhoeven (World Scientific, Singapore, 1997).

[16]   B.H. Deng *et al*., Rev. Sci. Instrum. **72**, 301 (2001).

[17]   B.A. Carreras *et al*., Phys. Plasmas **6**, 4615 (1999).

[18]   C. Gasquet, P. Witomski, *Fourier Analysis and Applications: Filtering, Numerical Computation, Wavelets*, Springer-Verlag, New York (1999).

[19]   B.H. Deng, Ph.D. dissertation, UC Davis (1999).

[20]   M. Häse, H.J. Hartfuss, C. Watts, in Proc. of the 10th Joint Workshop on ECE and ECRH, p. 131 (Ameland, April 6-11, 1997), edited by Tony Donné and Toon Verhoeven (World Scientific, Singapore, 1997).

[21]   Y. In *et al*., Presented at the 43rd Annual Meeting of the DPP, Long Beach, CA, USA (2001).

[22]   G. Cima *et al*., Phys. Plasmas **2**, 720 (1985).

[23]   L.R. Rabiner, B. Gold, *Theory and Application of Digital Signal Processing*, Englewood Cliffs, NJ: Prentice-Hall (1975).

[24]   P.D. Welch, *IEEE Trans. Audio Electroacoustics,* Vol. AU-15, p. 70 (June 1967).

[25]   A.V. Oppenheim, R.W. Schafer, *Discrete-Time Signal Processing*, Englewood Cliffs, NJ: Prentice-Hall (1989).

[26]   Ch. P. Ritz *et al*., Rev. Sci. Instrum. **59**, 1739 (1988).

[27]   F. Castejón, B. Ph. van Milligen, E. de la Luna, *Private Communications* (2002).

Chapter 5

MHD modes studied by microwave diagnostics at TEXTOR

Magnetohydrodynamic (MHD) modes and their influence on the transport properties of tokamak plasmas are important research themes at TEXTOR [1, 2]. The evolution of the electron temperature distributions of the islands in relation to that of the background plasma is studied by means of fast Electron Cyclotron Emission (ECE) diagnostics. The ECE diagnostic set-up at the TEXTOR tokamak makes it possible to analyse the temperature gradients inside the island in detail. These observations help to understand the flow of the heat flux from the plasma core around and inside the island. At TEXTOR, the temperature and density profiles are essentially flat inside the island. Moreover, under certain conditions, when radiation losses inside large $m/n = 2/1$ mode are not dominant, a secondary temperature and density peaking are observed inside the island [1]. This is an indication that the confinement inside the island is improved, compared to the background plasma. One should note, however, that the secondary density peaking is much more pronounced than the secondary temperature peaking. In this paper, the heat diffusivities along and across the field lines inside large $m/n = 2/1$ islands in TEXTOR are analysed using the extended Rutherford model [3] and the resistance network model [4].

Another striking result is an observation by ECE of the existence of a small mode with higher m number in the $q = 1$ and $q = 2$ vicinities, that has been earlier observed on the density evolution by the pulsed radar reflectometer [5, 6]. Interestingly, this mode suddenly uncouples from the strongly coupled $m/n = 1/1$ and $2/1$ modes, and its frequency increases significantly in a very short time interval.

At TEXTOR, a disruption prevention method has been developed [2]. Disruptions can deposit an enormous amount of power to the tokamak wall and, therefore, cause damage. That is why disruptions should be avoided, or, if they still occur, their effect should be minimized. In the prevention scheme, two ECE channels from the 11-channel radiometer (see Section 4.1.1), one on the Low Field Side (LFS) and one on the High Field Side (HFS), measure MHD mode oscillations. From the cross-correlation of these channels, a trigger is generated to start the Neutral Beam Injection (NBI) to prevent the disruption, or alternatively a strong injection of Helium is triggered to mitigate the effects of disruption.

This Chapter is organized as follows. Transport properties of plasma in presence of large MHD modes, as well as some aspects of the island rotation are discussed in Section 5.1. The disruption prevention scheme is described briefly in Section 5.2.

5.1 Transport properties of plasma in presence of large MHD modes[1]

Large MHD modes at TEXTOR are usually created by a fast density ramp up with a slower current ramp up in the early phase of the discharge [2]. To increase the mode

---

[1] This section is very similar to an article with the title "*Plasma properties in presence of MHD modes studied by ECE at TEXTOR*" of V.S. Udintsev *et al.*, accepted for publication by Nuclear Fusion (2003).

width and to reduce and flatten the toroidal plasma (counter-) rotation profile, co-neutral beam injection (co-NBI) of a few hundreds of kW is being applied. With reduced rotation, wall stabilization is also reduced, which results generally in larger island widths. Counter neutral beam injection (counter-NBI) (at lower than co-NBI power) is being used to prevent the mode from wall locking and, thus, from a disruption. In Fig. 5.1, a typical example of a discharge with a large $m = 2$ mode is shown. The current ramp up is continued up to 1 s, and the line-averaged electron density has reached its maximum of 2.2×10^{19} m^{-3} at ~ 0.9 s. The toroidal magnetic field B_φ was 2.4 T at the geometric radius of the vessel $R_0 = 1.75$ m. No additional gas puff has been performed in this shot.

5.1.1 The $q = 2$ radial position and $m/n = 2/1$ island width calculations

Using the different ECE diagnostics, the evolution of the electron temperature profiles has been studied for the rotating $m/n = 2/1$ island. In order to estimate the island width properly, the $q = 2$ surface position should be determined correctly. Since most of the magnetic diagnostics were not available for this series of shots, the $q = 2$ position can be either determined from the inversion of the ECE oscillations between different channels, or calculated from the current density profile, that is derived from the temperature profile assuming Spitzer resistivity. The role of neoclassical effects on the current density profile calculation will be discussed later.

For the same shot as in Fig. 5.1, the temporal evolution of the temperature profiles through the O- and the X-points of the island has been studied. Using a coordinate transformation and taking the total plasma displacement of ~ 9 cm into account (which is a combination of a programmed radial plasma displacement and the Shafranov shift), it is possible to have the full temperature profiles using the data from all ECE diagnostics, even though they measure at different toroidal and poloidal positions. Figure 5.2 shows the evolution of the temperature profiles inside/outside the $m/n = 2/1$ island at the LFS at six points in time. A temperature flattening inside the island can be clearly seen. The $q = 2$ position is determined to be at the crossing of the profiles through the O- and the X-points of the island. One should note that the plasma current is still in the ramp up phase until ~ 1 s, so the $q = 2$ surface is shifting outwards. It can also be seen that the asymmetry of the island between inside/outside of the $q = 2$ surface increases, as the island grows. Around $t \sim 1$ s, the $q = 2$ surface moves out of sight of the 112 GHz ECE channel at $R = 2.11$ m, and there are only two ECE channels located outside $q = 2$ at $R = 2.17$ m (109 GHz) and $R = 2.205$ m (107 GHz). Under the assumption that outside and close to the island separatrix the electron temperature is a flux function [7], the $q = 2$ position has been calculated for this point in time using the following relations [8]:

$$\Delta r = \frac{\Delta T_e}{dT_e/dr} \; , \tag{5.1a}$$

$$R_{q=2} = R_{114} + \Delta r \; , \tag{5.1b}$$

where ΔT_e is the difference between temperatures at the X- and O-points of the island at $R_{114} = 2.07$ m (as measured by the 114 GHz ECE channel), dT_e/dr is the temperature gradient at the X-point calculated for the same R, Δr is a displacement of the flux surfaces in the neighbourhood of the separatrix which is proportional to the change of the island width w, R_{114} is the location of the 114 GHz channel ($R_{114} - R_0 = 0.32$ m). If the island is
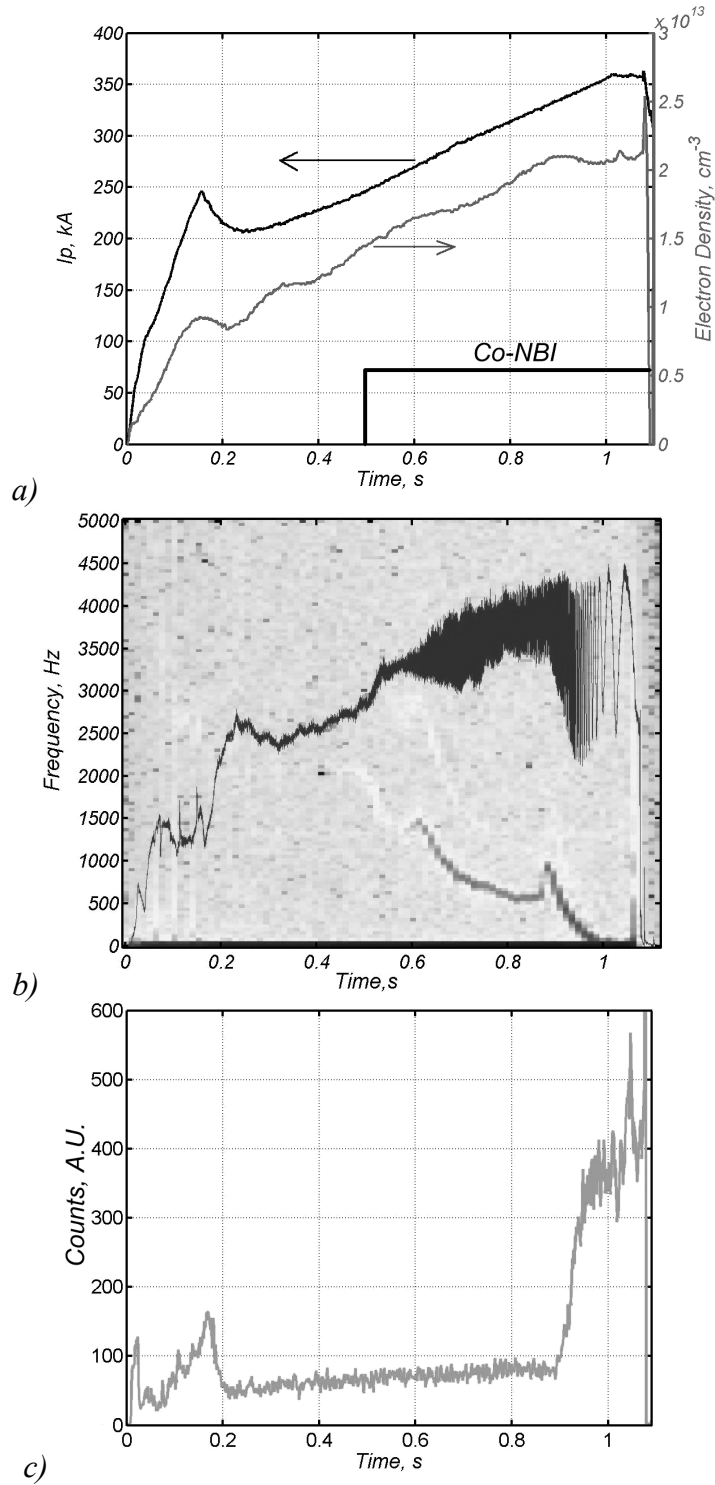
FIG. 5.1. Example of a discharge where a large m = 2 mode has been created. For this shot the magnetic field B_t = 2.4 T. Co-NB (~ 160 kW) injection is applied at 0.5 s. Evolution of the electron density and plasma current is shown in (a). A spectrogram (b) shows that the frequency of the mode is slowing down from 1.5 to 0.5 kHz, then spinning up to 1 kHz at ~ 0.88 s during a very short time interval, and slowing down again finally leading to a disruption. At ~ 0.88 s, an increase of the C-IV intensity (c) is observed by the VUV/XUV spectrometer. The mode activity is clearly seen on the 115 GHz ECE channel at the time between 0.45 – 1.07 s (b).
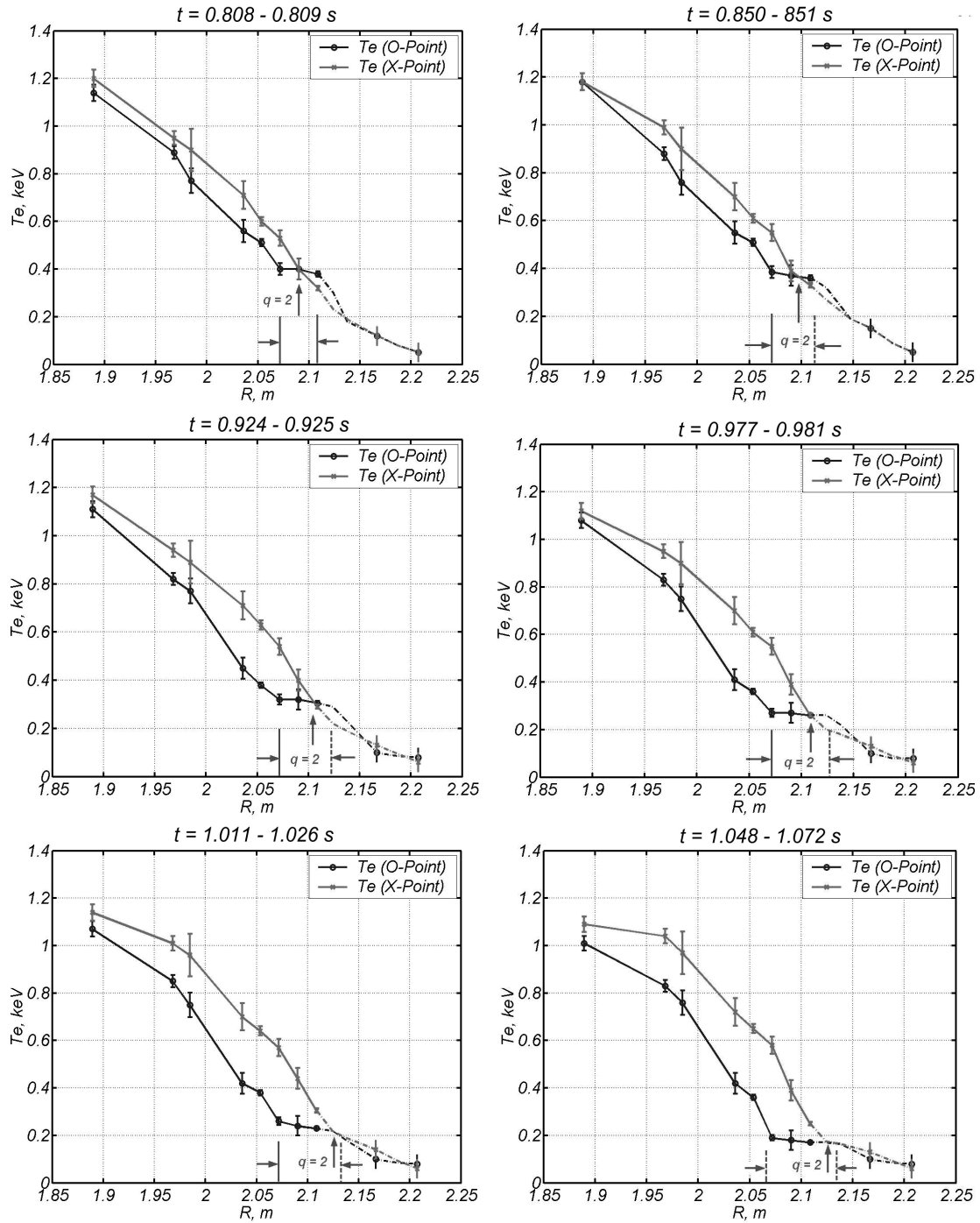
FIG. 5.2. Temporal evolution of temperature profiles through O- (dots, dark line) and X-points (crosses, light line) of a large m/n = 2/1 island at the LFS. As the mode grows, its asymmetry with respect to the q = 2 position becomes more pronounced. At t ~ 1.05 s, the total island width (as shown by arrows) is almost equal to its displacement Δr . Dashed lines are extrapolated temperature profiles, since there are only a very few ECE channels located outside q = 2. Between R = 2.170 – 2.205 m, also a small m/n = 3/1 mode activity has been detected.

radially symmetric with respect to the $q = 2$ location, Δr can be described as the island half-width $w/2$. This can be seen in Fig. 5.2 for the times before 0.85 s. Close to the disruption at 1.07 s, however, the asymmetry between the core-facing and the wall-facing separatrices is very large, and Δr almost equals to the island width w.

Another method to determine the $q = 2$ radial position is to calculate it from the toroidal current density profile evolution. From Ampere's law, the poloidal magnetic field B_θ at the flux surface with a dimensionless minor radius coordinate ρ,

$$\rho = [r - \Delta(\rho)]/a = [(R - R_0) - \Delta(\rho)]/a , \tag{5.2}$$

can be described by Eq. (2.14). In Eq. (5.2), $\Delta(\rho)$ equals to the plasma displacement of each flux surface due to the combination of the Shafranov shift and the programmed radial plasma displacement. The current density profile can be determined according to the theory of Spitzer [9, 10]. For fully ionised plasma, the resistivity along the magnetic field lines as a function of ρ can be written as follows:

$$\eta(\rho)=1.03\times10^{-4} \ln\Lambda \frac{\gamma_z(Z_{eff})}{T_e^{3/2}(\rho)} , \tag{5.3}$$

where Z_{eff} is the effective ion charge, T_e is the electron temperature in eV,

$$\ln\Lambda = \ln\left(1.09\times10^{14}\frac{T_e}{Z_{eff}\cdot n_e}\right) \tag{5.4}$$

is the Coulomb logarithm, and

$$\gamma_z(Z_{eff})=Z_{eff}\left(0.29+\frac{0.457}{1.077+Z_{eff}}\right) \tag{5.5}$$

is a numerical parameter which depends on Z_{eff} [11]. For the NBI-heated discharges at TEXTOR, Z_{eff} typically varies from 2.5 to 3.5 [12]. The parallel electric field across the plasma can be calculated from the measured single turn loop voltage:

$$E=\frac{V_{loop}}{2\pi R_0} . \tag{5.6}$$

Using Ohm's law and assuming that the electric field and Z_{eff} are constant throughout the plasma, the toroidal current density can be written as follows:

$$j(\rho)=\frac{E}{\eta(\rho)}=\frac{V_{loop}}{2\pi R_0\eta(\rho)}=k_s T_e^{3/2}(\rho) . \tag{5.7a}$$

Here, E is the parallel electric field across the plasma, V_{loop} is the loop voltage measured outside the plasma, k_s is a constant that depends on the total plasma current I_{pa} and

electron temperature profile. Using Eqs. (2.13a), (2.14) and (5.7a), one gets the following expression for the *q* profile:

$$q(\rho) = \frac{\rho^2 B_\varphi(R_0)}{\mu_0 R_0 k_s \int\limits_0^\rho \rho' T_e^{3/2}(\rho')d\rho'} \quad . \tag{5.8}$$

However, in toroidal geometry with the magnetic field decreasing towards the larger major radius coordinate, some electrons with a relatively high perpendicular velocity, with respect to the magnetic field direction, are reflected by the increasing magnetic field along the field line. These electrons bounce back and forth between the HFS of that field line and are trapped on so-called banana orbits and, thus, they are excluded from carrying current in the toroidal direction [11]. Due to this so-called *neoclassical* effect, the current density profile shape is modified. The effect can be quite significant, especially for large tokamaks. An example of two current density profiles for the TEXTOR tokamak, with and without neoclassical effect included, is shown in Fig. 5.3 for another shot than the one in Figs 5.1 and 5.2. Trapped particles are responsible for the existence of an additional toroidal current that is independent from the conventional current driven by the applied electric field. In the presence of a density gradient, trapped particles carry a current that is analogous to the diamagnetic current of passing particles but parallel to the magnetic field. Both trapped electrons and ions carry this current, and momentum transfer to the passing particles of both species (friction) that adjust their velocities is taking place. The so-called *bootstrap current* arises then from the difference in velocity between passing ions and electrons. In presence of trapped electrons, the resistivity of plasma will be enhanced, and Eq. (5.7a) can be written as follows:

$$j(\rho) = \frac{E}{\eta(\rho)}(1 - f_{trap}(\rho)) \quad , \tag{5.7b}$$

where f_{trap} is the fraction of the trapped particles which depends on the inverse aspect ratio $\varepsilon = \rho/R_0$ and the dimensionless collisionality v^* [11, 13]:

$$v^* = \frac{R_0 q(\rho)}{\tau_e(\rho) v_{Te}(\rho) \varepsilon^{3/2}} \quad . \tag{5.9}$$

Here, $\tau_e(\rho)$ is the electron collision time, $v_{Te}(\rho)$ is the electron thermal velocity. A boundary condition for the plateau and the banana regimes can be defined as $v^* \sim 1$. For the TEXTOR shots in Figs 5.1 and 5.2, the plasma is mainly in the plateau and Pfirsch-Schlüter regimes, and only in a very short radial range between $\varepsilon = \rho/R_0 \approx 0.48 - 0.55$ the plasma is on the border between plateau and banana regimes. The values of τ_e are changing from ~ 9 μs in the plasma centre down to ~ 5 μs at the edge for the parameters given in Table 5.1. The trapped electron fraction f_{trap} is calculated to be smaller than 12 - 15 % and the neoclassical correction can be neglected in the calculation of the $q = 2$ radial position. It is important to mention that Eq. (5.7b) does not take into account the bootstrap current. It has been found from the calculation of the current density profiles with both Spitzer and neoclassical resistivities that less than 5% of the total toroidal plasma current

is flowing outside $q = 2$. Therefore, one can assume that the radial position of the $q = 2$ surface does not depend too strongly on the shape of the current density profile.

In Fig. 5.4(a), the dimensionless island width w/a (upper curve) and displacement $\Delta r/a$ (lower curve) are shown for the same shot as in Figs 5.1 and 5.2. The width of the island is assumed to be equal to the radial size of the flat spot at the O-point (as seen in Fig. 5.2). Using Eqs (5.1a,b), the value of Δr has been calculated. The error bars are calculated from the spatial resolution for each channel and from the radial separation between the channels. Figure 5.4(b) shows the evolution in time of the $q = 2$ position as determined from the profiles in Fig. 5.2 (upper curve) and calculations using Eq. (5.8) (lower curve). In Fig. 5.4(c), the calculated radial q profile is shown for ~ 0.97 s. For this particular shot, no sawtooth activity, as well as no clear $m/n = 1/1$ mode, have been observed, which suggest q_0 to be greater than 1. The value of q_a depends on the total plasma current and changes from 4.6 for $I_{pa} = 315$ kA at 0.8 s to 4.03 for $I_{pa} = 360$ kA at 1 s. Some values calculated for ~ 0.97 s are shown in Table 5.1. It can be seen that the agreement between measured and calculated evolution of the $q = 2$ position is quite good: in the order of the spatial resolution of the ECE diagnostics.
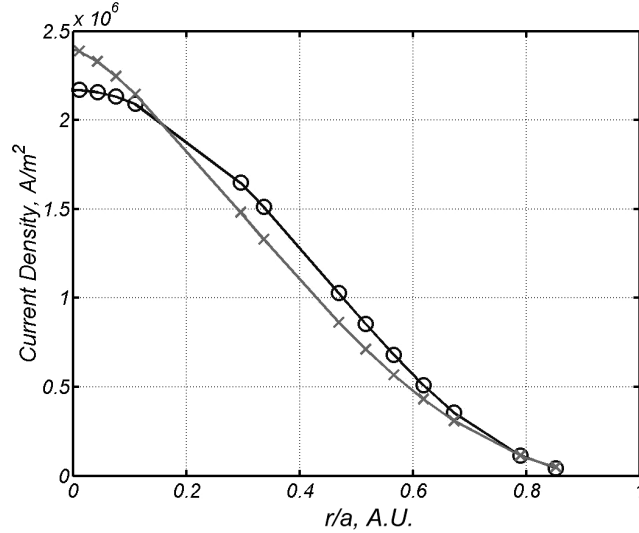
FIG. 5.3. Examples of the current density profile for TEXTOR plasmas calculated using the Spitzer model (circles) and with neoclassical effects taken into account (crosses) for a different shot than shown in Figs. 5.1 and 5.2. The plasma centre is at r/a = 0. In this example, the fraction of trapped electrons f(r/a) is about 20% at r/a = 0.5. For calculations, the total plasma current I_{pa} was taken to be the same for both cases.

TABLE 5.1. Some parameters at the q = 2 position ($R_{q=2} \approx 2.11$ m) for the time of ~ 0.97 s (see Fig. 5.4).

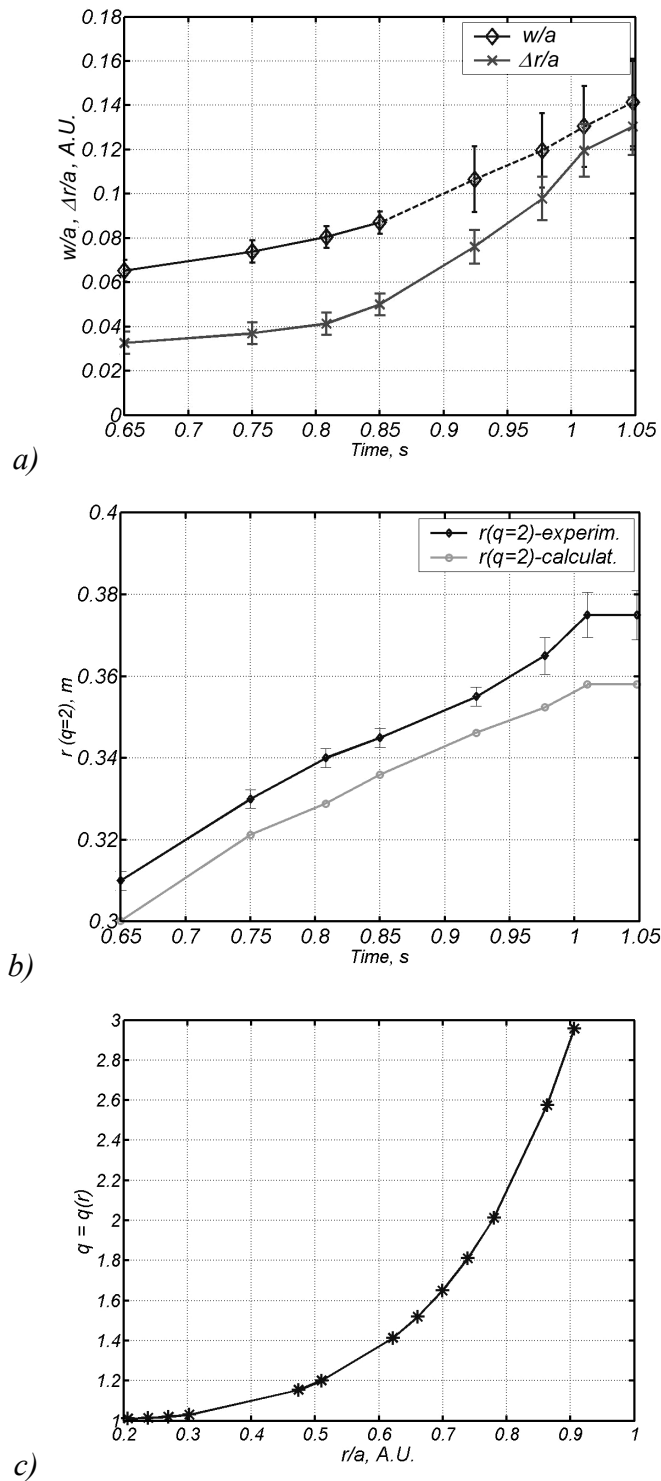| T_e, eV	n_e, m^{-3}	τ_e, s	η_{Sp}, Ohm·m	j, kA/m^2	$v_e^{thermal}$, m/s
260	2×10^{19}	2×10^{-6}	5×10^{-7}	100	2×10^7

a)

b)

c)

FIG. 5.4. The dimensionless width w/a and displacement $\Delta r / a$ with error bars of the large m/n = 2/1 island (a) and the q = 2 position (b) as functions of time. A systematic difference in (b) is coming from the approximation that has been used to calculate q(ρ), neglecting neoclassical corrections to Spitzer's resistivity. As can be seen from plot (a), the island width is growing linearly up to ~ 0.8 s, and then its growth rate increases markedly. The calculated radial q profile at ~ 0.97 s is shown in (c).

5.1.2 Transport properties of plasma in presence of the large *m/n* = 2/1 island

As has been reported earlier in [1], secondary temperature and density peaking inside the *m/n* = 2/1 island has been observed indicating an improved confinement inside the island. Although the secondary density peaking is almost always present, as evidenced by pulsed radar reflectometer measurements, the appearance of the secondary temperature peaking depends strongly on the island width and asymmetry. Figure 5.5(a,b) shows the evolution of the pulsed radar reflectometer signal at 47 GHz and of the HFS ECE channels at 140 and 145 GHz. For this shot, B_φ = 2.25 T at the plasma centre, and n_e = 2.2×10^{19} m^{-3} at the q = 2 radius. A secondary temperature peaking of 30 eV, compared to the temperature at the islands separatrix, is observed by the ECE channel. A secondary density and temperature peaking inside the island have been observed before by the Thomson scattering measurements at RTP [8] and TEXTOR [14, 15]. An example is shown in Fig. 5.5(c).

For the same shot as shown in Fig. 5.1, 5.2 and 5.4 and parameters given in Table 5.1, the transport properties of the TEXTOR plasma in the presence of the large islands have been studied using the extended Rutherford model [3, 8] and the resistance network analogy model described in [4].

In this TEXTOR shot, the total temperature flattening inside the island at the LFS is clearly seen (see Fig. 5.2). The resistance network model has been applied for t = 0.97 s. The ratio between parallel, $\tau_{//} = (m\pi R q^*)^2 / \chi_{//}$, and perpendicular, $\tau_\perp = w^2 / \chi_\perp$, transport times inside the island can be expressed as follows:

$$\frac{\tau_{\parallel}}{\tau_{\perp}} = \left(\frac{m\pi R q^*}{w}\right)^2 \frac{\chi_{\perp}}{\chi_{\parallel}} \; . \tag{5.10}$$

Here, q^* is the safety factor related to the field line helicity around the magnetic axis of the island just inside the separatrix. In general, q^* is a function of the current density profile inside the island:

$$q^* = \frac{8\pi r^2 B_\varphi(R_0)}{\mu_0 m^3 \delta I} \; , \tag{5.11}$$

where δI is an incremental current associated with the O-point of the island. From [16], the island width can be expressed in terms of the radial magnetic field perturbation at the rational surface $\widetilde{B}_r$:

$$w = 4\sqrt{\frac{\rho q}{m B_\theta \, \partial q / \partial \rho}} \sqrt{\widetilde{B}_r} \; , \tag{5.12}$$

with all the quantities taken at the rational surface. From $\widetilde{B}_r$, the amplitude of the perturbed component of the poloidal field can be deduced for the given *m* and *n* mode numbers, and the incremental current δI can be calculated. Unfortunately, no useful magnetic diagnostics were available to measure the perturbed poloidal magnetic field for this shot programme. Nevertheless, a very rough approximation can be made using Eq.

(5.12) and following the method for the δI calculation described in [4]. Then, $\widetilde{B}_r \sim 2 \times 10^{-3}$ T, and δI is estimated to be in the order of a few kA. Equation (5.11) can be written in the following form:

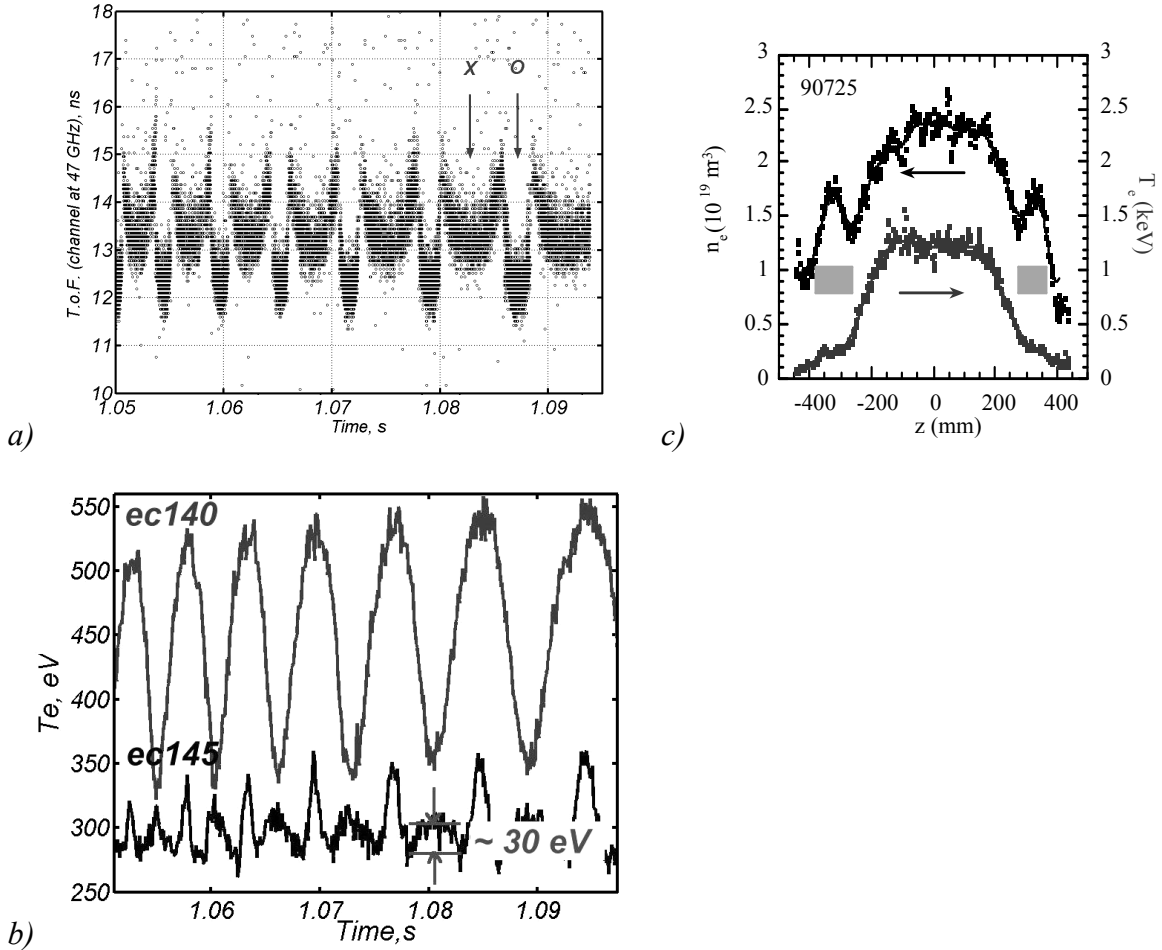$$q^* = 32\pi \frac{\rho q^2}{m^3 w^2 \, \partial q / \partial \rho} \; .$$ (5.11a)

a)

b)

c)

FIG. 5.5. Secondary density and temperature peaking inside a large m/n = 2/1 island as evidenced by the pulsed radar reflectometer at the LFS (a) and ECE at the HFS (b). For this shot, the island width is estimated to be about 4 – 5 cm. The island is symmetrical with respect to the q = 2 position at the HFS. The Thomson scattering profiles (c) confirm the secondary density peaking and temperature flattening inside the island. Fig. 5.5(c) is taken from [15] with kind permission of the authors.

For an island width of 5.5 - 6.0 cm and $\partial q / \partial \rho \approx 12$ m^{-1}, the q^* value calculated by using Eq. (5.11a) is found to be about 350. The calculated q^* value depends strongly on the island width w and radial position ρ, which are determined from the measurements. Therefore, the error bar for q^* can be quite considerable.

For the parameters given in Table 5.1, the parallel heat diffusivity $\chi_\parallel \sim v_e^2 \tau_e$ is calculated to be $\sim 6 \times 10^8$ m^2/s. The temperature flattening inside the island is very pronounced and the difference between temperatures in the O-point and the background

plasma at the same radius is high (Fig. 5.2), thus, a ratio of $\tau_{\parallel}/\tau_{\perp}$ much smaller than 1 is expected [4]. From Eq. (5.10), one can estimate $\chi_{\perp}$ to be about *0.13×*$\tau_{\parallel}/\tau_{\perp}$, so the expected value must be very low, probably approaching the neoclassical one.

Similar conclusion can be made if one applies the extended Rutherford model [3, 8] to TEXTOR plasmas. From Eq. (2.27), the island growth can be written as follows (with all quantities taken at the resonant surface):

$$\frac{dw}{dt} = 1.22 \frac{\eta}{\mu_0} \Delta' - \left(\frac{0.9\eta j q}{B_\varphi \, \partial q/\partial\rho} \right) \frac{\widetilde{P}_T}{\chi_\perp T_e} \quad . \tag{5.13}$$

Here, Δ' is the stability factor depending on the local averaged ∇j, $\widetilde{P}_T$ is the total net power density per particle in the island, j is the current density. If the radiation losses are not important, the second term in Eq. (5.13) can be neglected. The island is growing linearly during the time interval of 0.65 – 0.8 s (see Fig. 5.4), and Δ' is calculated to be ~ 0.5. A faster growth starts after 0.85 s. As Δ' does not change very much, it means that $\widetilde{P}_T$ becomes negative due to the increasing radiation losses inside the island. It should be noted that at this time an enhancement in the C-IV line is observed by the VUV/XUV spectrometer (see Fig. 5.1). This is an indication that the impurity level has rapidly increased in a layer (of 2-3 cm) close to the wall, and the plasma edge has started to cool. Simultaneously, the temperature inside the island drops from 390 eV at 0.8 s to 190 eV prior to the disruption, yielding an increase of the radiation losses inside the island. Integration and solution of Eq. (5.13) gives: $\widetilde{P}_T/\chi_\perp \approx$ -1.1×10⁵ eV/m⁻². Since the temperature inside the island is dropping over 200 eV from 0.8 to 1.07 s, $\widetilde{P}_T$ is found to be in order of 1000 eV×s⁻¹ and, therefore, $\chi_\perp$ ~ 0.01 m²/s. This is in agreement with the result obtained by using Eq. (5.10), and much less than the global heat diffusivity of about 1.5 m²/s following from the energy confinement time τ_E of 30 – 40 ms for the NBI-heated plasmas at TEXTOR.

5.1.3 Some aspects of modes rotation in TEXTOR plasma

The rotation of the large MHD modes in TEXTOR has been extensively studied in the past [1]. However, using the unique feature of the ECE-Imaging system to observe a vertical line of sight in the vicinity of the $q = 2$ surface at the LFS, it is possible to study the island rotation in the poloidal direction. A typical example is shown in Fig. 5.6(a), where the large $m/n = 2/1$ mode inverts its toroidal rotation direction at ~ 0.565 s due to co-NB injection, and locks to the wall at ~ 0.63 s. As can be seen from the contour plots in Fig. 5.6(c) and (d), the total island rotation velocity projected on the poloidal direction is about 1100-1200 m/s and 300-350 m/s before and after the rotation inversion, respectively. For this shot, no $m/n = 1/1$ mode activity has been observed. Taking into account that the magnetic island is a helical structure rotating with the plasma, the diamagnetic frequency (due to the electron diamagnetic current) f^*_e can be calculated for the time of the rotation inversion [17]:

$$f_{MHD} = n\frac{\mathrm{v}_{tor}}{2\pi R_0} \pm m\frac{\mathrm{v}_{pol}}{2\pi r} + mf^*_e \quad , \tag{5.14}$$

where m and n are the poloidal and toroidal mode numbers, v_{tor} and v_{pol} are the toroidal
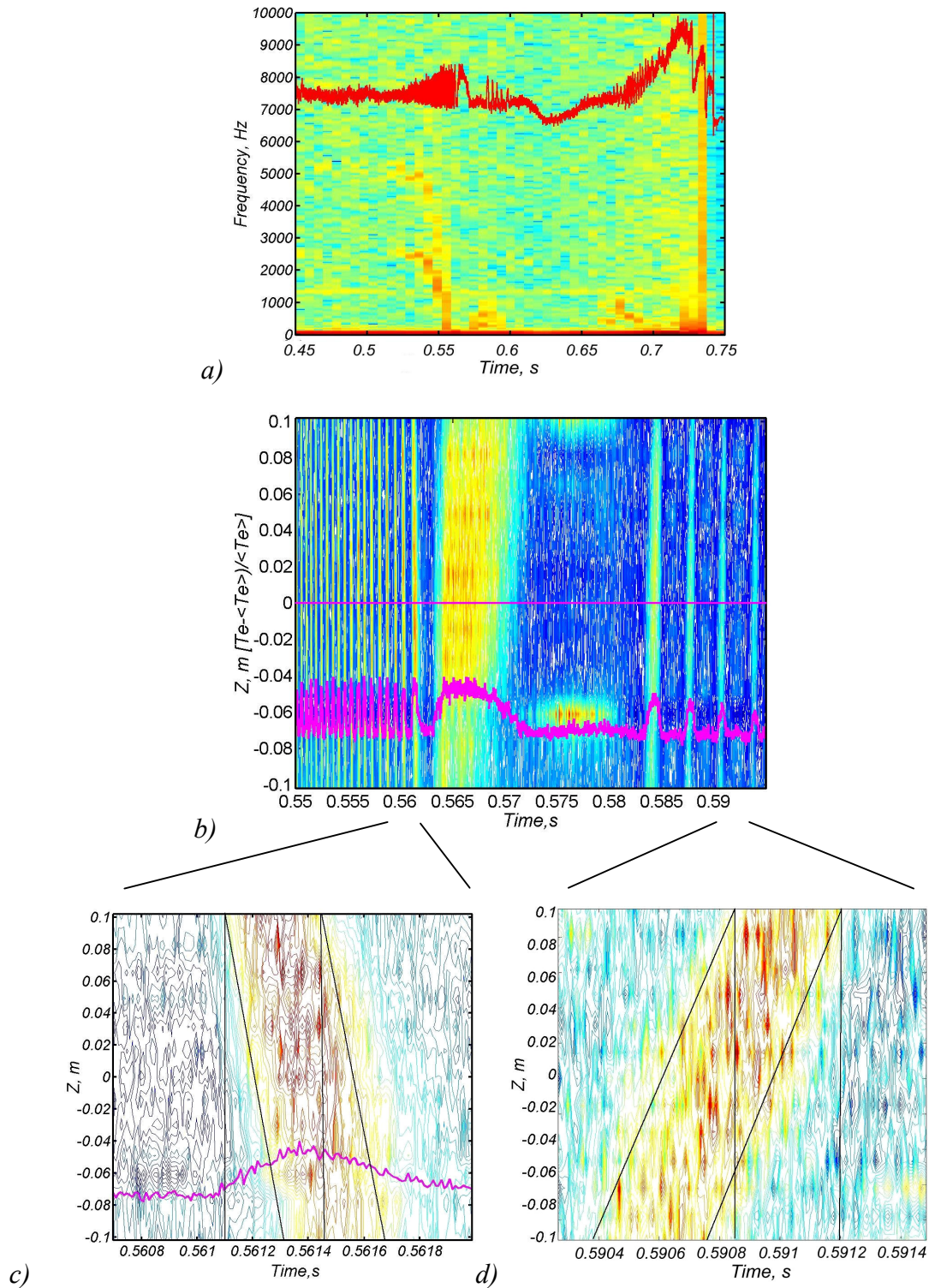
FIG. 5.6. (a) A large m/n = 2/1 mode and its spectrogram as monitored by the ECE-Imaging system. The rotation inversion occurs at ~ 0.565 s; (b, c, d) contour plot of the normalized temperature measured by ECE-Imaging. The position of the central channel is shown by the dotted line. The hot spot at z = -0.06 is due to the noise of the channel at this position. Lines in (c, d) match the X-point propagation and are being used to calculate the projection of the mode rotation velocity on the poloidal direction.

and poloidal ion fluid velocities, respectively, and the sign depends on whether or not the toroidal magnetic field is oriented in the same direction as the plasma current. In Eq. (5.14), it has been assumed that the MHD eigenfrequency is negligibly small. The electron diamagnetic frequency (that is due to the electron diamagnetic current) is given by:

$$ f_e^* = \frac{1}{2\pi e n_e B_\varphi} \frac{1}{r} \frac{\partial p_e}{\partial r} \approx \frac{1}{2\pi e B_\varphi r} \frac{\partial T_e}{\partial r} \quad , \tag{5.15} $$

under the assumption that the electron density does not change too much in the vicinity of the $m/n = 2/1$ island. The toroidal velocity, in its own turn, consists of the components parallel and perpendicular to the magnetic field line, $v_{tor}^{\parallel}$ and $v_{tor}^{\perp}$. This means that the ECE-Imaging measurement of the rotating island is not able to distinguish between purely poloidal velocity component and the toroidal rotation velocity of the helical mode projected on the poloidal direction. As it will be shown below, in some cases the poloidal rotation is quite essential and, therefore, cannot be neglected.

As has been described before, at ~ 0.575 s the mode rotation direction has been reversed. At this moment $f_{MHD} = 0$, and Eq. (5.14) can be rewritten as:

$$ \frac{1}{B_\varphi} \frac{\partial T_e}{\partial r} = \left[\frac{n}{m} \frac{r}{R_0} v_{tor} + v_{pol} \right] . \tag{5.16} $$

From the CXRS diagnostic, one can derive a value for the ion toroidal rotation at $q = 2$ ($r_{q=2} = 0.37$ m) being 1.2×10^4 m/s (Fig. 5.7). The time averaged electron temperature gradient at $q = 2$ is about $1.3 - 1.5$ keV/m, yielding the ion poloidal rotation velocity v_{pol} to be $\sim 580 - 850$ m/s.
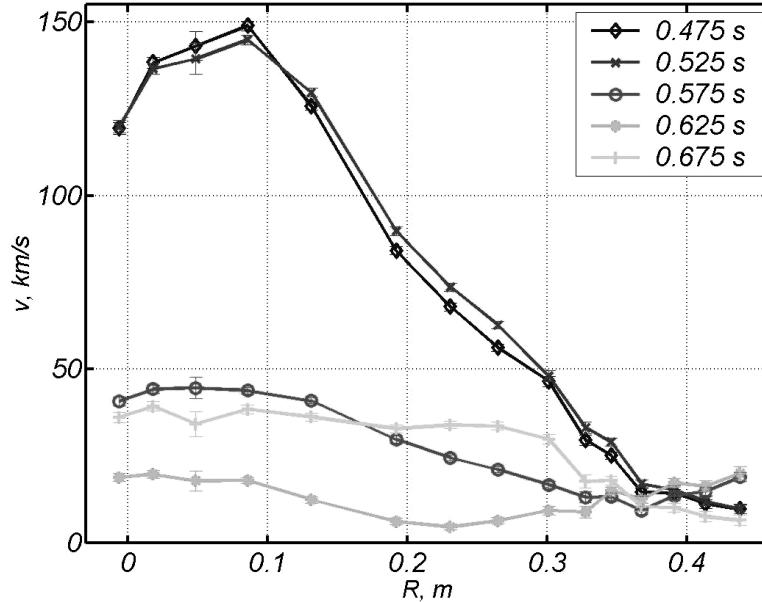
FIG. 5.7. The ion velocity rotation profiles for the same shot as in Fig. 5.6. The sampling rate of the CXRS system is 50 ms, meaning that fast changes in the toroidal velocity cannot be observed.

According to neoclassical theory [18, 19], the poloidal rotation can be written as:

$$v_{pol} = 5.33 \times 10^{-22} k \frac{c}{eB_0} \frac{\partial T_i}{\partial r} \ , \tag{5.17}$$

in which k is a numerical factor depending on the collisionality (in this case, $k \approx 0.4$), c is the speed of light, and dT_i/dr is the ion temperature gradient in the $q = 2$ vicinity. The CXRS measurements yield an ion temperature gradient of about 3.4 keV/m, leading to a poloidal velocity of 560 m/s. This is within the error bars comparable to the poloidal velocity determined with Eq. (5.16).

An interesting observation of a dynamic frequency behaviour of the $m = 2$ mode has been made in co-NBI heated TEXTOR plasmas [20, 2]. As can be seen in Fig. 5.8, acceleration of the mode frequency from 100 Hz to 800 Hz has taken place at 0.82 s in a very short time interval of a few ms. This effect has been observed shortly before the end of current ramp up. For this shot (#90311), no sudden changes in electron temperature and pressure profiles have been detected at 0.82 s. Thus, the diamagnetic frequency is not altered at this time. No change in the toroidal ion rotation has been observed too, albeit that the temporal resolution of the CXRS diagnostic (50 ms) is too poor to detect fast changes in the toroidal velocity. It should be noted that the impurity flux and, therefore, Z_{eff} are increased at this time, as evidenced from an enhancement of the H_α signal measured at the limiter. The increase in the mode frequency is correlated with a decrease in the frequency of the poloidal velocity v_{pol} at this time due to change in $\partial T_i/\partial r$.
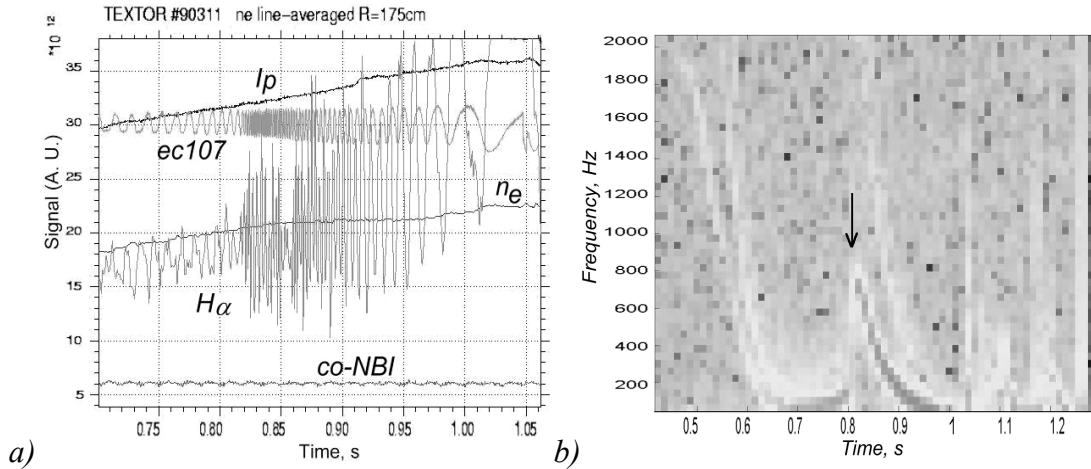
FIG. 5.8. Dynamic frequency behaviour of the mode in the ramp up phase of the discharge around 0.82 s (shot #90311, I=320 kA, n_e=2.1×10^{19} m^{-3}). The mode frequency is jumping from 100 to 800 Hz within a few ms. An enhancement of H_α signal during the frequency change is observed (a). A spectrogram for the 107 GHz ECE signal is given in (b). The arrow shows the time of sudden frequency increase.

Calculations performed for similar shots using Eqs. (5.14) – (5.17) have shown a good agreement with experimental data for f_{MHD} of $m = 2$ modes [2]. An example is shown in Fig. 5.9 for the discharge #90314. This shot is an example of the plasma recovery due to counter-injection. In the co-injection ($P = 200$ kW) phase ($t < 0.86$ s), the rotation profile is flat with $v_{tor} = 7 - 13$ km/s. In the case where the counter-NBI is switched on ($P = 0.8$

MW), a step of $\Delta v_{tor} = 15$ km/s in the rotation profile appears at $R = 2.08$ m, that is close to the $q = 2$ position. This step remains during the whole slowing down process and seems to reduce the fast decrease of the mode frequency as observed in plasmas without additional counter-NBI. In the latter case, the rotation profile remains flat and the $m = 2$ mode locks to the wall followed by a disruption.
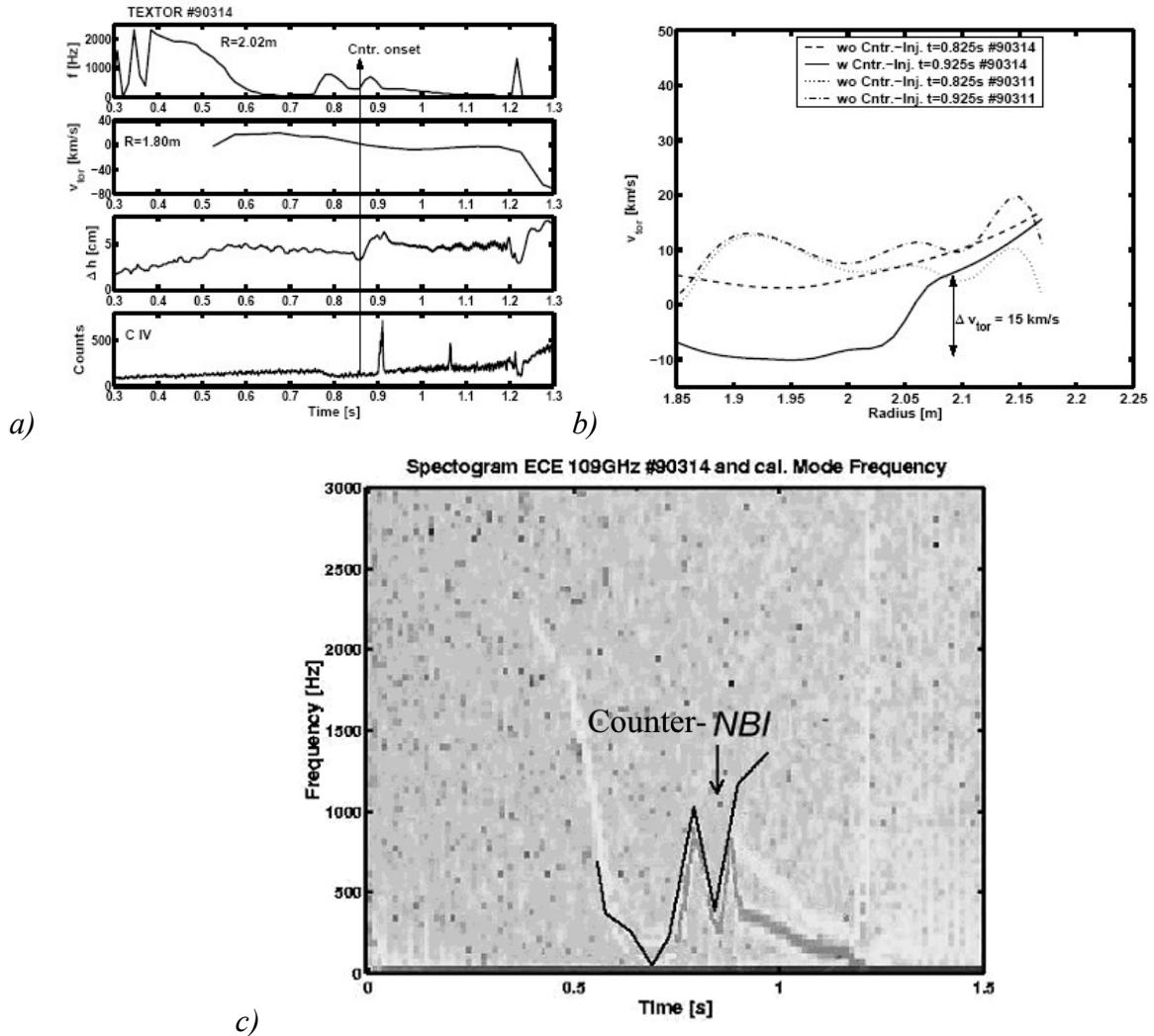
a)

b)

c)

FIG. 5.9. (a) Mode frequency for shot #90314 as observed by the ECE channel at 109 GHz (R = 2 m), the toroidal velocity deduced from the CXRS at R = 1.80 m, the horizontal plasma position from interferometer measurements, and C-IV emission line that exhibits an increase due to the plasma-wall contact at 0.9 s; (b) influence of counter-NBI on toroidal rotation profiles as observed by the CXRS for shots #90311 and #90314; (c) comparison between measured (spectrogram) and calculated (solid line) m/n=2/1 mode frequencies for the shot #90314 . The onset of the counter injector at t ~ 0.86 s is indicated by an arrow [2].

For this shot, calculations of the $m = 2$ mode frequency were done on the time grid of CXRS sampling rate [2]. Between $0.5 < t < 0.7$ s, a decrease of the mode frequency can be simulated quite well for an increasing $\partial T_i / \partial r$ (in this phase, $Z_{eff} = 2$). At $t \sim 0.8$ s, a decrease in the ion temperature gradient is observed that leads to an increase in the mode

frequency. The toroidal velocity and the diamagnetic frequency stay constant at this time. With the onset of the counter injector at $t \sim 0.86$ s, the diamagnetic frequency changes suddenly. The frequency of the toroidal velocity decreases less than expected for the counter-NBI phase, and the frequency of the poloidal velocity component does not alter. Thus, the calculated mode frequency f_{MHD} increases further with a maximum at $t \sim 0.9$ s, in agreement with the measured value.

It should be noted that in more standard TEXTOR discharges with strong momentum input given by NBI the toroidal plasma rotation of 10^5 m/s dominates the observed MHD frequency in Eq. (5.14) with only minor contributions from the poloidal rotation and the diamagnetic frequency.

If there are both $m = 1$ and $m = 2$ islands present in the plasma, it can be that f_{MHD} of the $m = 1$ mode is equal to that of the $m = 2$ mode while the local v_{tor}, as well as $\partial T_e / \partial r$, can be different in the $q = 1$ and the $q = 2$ vicinities. Modes with the same value of f_{MHD} are known as *coupled*. It has been shown in [17] that coupling of the 1/1 and 2/1 modes leads to a flattening of the rotation profile. However, if the NBI momentum input is not significant, contributions from the poloidal rotation and the diamagnetic frequency can play a role. If there is a large misbalance between co- and counter-NBI powers, the rotation profile will be peaked, and 1/1 and 2/1 modes can uncouple and rotate with different f_{MHD}.

The strong coupling plays an important role in plasma stability, because it can result in a disruption. Some mechanisms that lead to the disruption through the coupling between different modes will be discussed in Section 5.2.

Three-dimensional reconstruction of the large *m/n* = 2/1 mode

Using different ECE diagnostics, a 3D-mode reconstruction has been made for the same shot as in Fig. 5.1. The evolution of the $m/n = 2/1$ mode around the torus is shown in Fig. 5.10(a). The flat spot at the O-point is very pronounced, compared to the X-point. For this discharge, a 3/1-mode activity has been also detected (Fig. 5.10(b)). The $q = 3$ position is estimated to be at $R = 2.18$ m. From the ECE-Imaging system, a similar evolution in the poloidal direction is shown in Fig. 5.11(a). In Fig. 5.11(b) the temperature profiles from the vertically aligned ECE-Imaging diagnostic show how the vertical position of the X-point is changing in time.

In the contour plot in Fig. 5.12, for the radial set of ECE channels, the "hot" spot of the $m/n = 1/1$ mode is always in phase with the X-point of the $m/n = 2/1$ island at the LFS. This has also been observed at RTP [21]. In this shot, no sawtooth activity has been detected, so this kind of $m = 1$ island behaviour is typical for a slow precursor, when it couples to the $m = 2$ and $m = 3$ modes further outwards. This behaviour leads to a disruption (minor or major). Since the $m = 1$ mode does not show a clear tearing mode topology in this shot, the terminology of "hot" and "cold" spots, instead of X- and O-points, will be used. It should be noted that the $m = 1$ mode has a strong asymmetry with respect to the plasma centre at $R = 1.82$ m, so its "hot" spot is much more pronounced at the LFS than at the HFS. Both this and the radial $m/n = 2/1$ island asymmetries are an indication that ballooning-type effects are taking place. It can be seen in Fig. 5.13 that, unlike at the LFS, the large $m/n = 2/1$ island at the HFS is symmetrical with respect to the $q = 2$ position.

From Figs. 5.10, 5.11, 5.12 and 5.13, the full picture of the island phases at TEXTOR can be made. Figure 5.14 shows the mode topology for the phases when the O-

and X-points, respectively, are located in the equatorial plane at the LFS.
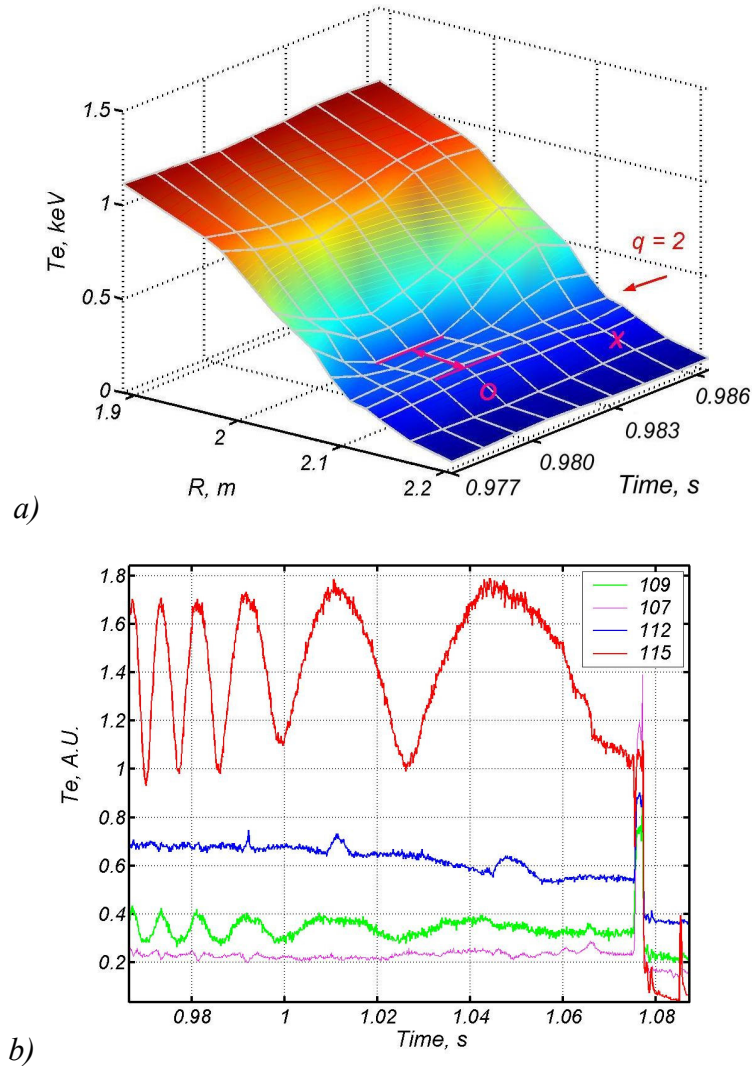

a)

b)

FIG. 5.10. The 3D-mode reconstruction for one rotation period around the torus. The O-and X-points of the m/n = 2/1 island are clearly visible. In the bottom plot, two ECE channels at 109 and 107 GHz indicate the presence of a 3/1 mode.

5.1.4 Evidence of a mode with higher *m* number associated with the large *m* = 2 island

One of the new results obtained recently with the ECE diagnostics at TEXTOR is the evidence of a small-scale mode associated with the large $m = 2$ island. In Fig. 5.15, a periodic increase of the temperature on top of the main $m = 2$ mode is seen by the fast ECE spectrometers at the HFS and by the 11-channel ECE radiometer at the LFS. Earlier, the same behaviour has been observed by the pulsed radar reflectometer in the density time traces [5]. In these shots, co- and counter-NBI with the same powers has been used. To make a proper estimation of m and n numbers for this mode, its location should be identified first. The $q = 2$ position is found to be at $R = 1.52$ m at the HFS and at $R = 2.11$ m at the LFS. It should be noted that the small-scale mode has appeared immediately after a minor disruption, and no traces of this mode have been found before. Some sawtooth
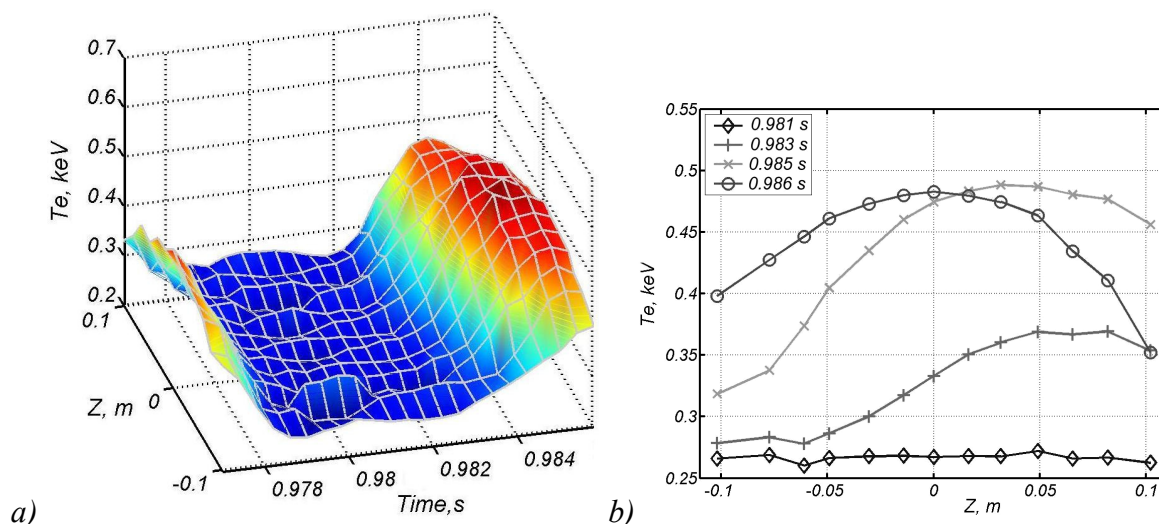
FIG. 5.11. The 3D-reconstruction of the m/n = 2/1 mode in the poloidal direction. The temperature profile at different times in (b) show how the X-point is moving through the viewline of the vertical set of ECE-Imaging channels.
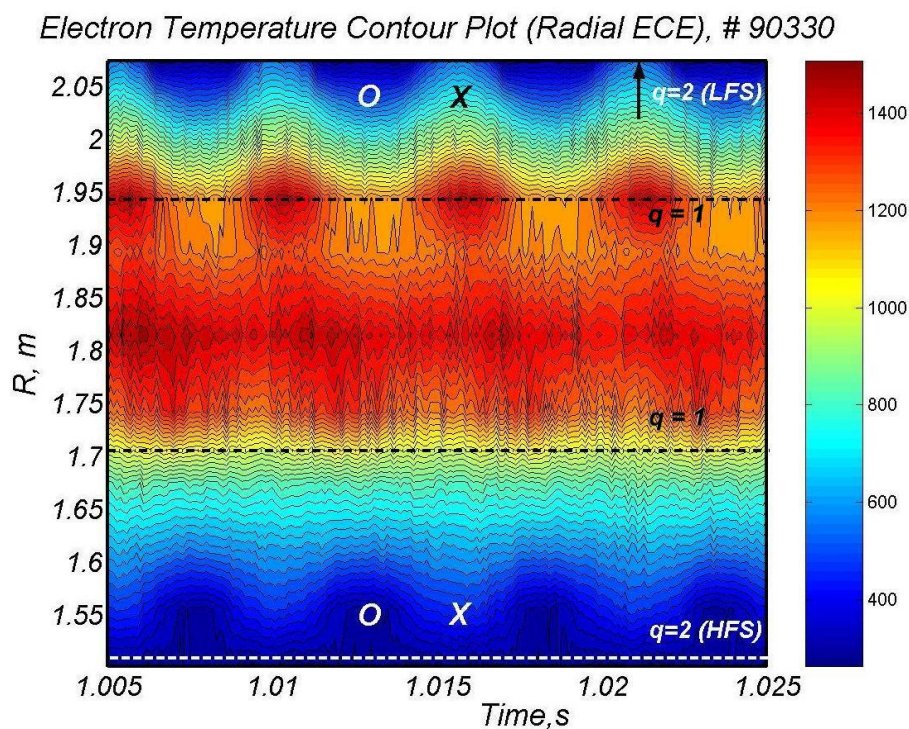
FIG. 5.12. Evolution of the m = 2 and m = 1 modes as seen by the radial set of the ECE channels. The central m = 1 mode is coupled to the m = 2 mode such that its "hot" spot is always in phase with the X-point at the LFS.

activity has been detected just after the minor disruption for about 6 ms, but then it has vanished (Fig. 5.16(a)), and an $m = 1$ mode develops with the same characteristics as described earlier in Section 5.1.3. Suddenly, the amplitude of the large $m/n = 2/1$ island is modulated by the small-scale mode. Analysis shows that the frequency of the small-scale mode is twice as high as that for the $m/n = 2/1$ island and equals to 1.3 kHz after the

disruption (Fig. 5.16(b)). This is also in agreement with the measurements performed by magnetic diagnostics, which show the presence of a mode with $n = 2$. The small-scale mode remains coupled with $m = 1$ and $m = 2$ modes up to a certain time, and then its frequency suddenly increases from 1.5 kHz to 3.7 kHz in a very short time interval of about 7 ms. At the same time, the $m = 1$ and $m = 2$ modes are still coupled and continue to slow down. There are two possibilities that could possibly lead to this kind of behaviour:

- The observed small-scale mode could be a 3/2 mode. From Fig. 5.15(a), a modulation caused by this mode is pronounced inside the $q = 2$ surface. From the ECE data, the location of $q = 1.5$ is estimated to be somewhere between $R = 1.97$ - 2.04 m at the LFS and $R = 1.56 – 1.62$ m at the HFS. The uncertainty of 6 - 7 cm is due to the large radial separation between channels at this position. However, the mechanisms which force the $m/n \approx 3/2$ mode to uncouple at some time from the strongly coupled $m = 1$ and $m = 2$ modes are not very clear. From the CXRS measurements, it follows that the toroidal ion velocity is very small at values of $3 – 7$ km/s in the vicinity of $q = 3/2$. This means that differences in the diamagnetic frequency and/or the poloidal ion velocity can create a large difference in f_{MHD} of the various modes. Thus, a sudden change in the local diamagnetic pressure could possibly cause the small mode to uncouple from the 2/1 and 1/1 ones.

- A higher-m mode with $1 < m/n < 2$. The break-up of the magnetic topology could lead to the creation of a chain of small islands with higher m and n numbers (for example, with $m = 6 – 12$ and $n = 2 – 4$, respectively) but with their ratio $1 < m/n < 2$. It is also probable that the 3/2 mode itself breaks up into this chain of small-scale islands. With the present spatial resolution of the ECE diagnostics this possibility could not be further investigated.
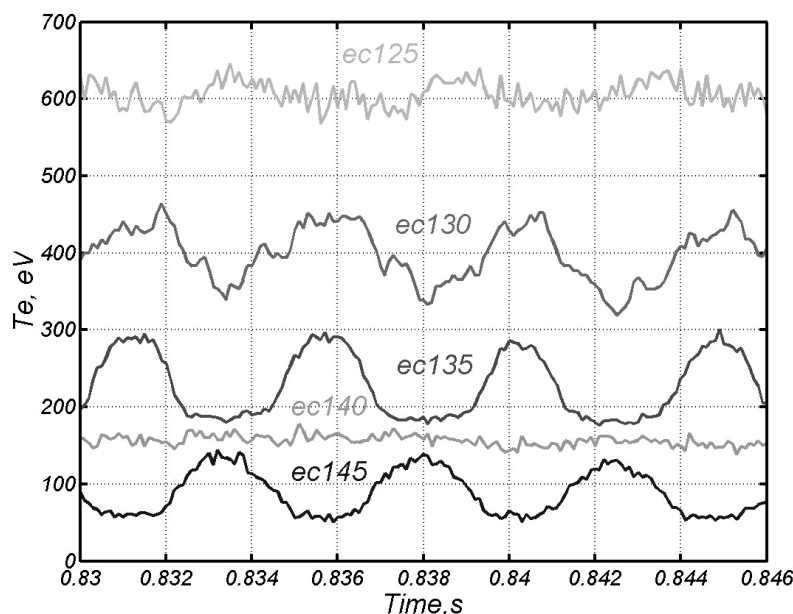
FIG. 5.13. Unlike at the LFS, a typical m/n=2/1 island is symmetrical at the HFS, with respect to the q = 2 position. The q = 2 position for this shot is determined from the phase inversion between two ECE signals at 135 and 145 GHz and approximately corresponds to the radius that is monitored by a channel at 140 GHz.
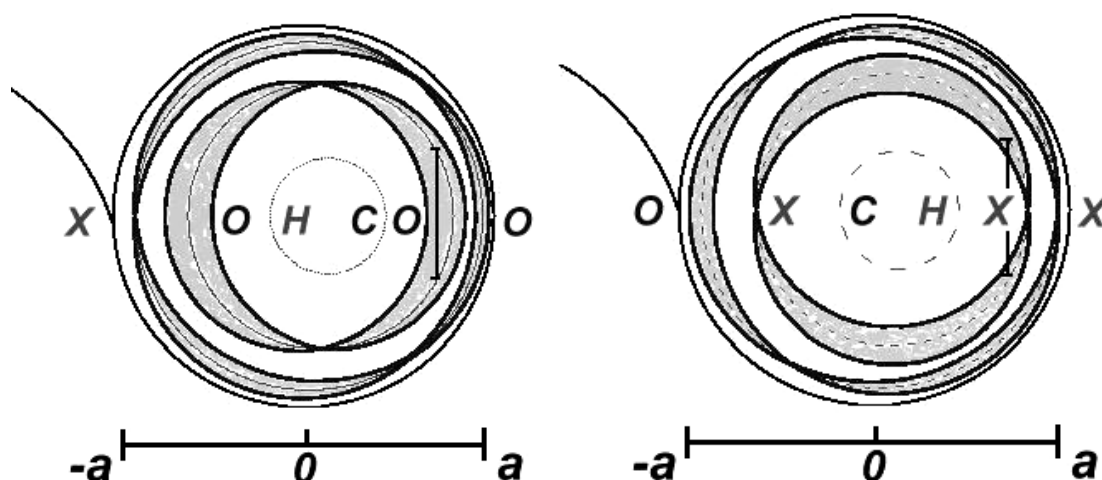
FIG. 5.14. Schematic drawing of the relative phases of the islands with different m numbers. The ECE-Imaging line of sight is shown at the LFS (magnetic field at a = 0 is 2.3 T).

Summary

Comparison between two models for the plasma transport properties inside the large MHD islands gives estimations of the heat diffusivities, which are much lower than the global plasma heat diffusivity. The 3D-reconstruction of large modes in TEXTOR allows modelling the island as a structure with closed flux surfaces. The main plasma heat flux flows through the X-point area probably along stochastic magnetic field lines. The perpendicular transport through the island is very much reduced. This is confirmed by a temperature profile flattening and even secondary peaking inside the island, compared to the X-point. The same observations have been made in the electron density profiles. It will be shown in Chapter 6 that the broadband temperature and density fluctuation measurements in the vicinity of the X-point confirm that the magnetic topology is probably stochastic there, compared to the O-point.

The mode rotation studies with the ECE-Imaging diagnostic have shown that the purely poloidal component of plasma rotation can be significant in some Ohmic and NBI-heated discharges at TEXTOR, especially when large modes are present with low toroidal ion velocity. It is confirmed that if the $m = 1$, 2 and 3 modes with $n = 1$ number are coupled, they have their X- or O-points in phase at the LFS. The large islands are almost always asymmetric at the LFS and symmetric at the HFS, although, the total island width is the same in both cases.

Both the ECE and the pulsed radar reflectometer diagnostics have confirmed the evidence of a small-scale mode with $1 < m/n < 2$. The mechanisms that force this mode to uncouple from the 1/1 and 2/1 modes are not very clear yet.
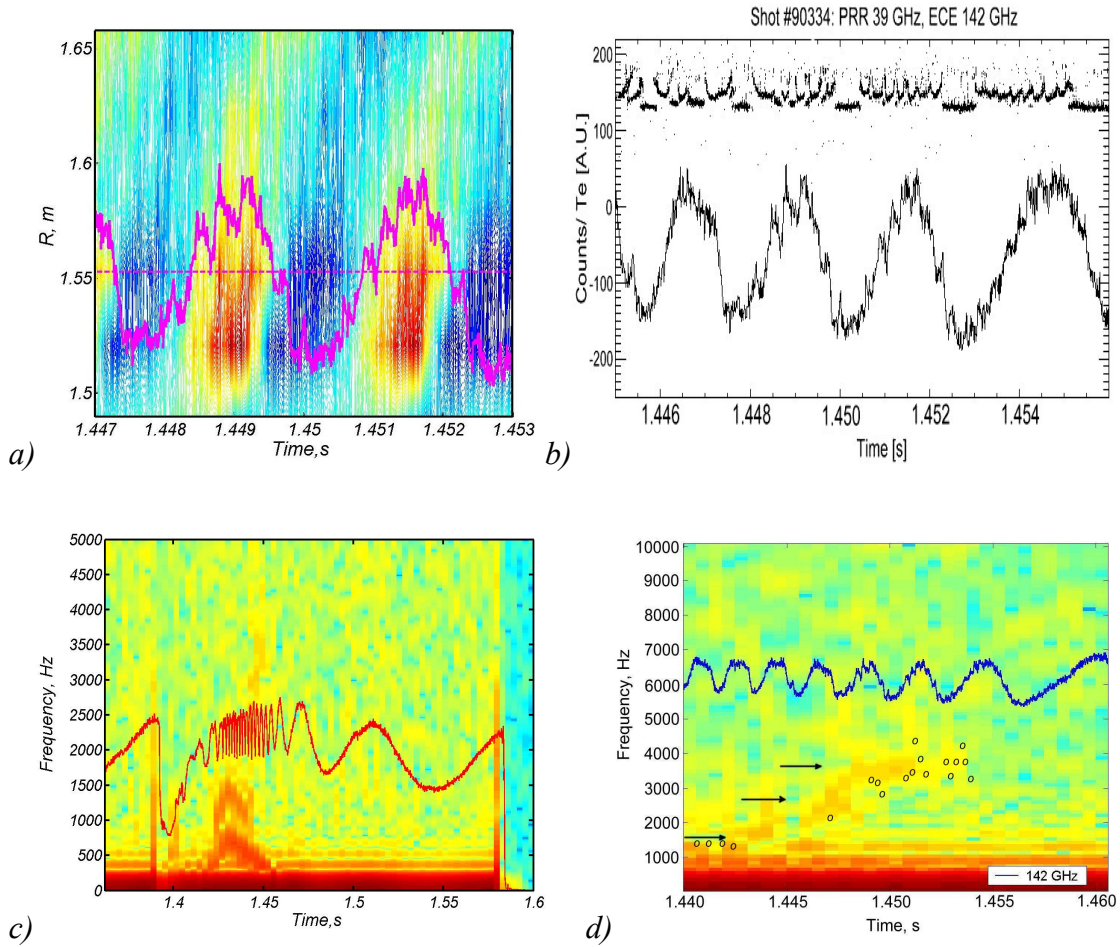
FIG. 5.15. Evidence for a small mode in TEXTOR: (a) – the contour plot shows periodical increase of temperature on top of the m = 2 mode, (b) – pulsed radar reflectometer (top) and ECE (bottom) raw signals clearly indicate the fast change in frequency for the high m modes between 1.447 – 1.455 s, (c) – spectrogram of the LFS ECE signal (107 GHz), (d) – spectrogram of the HFS ECE signal (142 GHz) with arrows showing the frequency change of the small-scale mode from 1.5 to 3.7 kHz, dots are results obtained with the help of pulsed radar reflectometer.

a)

b)
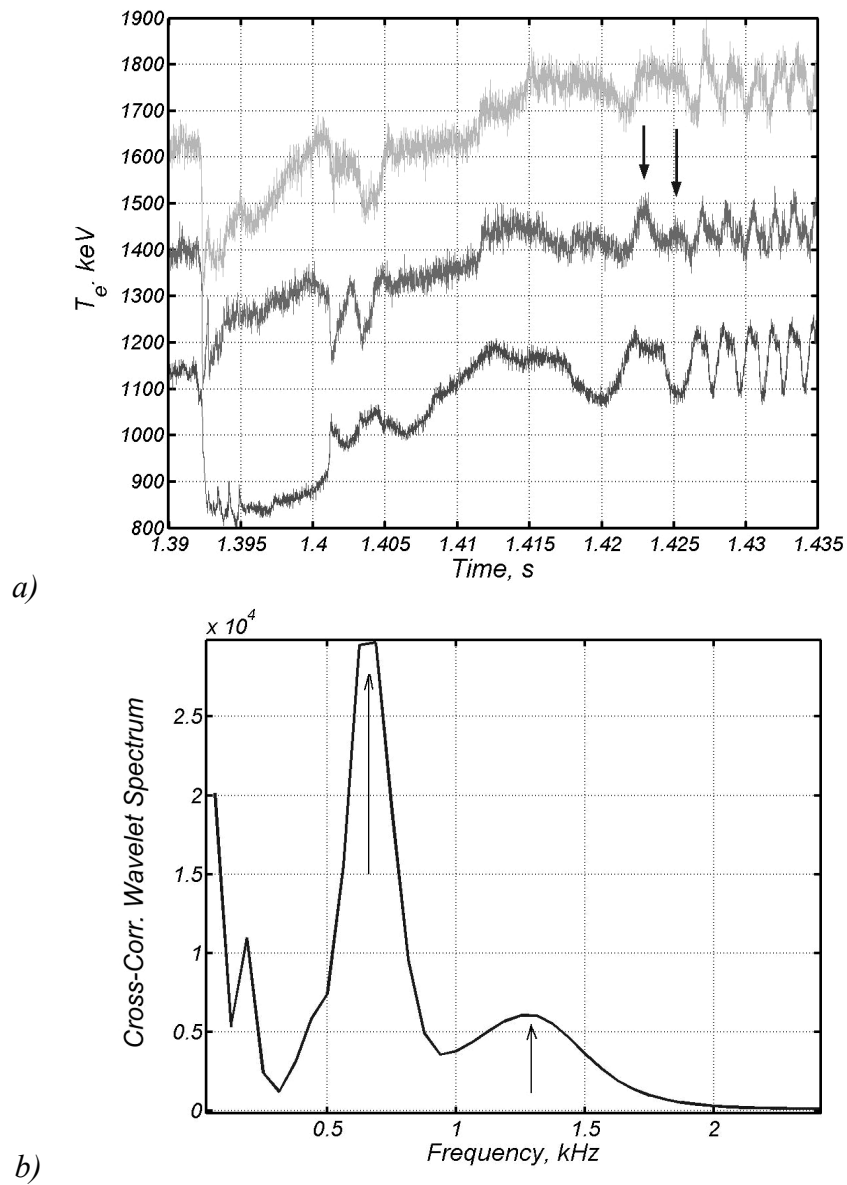
FIG. 5.16. The behaviour of the electron temperature as measured by ECE after a minor disruption (a) at q = 1.5. The mode with n = 2 can be seen soon after 1.42 s as a modulation on top of 2/1 mode oscillations and indicated by arrows. It is coupled to the m = 2 mode and has a twice as high frequency of 1.3 kHz, as can be seen from the cross-correlation wavelet spectrum obtained at the period from 1.42 – 1.435 s (b).

5.2   Disruption prevention scheme at TEXTOR[1]

Disruption instabilities in tokamak plasma are major concerns for the tokamak operation [2, 22, 23]. During the disruption, the enormous power flux deposited within a millisecond to the wall components can cause serious damage. That is why disruptions should be avoided or, if this is not possible, their effect should be mitigated as much as possible. At TEXTOR, a disruption prevention scheme has been recently introduced.

Disruptions at TEXTOR

At TEXTOR, two types of disruptions, minor and major, can be recognized. Unlike the major disruption, the minor one does not result in a termination of the discharge. The precursor in both cases is an $m/n = 2/1$ mode. Though, a role of $m/n = 1/1$ mode in provoking the major disruption can be very important too, because it destroys the magnetic shear in the plasma centre and triggers an $m/n = 2/1$ mode to develop [24]. However, the development of an $m/n = 1/1$ mode prior to the disruption is not always observable clearly enough by ECE. In Fig. 5.17, two electron temperature contour plots show the development of both types of disruptions. It can be seen that the plasma core (and, therefore, plasma current) survives during the minor disruption and the temperature profile recovers. Moreover, as evidenced by the VUV/XUV spectrometer measurements, the value of Z_{eff} drops, so the plasma becomes more "clean" [2, 25].

For the major disruption at TEXTOR, three different phases can be seen from ECE. The first phase is the development of the $m/n = 1/1$ and $2/1$ modes. The second one is the energy quench phase with one or more heat pulses. During the third phase, the current decay takes place. As can be seen in Fig. 5.17 (b, d), shrinking of the electron temperature profiles and steepening of the gradients is taking place prior to the disruption (in the rest of the paper, major disruption will be referred to as "disruption" simply). This is caused by a strong impurity flux from the wall to the core and, therefore, by an intensive plasma cooling. In order to avoid a disruption, one needs to develop an active control mechanism for use in the first phase of disruption. In the other two phases, only mitigation of disruptive effects is possible.

Method to avoid disruptions at TEXTOR

At TEXTOR, it is decided to use a large $m/n = 2/1$ mode as an indicator for an approaching disruption. A reliable method to detect this mode is based on the dynamic cross-correlation measurement of two ECE channels from the 11-channel radiometer located at the LFS and the HFS at the $q = 2$ surface [2]. As can be seen in Fig. 5.18, an ECE diagnostic, rather than an interferometer or magnetic coils, are best suited for the detection of the $m = 2$ mode. With a sampling rate of 10 kHz (see Section 4.1.1), the diagnostics is able to detect modes up to 5 kHz. A disadvantage of the ECE diagnostic is that it is very sensitive to the change in the magnetic field. When the $q = 2$ surface is properly located with respect to the ECE channels used in the cross-correlation calculation, the cross-correlation module generates a trigger that is used to start the neutral beam injection within a few *ms* after occurrence of the trigger. Alternatively an intensive

---

[1] This section is related to parts of an article with the title "*Heterodyne ECE diagnostics in the mode detection and disruption avoidance system at TEXTOR*" by A. Krämer-Flecken, K.H.Finken, V.S.Udintsev, H. Larue, accepted for publication in Nuclear Fusion (2003).

helium puff can be started to mitigate the disruption effects on the wall (see Fig. 5.19). The cross-correlation module is able to distinguish between $m = 2$ mode and sawtooth activity.
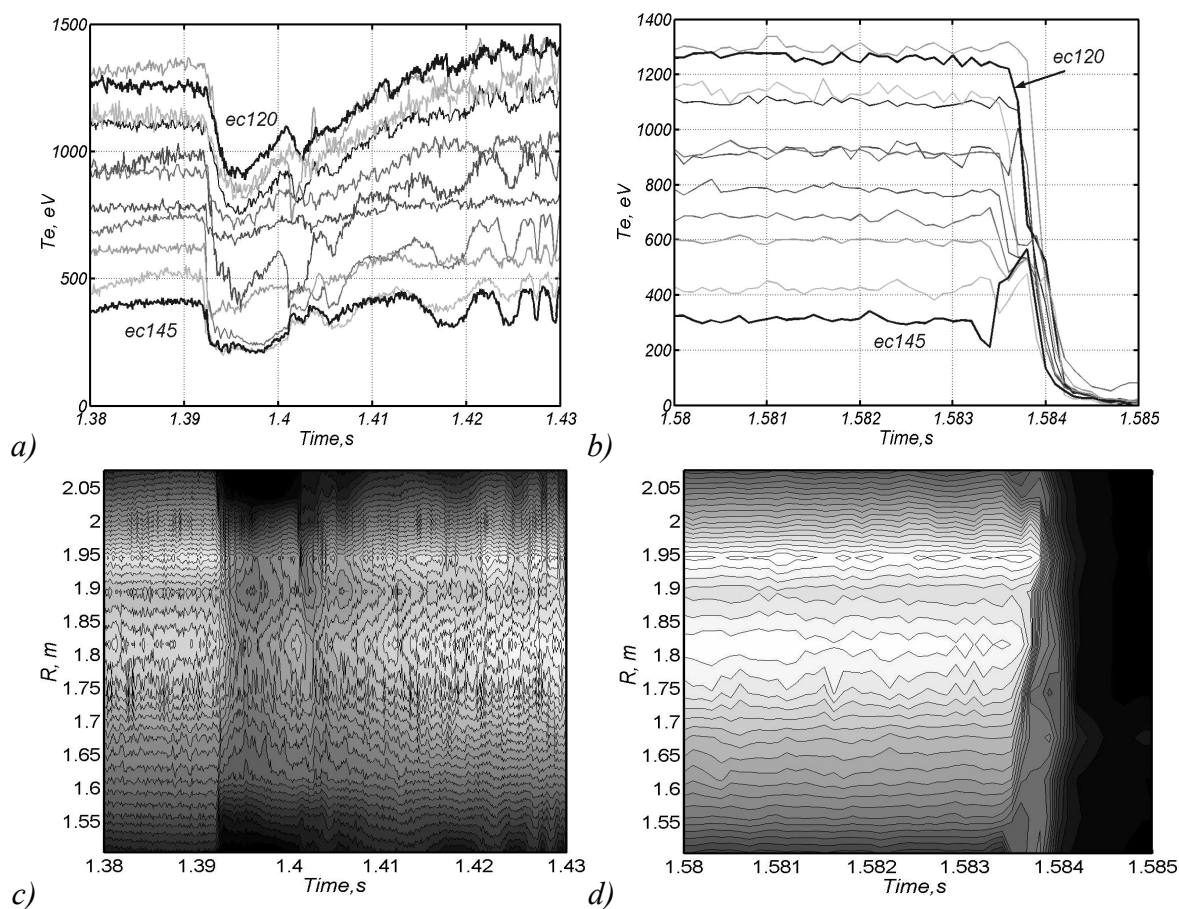

FIG. 5.17. Evolution of a minor (a - time traces, c - contour plot) and a major (b, d) disruptions as evidenced by ECE for the same shot as in Fig. 5.15. Unlike for the major disruption, the plasma core survives during the minor one. A large heat pulse characterizes an energy quench during the major disruption after 1.583 s.

Two sets of experiments have been performed. First experiments were done on Ohmic target plasmas with tangential co-NBI (power of 0.7 MW) that has been switched on by the trigger. Figure 5.20 shows the development of the large $m/n = 2/1$ mode and the transition to a sawtoothing plasma after onset of the co-injection. At 0.6 s, the mode width is estimated to be about 10 cm and its frequency decreases down to 200 Hz. At this time, the trigger is generated. The co-injection causes the velocity shear to decrease by flattening of the rotation profile, and the mode locks. At 0.64 s, a minor disruption occurs. After the minor disruption, the mode activity starts again but disappears soon. At 0.68 s, the $q = 1$ surface appears in the plasma, as evidenced by the sawtooth activity. The plasma recovery can be explained by an increased velocity shear between the $m = 2$ mode and the wall that prevents wall locking. The co-NBI is switched off when the trigger disappears. The sawtooth activity remains, and the discharge is terminated by a normal current ramp down. The described behaviour is quite reproducible for $0.5 \leq P_{\text{co-NBI}} \leq 0.7$ MW. For smaller or higher power values the plasma disrupts. The lower limit can be explained by

the missing toroidal momentum. For TEXTOR, about 0.2 MW is needed to stop the mode rotation, and an additional 0.3 MW are necessary to build up the velocity shear. The upper limit for the added co-injection power can be explained by the perturbation level induced in the already disrupting plasma [2].
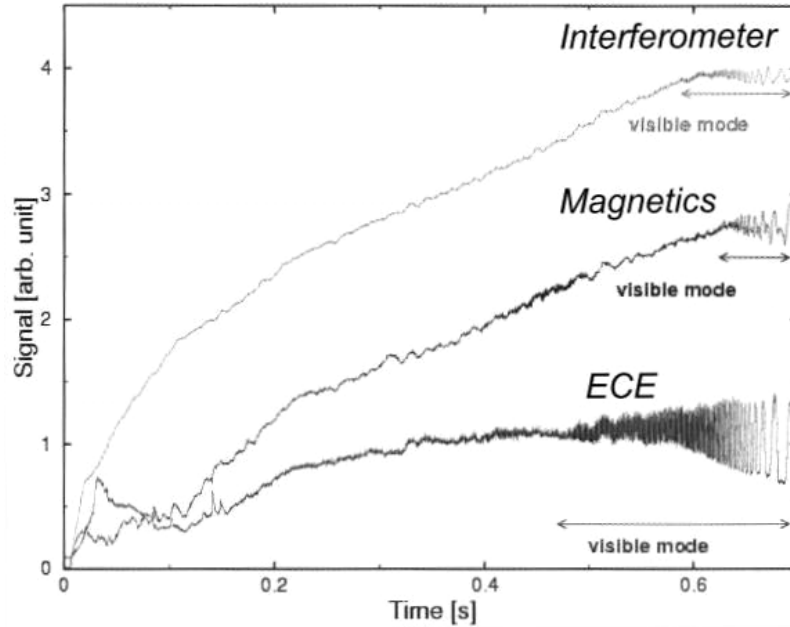

FIG. 5.18. A large m = 2 mode is much earlier detected by the ECE, compared to the density interferometer and magnetic coils. However, ECE is very position sensitive [25].
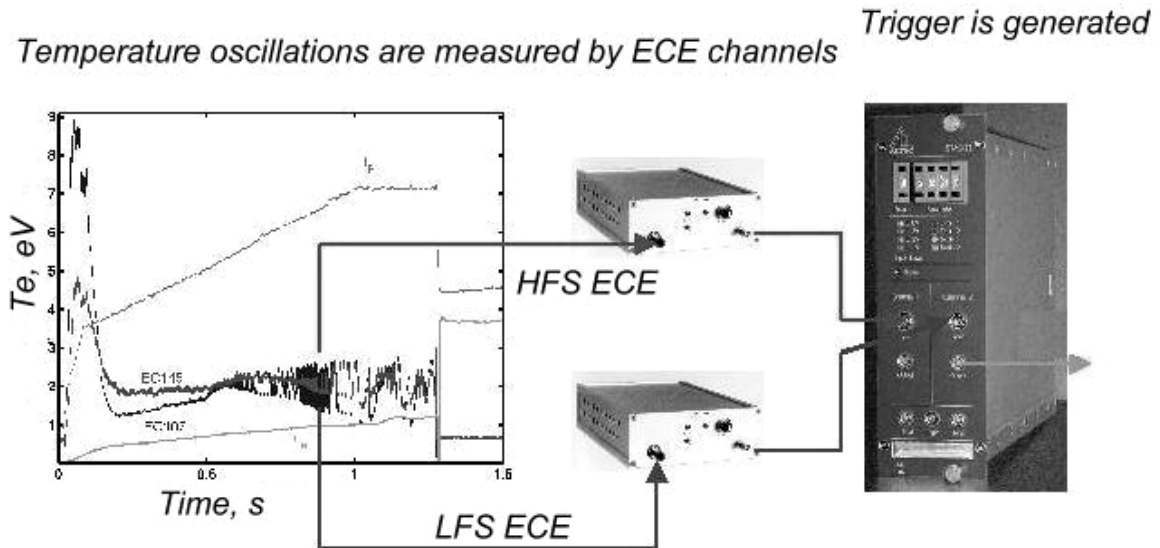

FIG. 5.19. Scheme of the cross-correlation mode detector at TEXTOR. If the m = 2 mode is detected, the trigger is generated, and the neutral beam injection starts within 8 ms after the trigger [25].
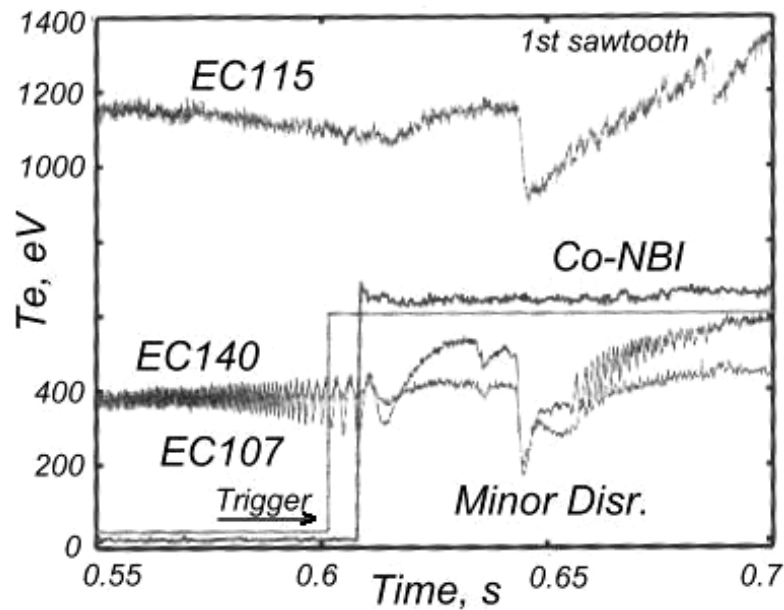
FIG. 5.20. Disruption avoidance for Ohmic heated plasma. The trigger and co-NBI onset are shown [25].

A second set of experiments has been done with the use of both co- and counter-injectors. A typical example is shown in Fig. 5.21 for the same shot as in Fig. 5.9. To support the mode development, co-NBI with a power of 200 kW has been applied at 0.5 s to flatten the toroidal rotation profile and to increase the width of the $m = 2$ island. The mode can be seen by ECE at 0.55 s, and its frequency drops with the onset of co-NBI (see Fig. 5.9). The trigger switches on 1.2 MW of counter-NBI at 0.85 s, and the mode frequency increases. However, no change in the toroidal rotation has been observed with onset of counter-NBI, and the toroidal rotation profile remains flat up to the minor disruption at 1.2 s (see Section 5.1.3). The sawtooth activity appears at 50 ms after the minor disruption, and the central toroidal rotation velocity drops to $v_{tor} = -80$ km/s. The plasma profile changes too. Up to 1.233s the profile is flat for $1.49 \leq R \leq 1.55$ m. Within 2 ms a gradient develops over this radial range. This behaviour is typical for all analysed discharges. After 1.9 s the counter-NBI is switched off and the rotation profile becomes similar to those at 0.5 s. The discharge was successfully terminated some time later.

Mitigation of disruption effects by He-gas puffing

To suppress runaway electrons that are created during a disruption [26], a massive amount of the noble gas He is injected into the TEXTOR plasma. The strong increase in density prevents electrons to be accelerated and become runaway. He-gas has a low Z number, and therefore it has a small probability to be implanted in the wall and can be easily pumped away by the turbo-molecular pumps behind the limiter. If the $m = 2$ mode appears, the trigger opens the valve, and the injection of up to 10 mbarL of helium into the vessel is possible in less than 1 ms. The valve is mounted directly on the TEXTOR vessel. If one assumes sound speed propagation, the gas reaches the plasma within 1 ms. It has been found that after disruptions mitigated by a He-puff indeed runaway generation is prevented and the subsequent discharges always showed a good breakdown [2, 23].
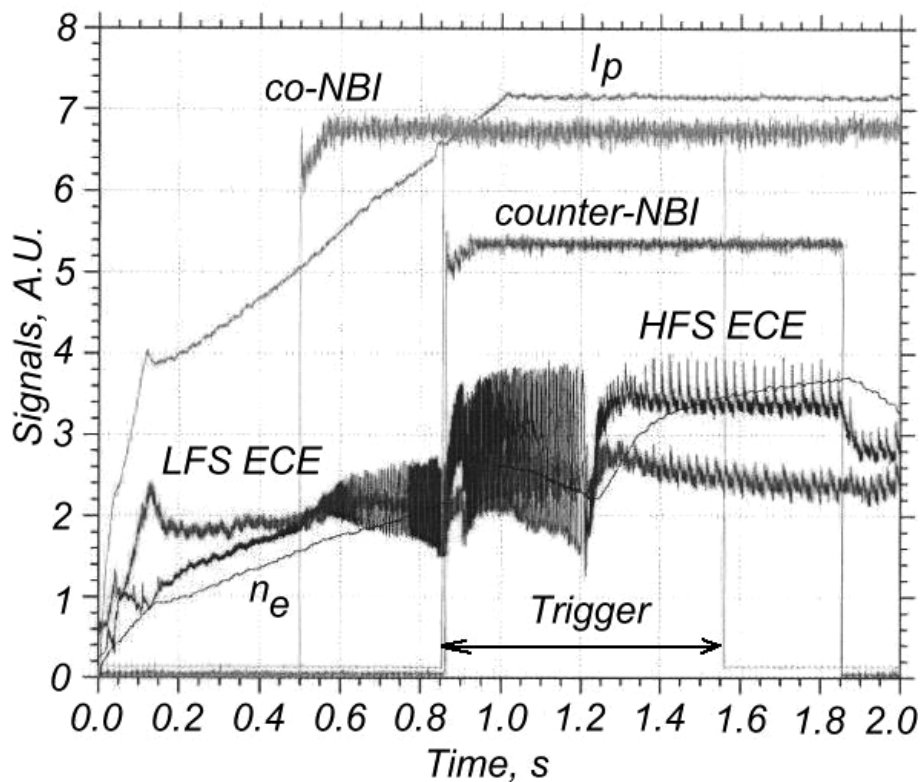
FIG. 5.21. An example of disruption avoidance with both co- and counter-NBI (the same shot as in Fig. 5.9). The m = 2 mode is detected at 0.55 s, and the counter-NBI is switched on by the trigger at 0.85 s. After the minor disruption, sawtooth activity is observed, and the discharge is terminated successfully some time later [25].

Acknowledgement

References

[1]   P.C. de Vries *et al*., Nucl. Fusion **37**, 1641 (1997).

[2]   A. Krämer-Flecken *et al*., "*Heterodyne ECE diagnostic in the mode detection and disruption avoidance at TEXTOR*", accepted for publication in Nucl. Fusion (2003).

[3]   P.H. Rutherford, PPPL Report-2277 (1985).

[4]   B.Ph. van Milligen *et al*., Nucl. Fusion **33**, 1119 (1993).

[5]   J.C. van Gorkom *et al*., in Proc. of the 5th Int. Reflectometry Workshop, Toki, Japan (2001), published as NIFS Research Report NIFS-PROC-49, p. 59-63 (2001).

[6]   V.S. Udintsev *et al*., in Proc. of the 12th Joint Workshop on ECE and ECRH, p. 215 (Aix-en-Provence, May 13-16, 2002), edited by G. Giruzzi (World Scientific, Singapore, 2002).

[7]   R. Fitzpatrick, Phys. Plasmas **2**, 825 (1995).

[8]   F. Salzedas *et al*., Phys. Rev. Lett. **88**, 075002 (2002).

[9]   H. Soltwisch, Plasma Phys. Control. Fusion **34**, 1669 (1992).

[10]   L. Spitzer, R. Härm, Phys. Rev. **89**, 977 (1953).

[11]   J. Wesson, *Tokamaks*, Clarendon Press, Oxford (1997).

[12]   J. Rapp *et al*., Forschungszentrum Jülich Report Jül-3697 (1999).

[13]   D. Hogeweij, *Private Communications* (2002).

[14]   V.S. Udintsev *et al*., in Proc. of the 27th EPS Conf. on Control. Fusion and Plasma Phys., Budapest, Hungary, Eur. Conf. Abstr. Vol. **24**B, 948 (2000).

[15]   B.Ph. van Milligen *et al*., Rev. Sci. Instrum. **74,** 3998 (2002).

[16]   R.B. White, D.A. Monticello, Phys. Fluids **20**, 800 (1997).

[17]   P.C. de Vries *et al*., Plasma Phys. Control. Fusion **39**, 439 (1997).

[18]   R.D. Hazeltine, Phys. Fluids **17**, 966 (1974).

[19]   V.I. Bugarya *et al*., Nucl. Fusion **25**, 1707 (1985).

[20]   V.S. Udintsev *et al*., in Proc. of the 28th EPS Conf. on Control. Fusion and Plasma Phys., Funchal, Portugal, Eur. Conf. Abstr. Vol. **25**A, 85 (2001).

[21]   F. Salzedas, Thesis Universiteit Utrecht (2001).

[22]   S.V. Mirnov *et al*., Phys. Plasmas **5**, 3950 (1998).

[23]   G. Mank *et al*., in Proc. of the 28th EPS Conf. on Control. Fusion and Plasma Phys., Funchal, Portugal, Eur. Conf. Abstr. Vol. **25**A, 1469 (2001).

[24]   S.V. Mirnov, *Private Communications* (2003).

[25]   A. Krämer-Flecken, *Private Communications* (2003).

[26]   R.D. Gill, Nucl. Fusion **33**, 1613 (1993).

Chapter 6

Temperature fluctuation measurements in TEXTOR plasmas and their relation to MHD modes

Studies of electron temperature fluctuations in magnetically confined plasmas can shed some light on the nature of the turbulent transport [1 - 4]. At the TEXT-U experiment, investigations on the role of high-frequency electrostatic fluctuations in anomalous heat transport in the tokamak were performed by means of the ECE cross-correlation technique [1]. It has been stated that long wavelength modes (with poloidal wave number ≤ 1 cm^{-1}) cannot account for the observed transport. As was concluded from far-infrared scattering measurements, shorter-wavelength electrostatic turbulence could still be responsible for the transport, albeit that the spatial resolution of this type of measurement is poor. Moreover, the influence of magnetic fluctuations on electron heat transport has not been fully investigated up to now, and often is neglected, as is the mutual interaction between macroscopic MHD-modes and small wavelength broadband turbulence.

In the TEXTOR tokamak, first measurements of temperature fluctuations were recently made by means of ECE diagnostics. Low frequency (kHz) oscillations are associated with the presence of MHD modes with different *m* and *n* numbers. Broadband high frequency (10-100kHz) has been observed as a manifestation of fine-scale turbulence. Their spectral properties depend strongly on the plasma parameters (rotation velocity, electron temperature, density, and their gradients), as well as on whether or not additional heating is applied. Interestingly the high frequency turbulence localized around macroscopic MHD modes appears to be modulated by these modes as if the change in characteristics travels with the rotating MHD-modes

The correlation technique that is being used at TEXTOR has been described in Section 4.2. Here, only a short reminder is given. Two different types of ECE diagnostics are utilised for temperature fluctuation studies: an ECE-Imaging system with vertical line of sight and a number of conventional radial radiometers. Two schemes were used to realise fluctuation measurements with sufficiently low statistical error:

(1) because of the relatively small poloidal separation between the ECE-Imaging channels of about 1.5 cm combined with an observation spot size of 1.3 – 2 cm, this system is a powerful tool for the study of sufficiently large temperature fluctuations and enables to measure correlation lengths in the vertical direction;

(2) even with a single line of sight and a single channel, the spectrum can be evaluated from the autocorrelation function under certain assumptions. The thermal noise generates a peak around zero time lag that should be subtracted from the autocorrelation function. Subsequently, a Fourier transform can be applied to the remainder. The resulting spectrum can be used for temperature fluctuation studies (see Fig. 6.1). This scheme can be used by any of the ECE systems with a post-detection bandwidth much larger than the width of the temperature fluctuation spectrum.
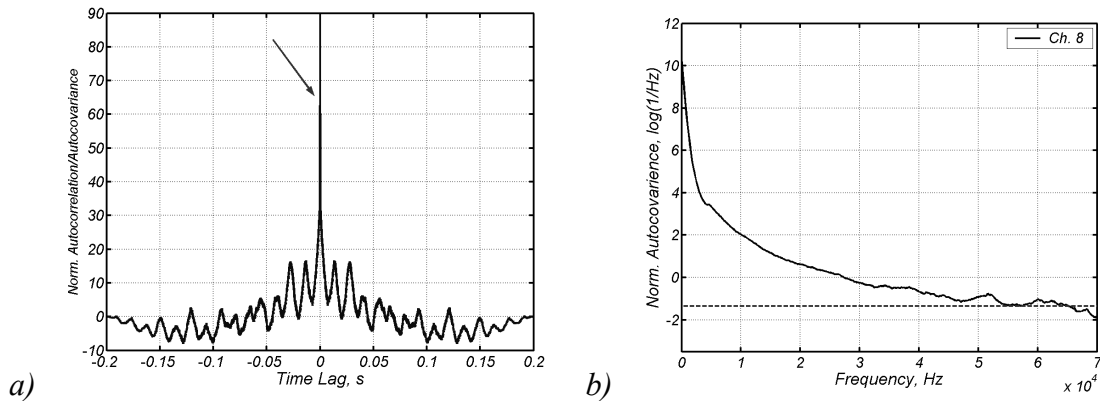
FIG. 6.1. The thermal noise generates a peak around zero time lag in the autocorrelation function (channel 8 of the ECE-Imaging diagnostic, B_t = 2.19 T, ECRH), as indicated by the arrow (a). After subtraction of this peak, a fast Fourier transformation is applied to the autocorrelation function. The resulting autocorrelation spectrum (b) is normalised to the r.m.s. value. The dashed line shows the statistical noise level for this spectrum.

6.1 Studies of *m* = 1 precursor to sawteeth

Figure 6.2(a, b) shows the development of the precursor in an ECR-heated discharge prior to a sawtooth crash as seen by the channels of the radial ECE radiometers. For this shot (B_T = 2.14 T), the sawtooth inversion radius is very close to the position of the 107 GHz channel. The amplitude of the oscillation changes strongly over the time interval between 2.105 − 2.109 s. The precursor oscillation is nicely seen inside the inversion radius, but is not showing up outside q = 1.

The unique feature of the ECE-Imaging system to observe the plasma at 114 GHz along a vertical line of sight has been used to study the poloidal evolution of the precursor. From the cross-correlation between two channels above and below the equatorial plane (Fig.6.3a), the MHD frequency and the projected poloidal rotation velocity of the *m* = 1 precursor prior to the crash at 2.109 s has been estimated to be about 4.2 kHz and 2 km/s, respectively. From the surface plot and time traces in Fig. 6.3(b, c) one can see that measured temperature contours exhibit some kind of 'bending behaviour' around the equatorial plane, as it propagates along the line of sight of the ECE-Imaging system. From the poloidal reconstruction of the plasma region that is been monitored by the ECE-Imaging, it can be concluded that the *m* = 1 precursor has an elongated shape and is hot. Moreover, the axis of rotation (being probably the magnetic axis) is 2 cm above the midplane (Fig. 6.3(d)). In addition to the ECE-Imaging, data from the radial ECE diagnostics has been used to make a full reconstruction of the precursor from *r* = 0 to 0.15 m, both with the coordinate transformation and the Shafranov shift taken into account. The plasma is assumed to rotate as a rigid body. The effect of precession induced by the vertical displacement of the magnetic axis causes the temperature surfaces of the rotating island to 'bend' on the surface plot.

The obtained reconstruction is generally in agreement with results obtained in TEXT-U with ECE [3] and in JET [5]. At JET [6] and at the FTU tokamak [7] (see Fig. 6.4), Soft X-Ray (SXR) tomography has been used to investigate *m* = 1 like oscillations induced by pellet injection. Since SXR radiation is proportional to $n_e^2 T_e^{1/2}$, high emission can be expected where the temperature is low and the density is high. Topologically, Figs.

6.3(d) and 6.4 are complementary. Interestingly, it therefore appears that the *m = 1* sawtooth precursor is a 'hot island' as a crescent surrounding of a cold and dense bubble as predicted by Kadomtsev [8]. Standard tearing mode theory is therefore not applicable here.
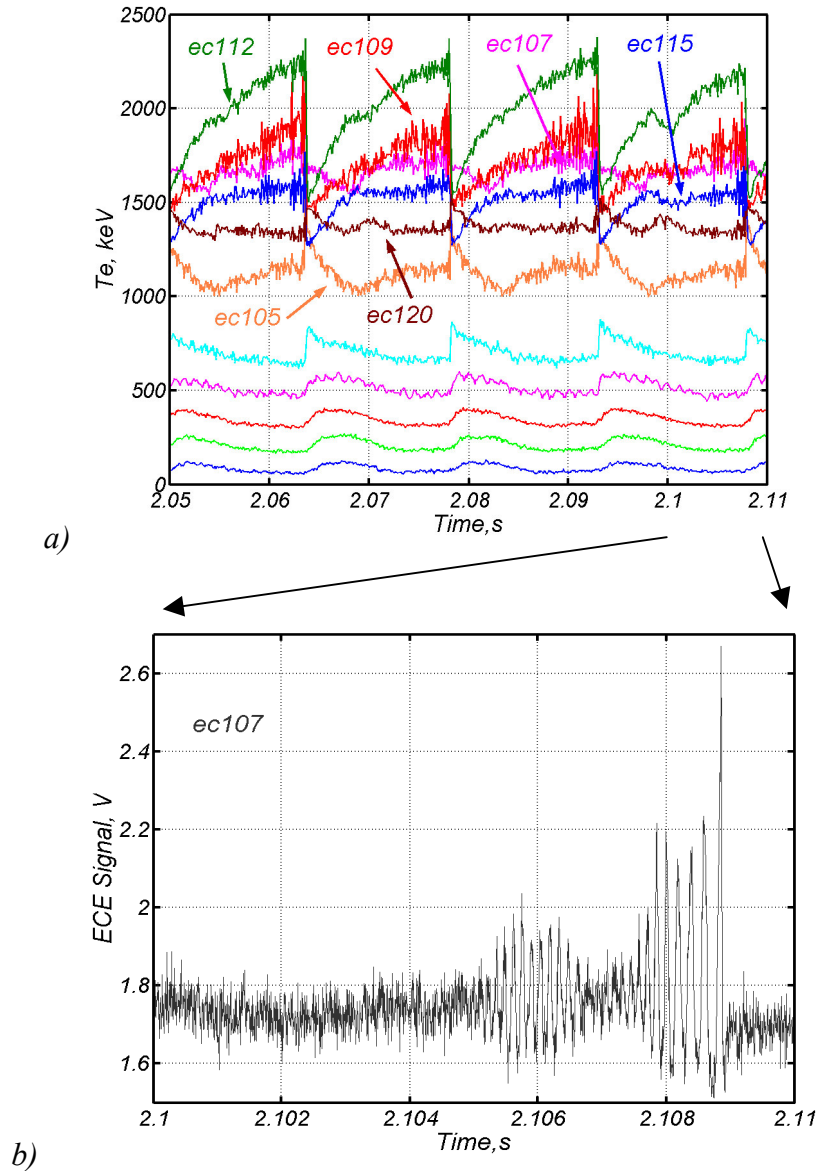

a)

b)

FIG. 6.2. Dynamic behaviour of a large m = 1 precursor as observed by the radial ECE radiometer channels. Outside the q = 1 radius (e.g. the channels with inverted sawteeth), no oscillations due to the precursor are observed (a). The bottom traces represent the temperature evolution as measured at the HFS outside q = 1. A strong change in amplitude can be seen from about 2.105 s to 2.109 s (b).
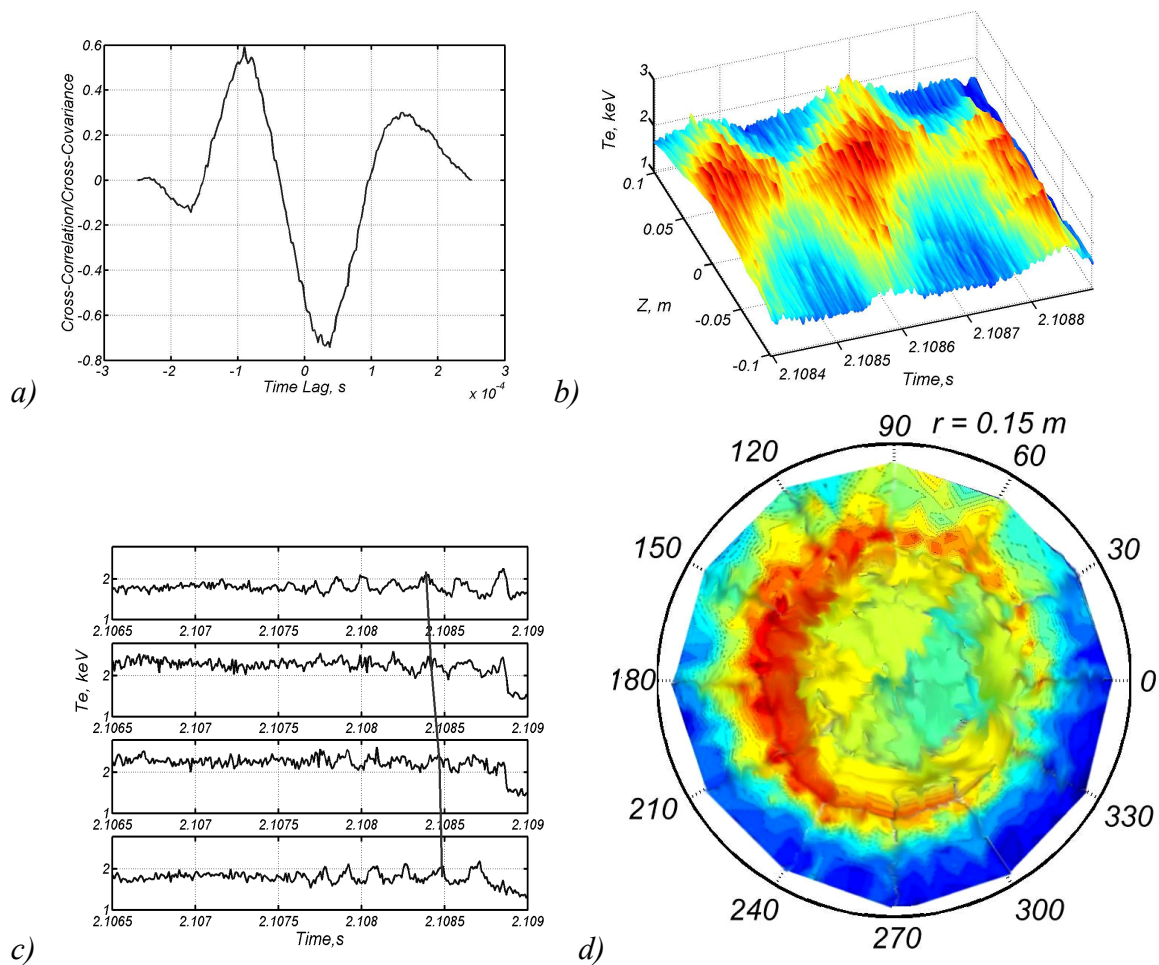
FIG. 6.3. From the cross-correlation between two channels above (#14) and below (#3) the equatorial plane, displaced by 18 cm (a), the MHD frequency and the projected poloidal rotation velocity of the m = 1 precursor prior to the crash is estimated to be about 4.2 kHz and 2 km/s, respectively. A surface plot (b) shows that temperature profiles are "bending" around Z = 0. An asymmetry can also be seen on time traces (c; channels 3, 8, 10, 13). The propagation of the 'hot spot' (i.e. the O-point) of the precursor is shown by a curved line. From the poloidal reconstruction (d), it can be seen that the m = 1 has an elongated shape, and it is displaced with respect to the midplane. Oscillations with higher frequencies are probably caused by an artefact induced by an imperfect calibration of the ECE-Imaging. Contour smoothing has been used to improve the quality of the figure.

At TFTR [9], a 'hot spot' elongated in the radial direction has been observed. In [10], it has been suggested that in low magnetic shear configurations or in the case of strong current perturbations, 'positive' magnetic islands can form in local regions with positive current modulation together with the usual 'negative' magnetic islands, in which the modulation of the perturbation currents is negative. The 'positive' islands can be a reason for the 'hot spot' in the plasma centre during a sawtooth crash.

However, a verification of some crucial plasma properties in the core, such as the magnetic shear or presence of strong current perturbations, is needed if one wants to use this model to explain TEXTOR observations.
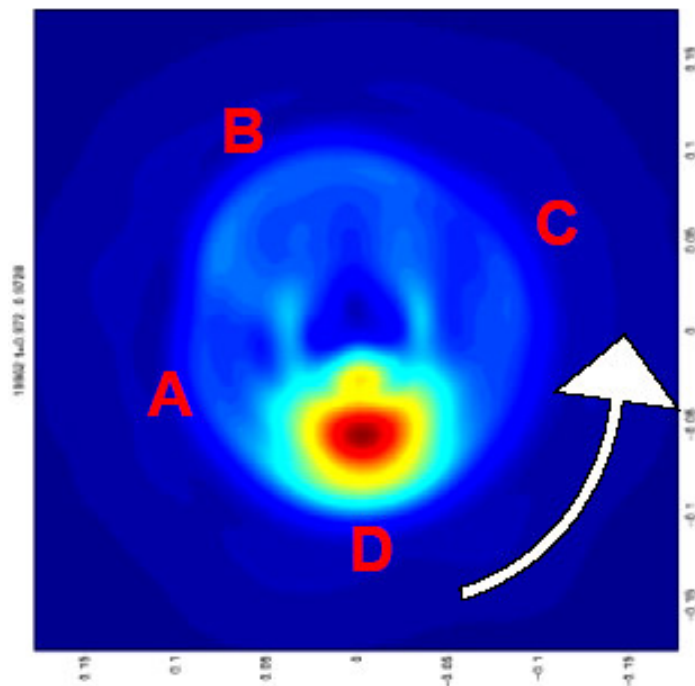
FIG. 6.4. An m = 1 mode tomographic reconstruction of SXR data in the FTU tokamak [7]: A, C – footprint of the X-point, B – a displaced hot core, D – an O-point. As evidenced from this figure, temperatures in the O-point are higher, compared to the X-point and the displaced core. An arrow shows the direction of rotation.

6.2 Temperature fluctuations in the vicinity of the X, O-points of a large *m* = 2 mode

As has been shown earlier in [11], the broadband density fluctuations in the presence of the large *m* = 2 mode at TEXTOR, as obtained from the measurements of the amplitude of the signal by a pulsed radar reflectometer, are enhanced at the X-point of the island, compared to its O-point (see also Fig. 6.5). The temperature fluctuations have been measured by analysis of the signals of neighbouring ECE-Imaging channels. When frequency bands are very close, they correspond to mostly overlapping sample volumes, so that the r.m.s. value and cross power spectrum of the local T_e fluctuations can be calculated from the cross-correlation between these signals. The adjacent channels are slightly displaced above and below the midplane on the LFS. The principles of the temperature fluctuation measurements by this method are described in detail in Section 4.2.

For this analysis, the time interval of one mode oscillation (Fig. 6.6(a)) for the same shot as in Fig. 5.1 has been subdivided into several windows. The mean temperature was subtracted from the signals and subsequently they were subjected to a wavelet transform, which rather than a Fourier transform, gives better accuracy for the relatively short data records and does not average the spatial information [12]. One should note, however, that these time intervals are very short, so the accuracy in determination of exact fluctuation frequencies and amplitudes is rather low even for the wavelet transform, so mainly a qualitative analysis can be made. The present observations are in agreement with those for density fluctuations. The wavelet cross-spectrum shows an enhancement of the

broadband temperature fluctuations near the X-point, compared to the O-point of the $m = 2$ island (Fig. 6.6(b)). It is necessary to mention, however, that the spectra obtained for the r.m.s. values of the fluctuations, normalized to the mean value of the temperature for each time window (Fig. 6.6 (d, e), see the method described in [4]), do not show a significant difference between O- and X-points.

If one uses a mixing length argument, one derives for $\widetilde{T}_e / \nabla T_e$ a length scale of 1 cm at the X-point and 4 cm at the O-point. The latter value comes close to the island width of 5 cm. In conclusion one can say that the turbulence characteristics are quite different: at the X-point small-scale lengths at high frequencies; at the O-point long scale lengths at low frequencies, probably associated with the rotating MHD island (Fig. 6.6 (c)).
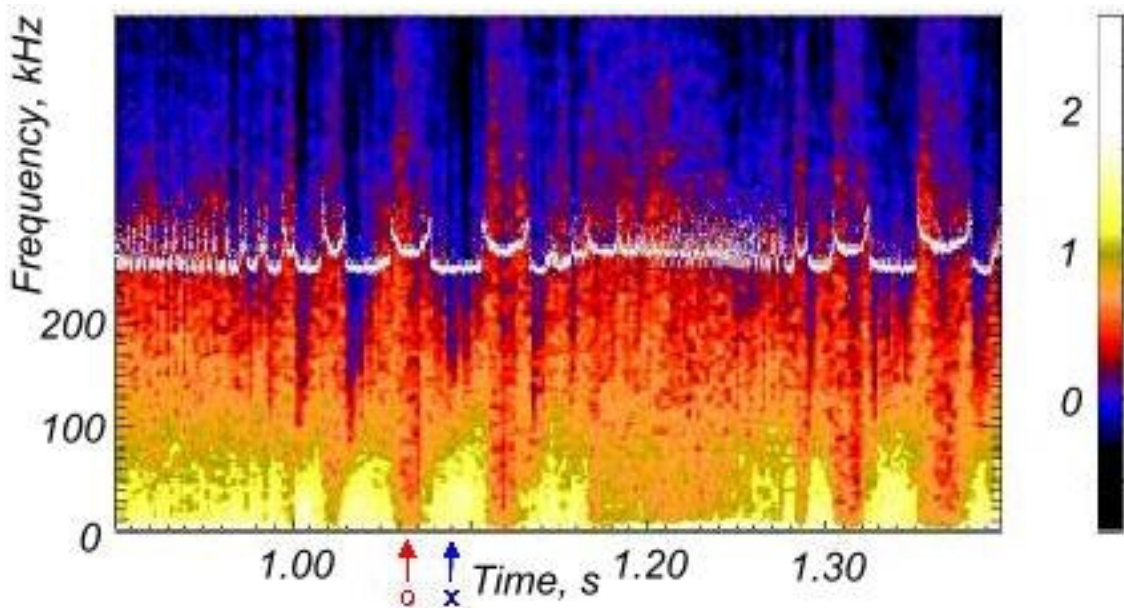
FIG. 6.5. Power spectrum of a pulsed radar reflectometer channel (33 GHz, LFS) shows an enhancement of density fluctuations below ~ 100 kHz at the X-point of the m/n = 2/1 island, compared to the O-point [11]. In this figure, light colour corresponds to a higher power.

6.3 Temperature fluctuations around $q = 1$ and outside $q = 2$

To gain a better understanding of the turbulent transport in the plasma core, electron temperature fluctuations in the ECRH regime have been studied by means of ECE. Two shots with central magnetic field values of 2.25 and 2.19 T have been chosen. In both shots, ECRH has been applied between 2.0 – 2.25 s (see Fig. 6.7, for the shot at 2.25 T).

For the shot with $B_t = 2.19$ T, channels 4 to 14 of the ECE-Imaging are located inside $q = 1$, as seen from the inversion of sawteeth. Channels 1, 2, 3 and 16 monitor the plasma temperature outside $q = 1$. of which only channel 3 is suitable for analysis. For the shot with $B_t = 2.25$ T (shown in Fig. 6.7) only channel 8 monitors the plasma inside the $q = 1$ radius, while the others are located outside $q = 1$.
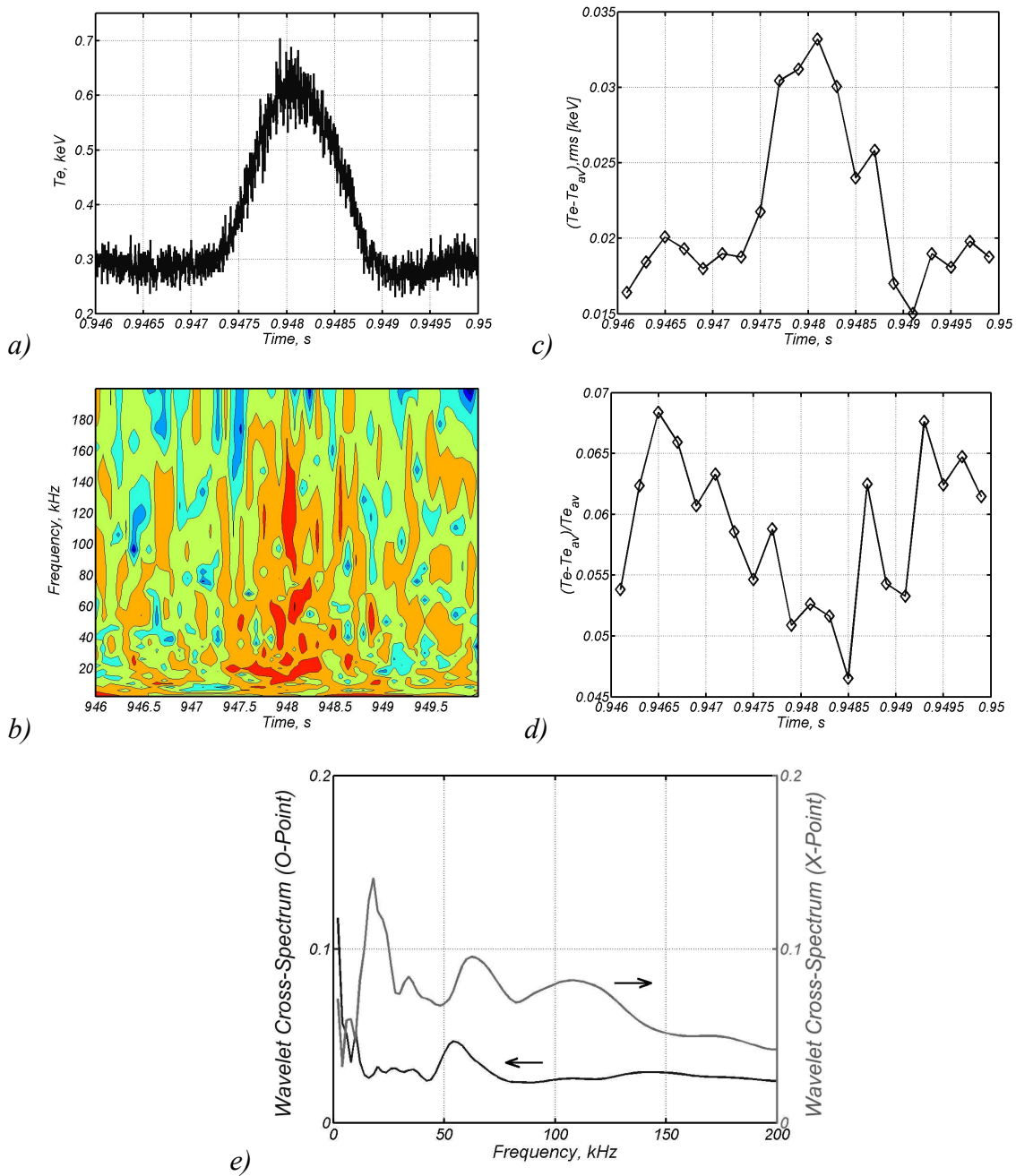
FIG. 6.6. The (wavelet) cross-spectrum (b, dark colour corresponds to a higher power) of two adjacent ECE-Imaging signals (a; only one signal is shown) shows an enhancement of the temperature fluctuations in the X-point vicinity of a large m = 2 mode. Wavelet power spectra for the O-point and the X-point (e) shows that these fluctuations are in the frequency range of 20 – 150 kHz, though higher frequencies dominate the turbulence characteristics for the X-point, compared to the O-point. The r.m.s. values for the mean-removed signal (c), as well as the normalized r.m.s. values (d), are given for comparison.

Figure 6.8 (a, b) shows the cross-power spectra between different ECE-Imaging channels that monitor the plasma outside and inside the $q = 1$ surface normalized to the r.m.s. for these two shots. To minimize as much as possible the statistical noise level, all spectra were obtained by averaging over sawtooth periods during the whole or a large part

of the ECRH phase. It is also desirable to calculate the cross-correlation between odd and even channels, in order to get rid of any spectral 'pollution' caused by the technical implementation of ECE-Imaging in the TEXTOR hall. It can be seen that the amplitude of the cross-power spectrum between two channels is significantly lower for channels on different sides with respect to the $q = 1$ surface than between channels on the same side of $q = 1$, even though the cross-correlation has been done between channels well above and well below the midplane. For the shot with $B_t = 2.19$ T, the weakest cross-correlation is observed between channels 8 and 3, whereas the cross-correlation between channels inside $q = 1$ is high (Fig. 6.8(a)). However, for the shot with $B_t = 2.25$ T, the weakest cross-correlation is observed between channel 8 (inside $q = 1$) and any of the channels outside $q = 1$ surface. The conclusion of these observations must be that the turbulent structures inside and outside $q = 1$ are separated. The $q = 1$ surface acts as a sort of a barrier. This is in good agreement with observations from heat pulse propagation measurements [13], which showed that the $q = 1$ surface acts as a barrier for thermal transport
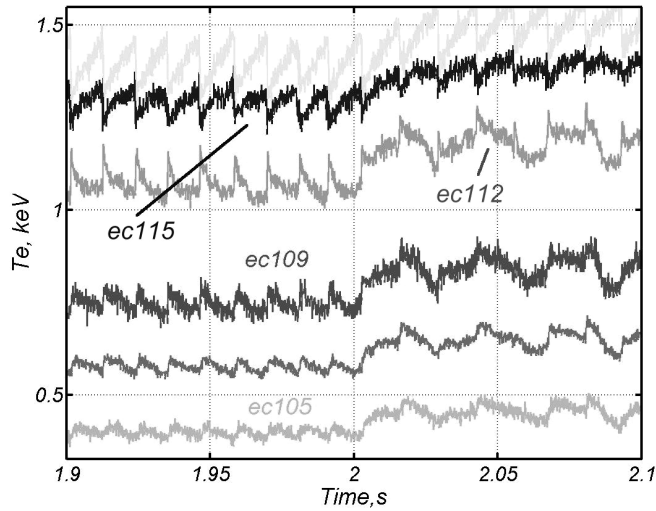

FIG. 6.7. Electron temperature behaviour during ECRH switch-on at 2 s, as evidenced by the radial ECE channels. Inversion of sawteeth occurs between channels at 115 and 112 GHz. For this shot, the central magnetic field is about 2.25 T. Only a part of the ECRH phase is shown.

For the shot where most of the channels are inside the $q = 1$ radius (e.g. $B_t = 2.25$ T), it is possible to estimate the poloidal correlation length of the fluctuations. Because the central channel 8 is looking almost through the plasma core in this shot, and under the assumption that flux surfaces inside $q = 1$ are symmetrical in their geometry, with respect to the core, one can assume an equivalence between vertical and radial correlation lengths in this shot. The strongest correlation is observed between channels 7, 8 and 9 of ECE-Imaging. Cross-correlation between channels 7 and 10, as well as between channels 8 and 5, is somewhat lower in the frequency range between 2 – 70 kHz than the cross-correlation between channels 8 – 9, 7 – 8 and 7 – 9, but still much higher than the cross-correlation between channels 8 and 3, so a distance of about 2 – 2.5 cm is taken as an estimate for the correlation length l_{corr}. From the cross-phase analysis, eliminating low frequency (< 10 kHz) components related to the pure MHD activity, a decorrelation time t_{decorr} of about 70 μ s is found. Thus, for $l_{corr} \sim 2$ cm, the value of the heat diffusivity inside the $q = 1$ radius is estimated to be:

$$\chi_e \sim l_{corr}^2/t_{decorr} \sim 6 \text{ m}^2/\text{s} , \qquad\qquad (6.1)$$

This value is in good agreement with values obtained from power balance analysis inside q = 1 [14]. However, errors in these estimations can be quite significant due to a relatively high statistical noise level at higher frequencies. In future, these measurements will be done with a high-performance ECE correlation technique, as described in Section 4.1.3.
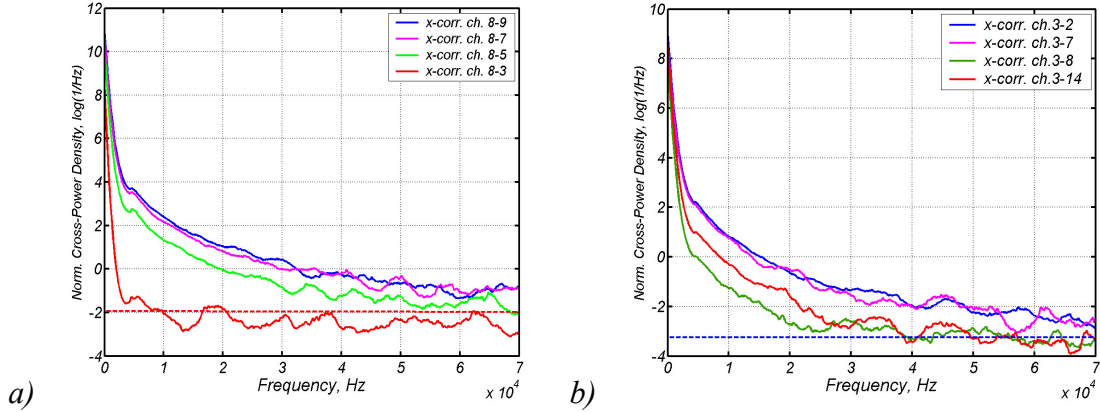

FIG. 6.8. Normalized cross-power densities as obtained from the cross-correlation between ECE-Imaging channels on the same side and on different sides of the q = 1 surface. For the shot with the magnetic field of 2.19 T (a), channel 5, 7, 8 and 9 monitor the plasma inside q = 1, whilst channel 3 is outside q = 1. For B_t = 2.25 T (b), channel 8 is the only channel inside q = 1. Note a difference in the statistical noise levels (horizontal dashed line) for (a) and (b), as different integration times have been taken for analysis of these two shots.

The obtained value of χ_e is orders of magnitude higher than the neoclassical value (see Chapter 5 for details). As has been shown in [3], during the ECRH phase a poor average confinement of the outer plasma and good confinement of the core plasma have been observed in the TEXT-U tokamak. Similar to TEXTOR, the heat diffusivity χ_e at TEXT-U during the transition from ECRH to the pure Ohmic heating has been found to be higher than the neoclassical, however, with somewhat lower values of $0.3 - 0.4$ m^2/s than in TEXTOR. However if f the q = 1 surface is indeed a thermal barrier, this lower value could be explained as being the result of averaging over a mixture of a high χ_e inside q = 1 and a low χ_e at the barrier.

Observations reported in [15] show that outside the inversion radius, the spectrum peaks at high frequencies (> 100 kHz), and the probable source of these turbulent fluctuations is attributed to T_e –gradient driven modes. Due to the low sampling rate of the ECE-Imaging diagnostic, this cannot be verified for TEXTOR yet. However, inside the inversion radius, low frequency components (< 30 kHz) are present, and no significant turbulence is detected at higher frequencies, in accordance with the results presented in [13].

Another observation of a high-frequency component (~ 87 kHz) has been done by channels that monitor the plasma outside the q = 2 surface (Fig. 6.9(a)). Interestingly, this component disappears on the channel inside q = 2. Similar observations were made in density fluctuation studies (Fig. 6.9 (b)) by means of an O-mode reflectometer [16]. The

origin of this mode is not known; possible candidate proposed in [16] was a trapped electron mode (TEM) instability; however, an Ion Temperature Gradient (ITG) mode cannot be excluded, too. For the Ohmic shots, the poloidal mode numbers are estimated to be in the range $30 < m < 70$. A good agreement between the turbulence velocity and the poloidal component of the phase velocity has been obtained. Further investigations both with the reflectometer and the ECE correlation technique are needed for a proper interpretation of the origin of this high frequency component in the outer and, possibly, inner plasma layers.

a)

b)
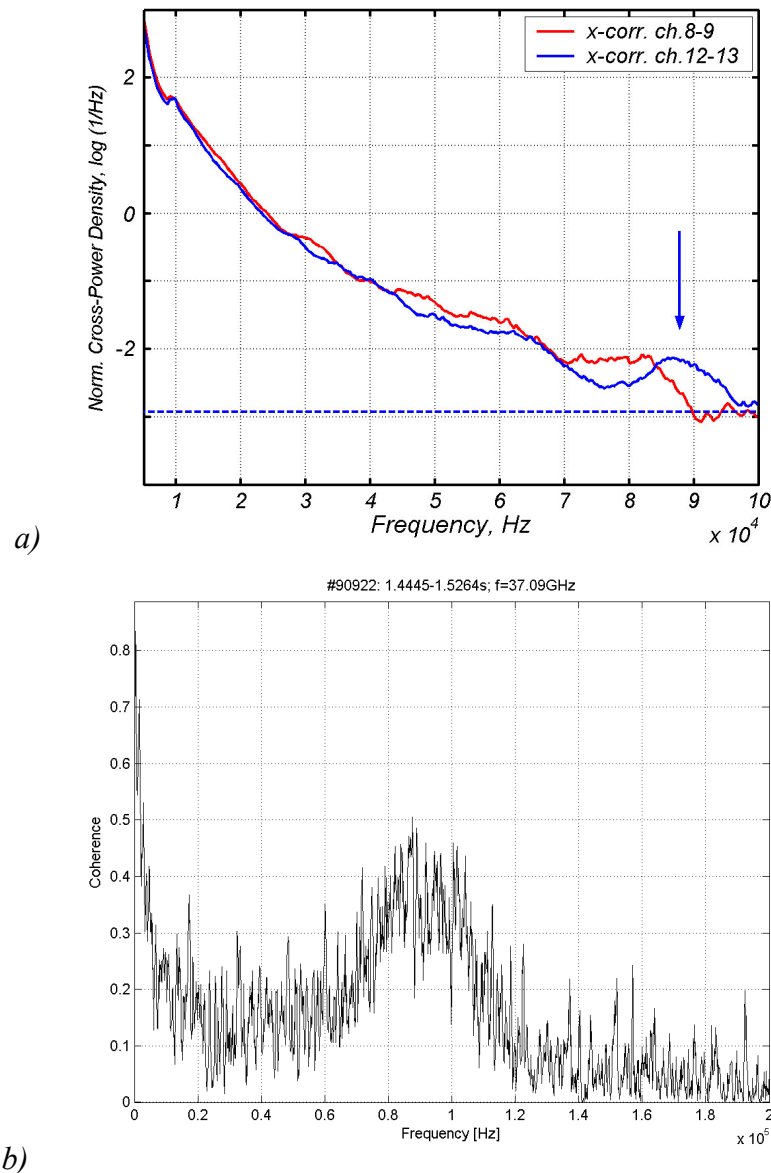
FIG. 6.9. The cross-power spectra between two neighbouring ECE-Imaging channels: inside q = 2 (red, channels 8 - 9) and outside q = 2 (blue, channels 12 – 13). Outside q = 2, a broadband fluctuation is observed at 87 kHz (a), similar to the one observed by the O-mode density reflectometer (b). The horizontal line shows the statistical noise level for this shot.

Acknowledgements

References

[1]   C. Watts, R.F. Gandy, T.D. Rempel, G. Cima, Rev. Sci. Instrum. **66**, 451 (1995).

[2]   H.J. Hartfuss, M. Häse, in Proc. of the 10th Joint Workshop on ECE and ECRH, p. 119 (Ameland, April 6-11, 1997), edited by Tony Donné and Toon Verhoeven (World Scientific, Singapore, 1997).

[3]   G. Cima et al., Plasma Phys. Control. Fusion **40**, 1149 (1998).

[4]   J. Herranz et al., Phys. Rev. Lett., **85**, 4715 (2000).

[5]   E.Westerhof, P.Smeulders, N.J. Lopes Cardozo, Nucl. Fusion **29**, 1056 (1989).

[6]   Y.Nagayama, A.W. Edwards, Rev. Sci. Instr. **63**, 4757 (1992).

[7]   P. Buratti, *"Growth and Rotation of m = 1 Magnetic Islands"*, Presented at the 7th Easter Plasma Meeting, Turin, Italy, April 3-5 (2002).

[8]   B.B. Kadomtsev, Fizika Plasmy **1**, 710 (1975) (in Russian), Sov. J. of Plasma Phys. **1**, 389 (1976).

[9]   Y. Nagayama *et al*., Phys. Rev. Lett. **67**, 3527 (1991).

[10]   S.V. Mirnov *et al*., Nucl. Fusion **40**, 727 (2000).

[11]   J.C. van Gorkom et al., in Proc. of the 28th EPS Conf. on Control. Fusion and Plasma Phys., Funchal, Portugal, Eur. Conf. Abstr. Vol. **25A**, 1401 (2001).

[12]   B.Ph. van Milligen et al., Nucl. Fusion **41**, 447 (2001).

[13]   E. Westerhof et al., submitted to Nucl. Fusion (2003).

[14]   F.C. Schüller, *Private Communications* (2003).

[15]   C. Watts, R.F. Gandy, Phys. Rev. Lett. **75**, 1759 (1995).

[16]   A. Krämer-Flecken et al., in Proc. of the 30th EPS Conf. on Control. Fusion and Plasma Physics, St.-Petersburg, Russia, Eur. Conf. Abstr. Vol. **27A**, P-2.135 (2003).

Chapter 7

Non-thermal electron studies at TEXTOR

Observation of non-thermal, or suprathermal, electrons in magnetically confined plasmas can be used to study the confinement of collisionless electrons and, thus, it can improve our understanding of anomalous transport in tokamak plasmas. Measurements of 30 MeV runaway electrons in TEXTOR, diagnosed by infrared synchrotron radiation, showed an energy dependence of the runaway confinement [1]. From these results, estimates about the scale length of the magnetic turbulence could be made. Lacking in the interpretation was experimental information about the lower energetic part of the fast electron distribution function. For that purpose the new ECE diagnostic has been developed to measure simultaneously the 2nd and 3rd harmonic X-mode emission at four radial locations (see Section 4.1.2).

Suprathermal electrons are electrons with energy [2]:

$$\frac{1}{2}m\mathrm{v}^2 > \frac{1}{2}kT_e \ .$$ (7.1)

This is still a considerable part of the electron distribution function, even if it is purely Maxwellian. Non-thermal electron populations deviate from a Maxwellian distribution with temperature T_e.

There are two important processes that strongly influence fast electrons in a tokamak plasma. The first one is a friction force F_{fr} that decelerates fast electrons with the time:

$$\tau_{dec} = \frac{m\mathrm{v}}{F_{fr}} = \frac{m_e^{\ 2}\mathrm{v}_{th}^3\left(\dfrac{\mathrm{v}}{\mathrm{v}_{th}}\right)^3}{A_e n_e (2 + Z_{eff})} \ ,$$ (7.2)

where A_e is a coefficient which depends on the Coulomb logarithm. The second process is the acceleration by the parallel electric field. The magnetic field causes an asymmetry in the force balance that splits the velocity space in a direction parallel and perpendicular to the toroidal magnetic field. Dreicer has first reported the effects of the balance between acceleration by the electric field along the magnetic field and deceleration by Coulomb collisions [3]. The effective slowing-down time τ_{eff} can be written as:

$$\tau_{eff} = \frac{m\mathrm{v}}{F_{fr} - eE_{\parallel}} \ .$$ (7.3)

When τ_{eff} becomes negative, the friction is not large enough anymore to prevent acceleration of the electrons to relativistic velocities.

In TEXTOR plasmas, besides the combined 2nd-3rd harmonic X-mode ECE radiometer, the presence of fast electrons can be routinely detected by X-mode ECE at the LFS channels of the 11-channel radiometer at frequencies below 107 – 105 GHz. Then,

the emission consists of a grey thermal emission as measured at the cold resonance radius R_{cold} plus a downshifted emission from a radius $R < R_{cold}$ (see Eq. 3.3). However, the observation of the downshifted ECE at the LFS is only possible if the non-thermal emission is very strong and the optical thickness is low enough, so it is not completely absorbed by the thermal electrons. It is necessary to mention that, if there would be a possibility at TEXTOR to measure ECE at the same radial locations but by an antenna at the HFS, the non-thermal radiation travelling towards the HFS would not experience the absorption. Comparison of the spectra as observed both from the LFS and the HFS can be very useful in obtaining information about non-thermal electron populations. This method has been used for the fast electron studies at RTP tokamak [4].

As can be seen from Eq. (3.24), the radiation from the nth harmonic is approximately given by $J_n^2(\omega\beta_\perp/\omega_{ce})$ for perpendicular observation, which is proportional to $\beta_\perp^{2n}$ for $\beta = v/c << 1$ [5]. This means that higher harmonics will be more enhanced by high-energy tails than low harmonics. Moreover, the relativistic downshift can lead to overlap of the different harmonics if the tail of the electron velocity distribution function is relativistic. Thus, the observed ECE intensity (Eq. 3.26) is a complicated integral over ω, $\beta_\parallel$ and $\beta_\perp$.

The energy of non-thermal electrons can be expressed in terms of tail temperatures (energy) $T_\parallel$ and $T_\perp$, instead of velocities $v_\parallel$ and $v_\perp$. As has been reported in [2], a linear scaling of T_e^{rad} with the relative density of the non-thermal electron population and its $T_\perp$ is expected for the optically thin part of the X-mode ECE spectrum. With an increase of $T_\perp$, the second harmonic downshifted radiation should move towards lower frequencies, and on its turn $T_\parallel$ influences the intensity of the downshifted radiation. It should be mentioned that any existing population of hot electrons trapped in banana orbits strongly influences the observed ECE spectra, because these electrons have a high perpendicular energy and, therefore, are strong ECE sources.

Some properties of non-thermal electron populations in TEXTOR plasmas will be discussed in the next Sections.

7.1 Reflection coefficient measurements

For the correct interpretation of the ECE in the presence of non-thermal electrons, it is essential to know the value of the vessel reflection coefficient. A unique feature of the combined 2nd-3rd harmonic radiometer is that direct measurements and calculations of the reflection coefficient are possible. This can be done for Ohmic plasmas with a central density of $1.5 - 2.5\times10^{19}$ m^{-3}, where the plasma is optically thick for the 2nd harmonic ($\tau_2 \sim 10 - 15$) but optically thin for the 3rd harmonic ($\tau_3 \leq 1$, typically $0.4 - 0.8$). It is necessary for ECE channels to be absolutely calibrated. Furthermore, one should take care that no non-thermal populations are present during the measurement, which can be verified by observing ECE emission at a frequency that corresponds to a radial location outside the plasma. The 3rd harmonic signal depends on the electron temperature (measured at the same location by the 2nd harmonic), the electron density (measured by a far-infrared interferometer) and on the unknown reflection coefficient ρ_{refl} (see Eq. 3.25). The measured reflection coefficient is 0.7, similar to a one measured at JET [6].

7.2 Non-thermal electron studies under a density scan and ECRH

The density dependence of non-thermal electron losses is investigated during Ohmic shots [7]. Figure 7.1(a) shows the behaviour of ECE time traces for a typical low-density discharge with a non-thermal electron population. It can be seen that the LFS channel at 105 GHz and the HFS channels with frequencies equal to or higher than 135 GHz saturate after 0.8 s due to the enhanced radiation. The evolution of the line-averaged density is shown in Fig. 7.1(b). For the 2nd harmonic X-mode, the emission measured by the central channels comes from the optically thick plasma (n_{e0} = 1×10^{19} m^{-3}, $\tau_2 \approx$ 4–5 for R = 1.6 – 2.0 m at 0.6 – 1.6 s). For the ECE measured by the outer channels, the plasma is optically "grey" both for the LFS and the HFS. For example, the optical thickness $\tau_2 \approx$ 1.5 at R = 2.08 m (or, alternatively, at 105 GHz in frequency). As has been discussed in Section 4.1.1, channels from 105 to 125 GHz receive ECE from the LFS antenna, whereas channels from 130 to 145 GHz measure radiation from the HFS. Downshifted emission from the non-thermal electrons as observed from the LFS is not completely absorbed by thermal electrons because of the low optical thickness and, therefore, results in enhancement of the radiation temperature as measured by the channel at 105 GHz (see Fig. 7.1 (c)). For the neighbouring channel at 107 GHz, however, this effect is not very pronounced due to the increased density and, thus, increased optical thickness.

Non-thermal ECE that travels towards the HFS is not absorbed, so the resulting radiation temperature as measured by the HFS channels is more strongly influenced by the emission from fast electrons. The downshifted 3rd harmonic ECE may considerably affect HFS spectra too. Figure 7.1(c) gives a comparison of two radiation temperature profiles at a time of ~ 0.6 s for two discharges with similar plasma conditions, but one of them without a significant non-thermal electron population. In the latter case, the line-averaged density is slightly higher than in the discharge with non-thermal electrons. As will be shown later, even a small difference in density can influence the properties of the non-thermal electron population quite significantly. The time of comparison has been chosen such that the channels do not yet show saturation due to the increased radiation. An enhancement of the radiation temperature at the HFS channels (145 and 140 GHz), as well as the relativistic downshift at 105 GHz, can clearly be seen for the plasma with the fast electron population.

Figure 7.2 shows the evolution of both 2nd and 3rd harmonic ECE signals for the same shot as in Fig. 7.1 as measured by the new combined 4-channel 2nd-3rd harmonic radiometer (for technical details, see Section 4.1.2). The 3rd harmonic channels are calibrated at the time interval between 3 and 3.5 s, after an intensive Ne-gas puff. In this phase of the discharge, the line-averaged density rises to 2.7×10^{19} m^{-3}, so the plasma is optically thick for all 2nd harmonic ECE channels, and no fast electrons are present. However, the plasma is still optically thin for the 3rd harmonic ECE, so these channels need to be corrected for the optical thickness and for the wall reflection coefficient in order to obtain proper calibration factors. It is also necessary to mention that the video detectors of the radiometer may have non-linear characteristics at higher input powers. This effect can influence the calibration factors quite significantly, and one needs to be very careful when one tries to interpret the measurements of high radiation temperatures, for example at ~ 1.2 – 1.7 s.

At about 1.6 s, a small density increase from 0.79·10^{19} m^{-3} to 0.85·10^{19} m^{-3} (shown by a vertical arrow in Fig. 7.1(b)) causes a strong decay of the emission in all channels, even in the central 2nd harmonic ones. The 3rd harmonic channels (170 and 175 GHz), as
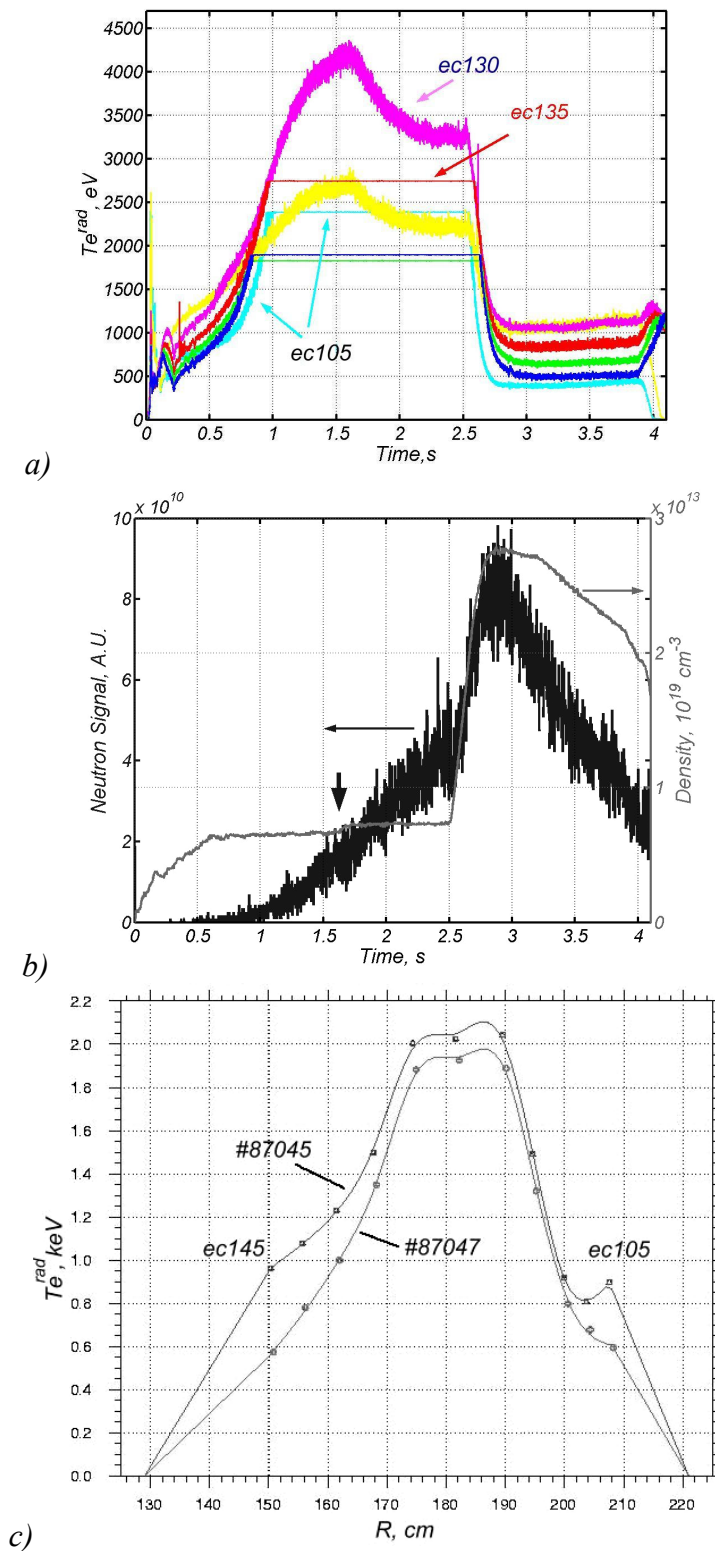
FIG. 7.1. An example of a low-density discharge with a non-thermal electron population: a) 2nd harmonic LFS and HFS ECE time traces from the 11-channel radiometer, b) line averaged density and neutron signal, c) comparison of electron temperature profiles at ~ 0.6 s for the discharge shown in (a) and (b) (#87045) with a similar one (#87047) but without non-thermal electrons in the plasma.

well as some HFS 2nd harmonic channels, fall more rapidly than the 2nd harmonic central and LFS channels (with sufficiently high optical thickness), indicating a very high sensitivity of low energetic non-thermal electrons to slight density changes.
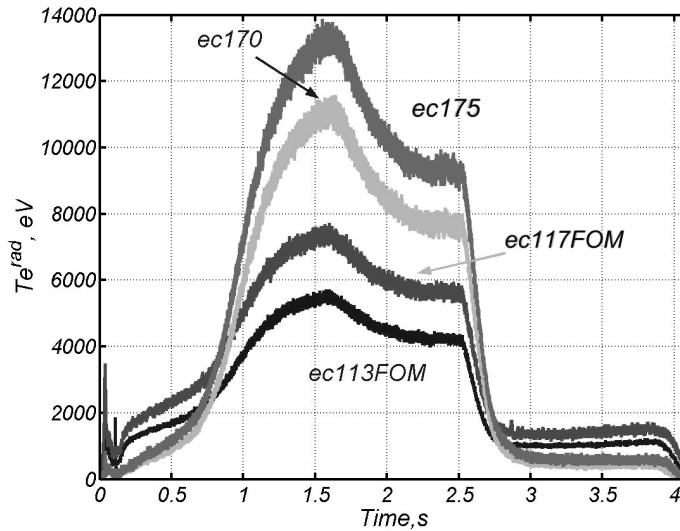
FIG. 7.2. Evolution of the radiation temperature for the same shot as in Fig. 7.1 as measured by the optically thick 2nd (ec113FOM, ec117FOM) and optically thin 3rd (ec170, ec175) harmonics with the 4+4 combined system. At ~ 1.5 s, a slight density increase leads to the decay of the radiation temperature. At 2.5 s, a strong Ne-gas puff leads to a significant density increase. Third harmonic ECE channels were calibrated in the interval between 3 – 3.5 s, with the local optical thickness and the wall reflection coefficient taken into account.

Interestingly, the highly energetic runaways with energy up to 20 MeV are not directly responding to such small density changes. They are only affected by a substantial density ramp up. This is evidenced by measurements of the neutron signal (see Fig. 7.1(b)). Neutrons are created when runaway electrons with an energy of > 10 MeV hit the limiter. In other words, the neutron signal measures the loss rate of highly energetic runaways. Soon after a strong Ne-gas puff at 2.5 s the medium energetic electrons ($10 < E/kT < 100$) responsible for the high ECE-values are lost while highly energetic runaways ($100 < E/kT < 1000$) are still existing more than 0.5 s after the gas puff has been started.

Figure 7.3 shows a significant drop in radiation temperature during ECRH (frequency 110 GHz, duration 80 ms, injected power 300 kW) at 1.5 s, as observed from the LFS. The decay time during ECRH and the rise time of the radiation temperature after switching off ECRH are again different for the 2nd and 3rd harmonic ECE, with the re-absorption at the thermal layer taken into account. This might indicate a lower birth-rate of non-thermal electrons during ECRH due to a drop in the parallel electric field, which is observed as a decrease in the loop voltage. A further mechanism that can possibly play a role is a degradation of the confinement of non-thermal electrons as a result of enhanced magnetic turbulence in the presence of ECRH.

Another example of the behaviour of non-thermal electrons under modulated ECRH is shown in Fig. 7.4. Spikes on the 105 GHz LFS ECE channel are associated with the sawtooth activity and probably they are caused by downshifted radiation from non-

thermal electrons with perpendicular energy up to a few tens of keV. During the time interval, plasma is optically "grey" at this radius with $\tau_2 \approx 1.8$. For the neighbouring channel at 107 GHz, however, the optical thickness value amounts already to ~ 3.2, due to the steep density gradient. This can explain the fact that the non-thermal radiation does not appear first on channels closer to the heating frequency of 110 GHz. At the same time, the electron density drops in this phase of the discharge. Interestingly, the intensity of the downshifted emission (spikes) in the beginning of the inverted sawteeth drops as the ECRH phase continues. It is possible that the energy of these non-thermal electrons grows, so their radiation shifts further towards lower frequencies.
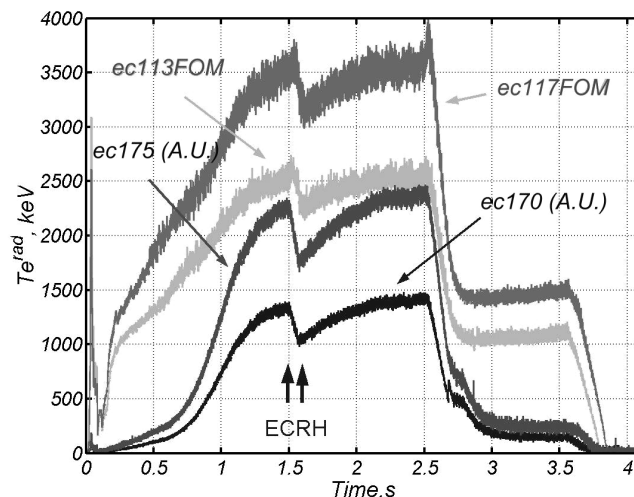
FIG. 7.3. During and after ECRH, a difference in the duration of decay and rise time of the radiation temperature is observed for 2nd and 3rd harmonic ECE. ECE signal numbers are the same as in Fig. 7.2. Third harmonic ECE signals are given in arbitrary units. Two vertical arrows show an 80 ms ECRH phase. Magnetic field B$_t$ = 2.25 T.

7.3 ECE spectra simulations with the NOTEC code and conclusions

The ECE spectra in presence of non-thermal electrons have been calculated with the help of the so-called NOTEC code. NOTEC is a 3-D code to calculate ECE spectra, taking into account the antenna pattern, refraction, the vessel reflection coefficient, and non-thermal populations [8]. Non-thermal features of ECE spectra can be modelled in NOTEC with drifting Maxwellians, temperature anisotropy, loss- and anti-loss cones. To calculate spectra for the known antenna pattern and vessel parameters, several rays, describing the characteristics of this pattern, are launched into the plasma. For the ray tracing part, the cold plasma approximation is being used (see Section 3.1). This code has been fully adapted for TEXTOR plasma conditions.

The electron temperature field (profile) in NOTEC is described as follows:

$$T_e = (T_e^{\max} - T_e^{\min}) \left[1 - \left(\frac{\rho}{a} \right)^{p1} \right]^{p2} + T_e^{\min}, \tag{7.4}$$
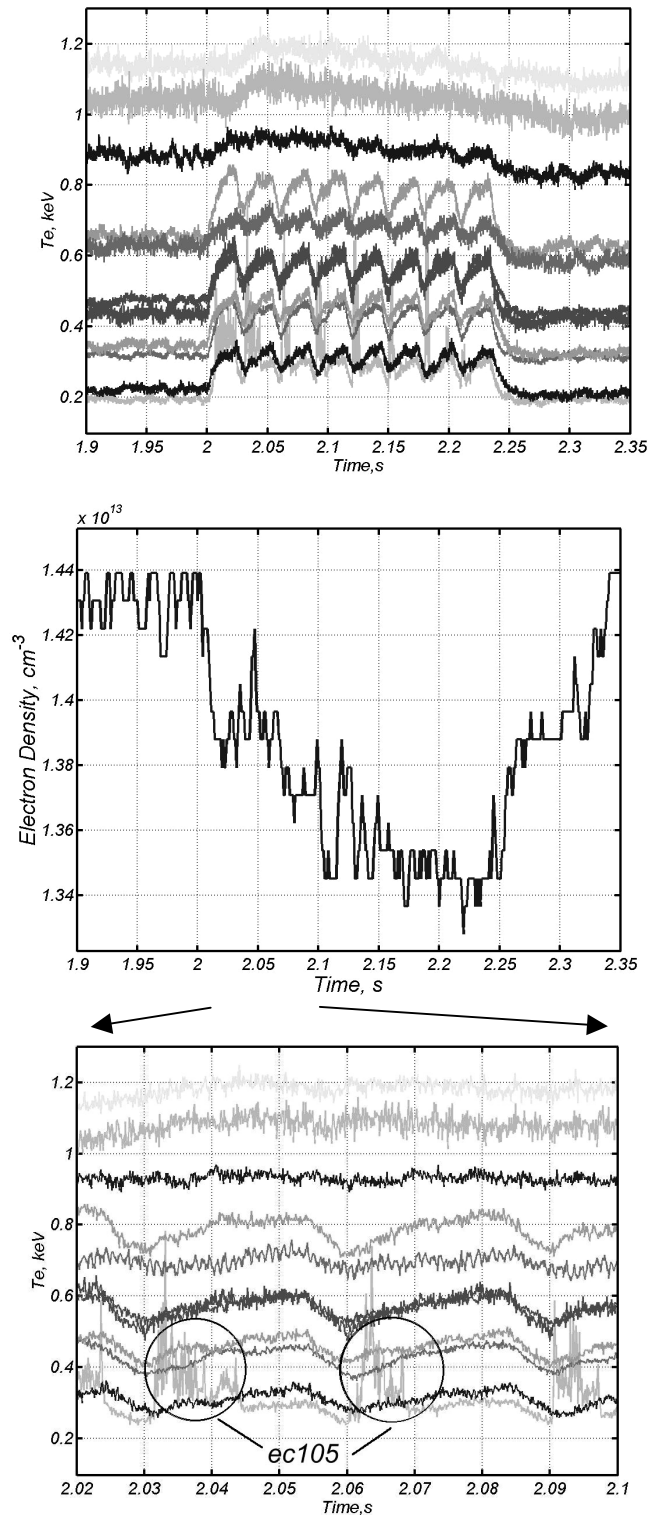
FIG. 7.4. ECE time traces show an enhancement of the electron temperature (upper plot), and the line-averaged electron density drops by 6% (middle plot) during modulated ECRH between 2 – 2.25 s. ECE time traces at the LFS (bottom plot) show spikes on top of the 105 GHz channel, due to downshifted radiation of non-thermal electrons. The magnetic field is about 2.24 T.

where T_e^{max} and T_e^{min} are electron temperatures in the plasma core and at the edge, respectively. A similar expression describes the electron density profile. Since temperature and density profiles can vary from shot to shot, depending on particular plasma properties, parameters *p1* and *p2* may change. For the same shot as in Figs 7.1 – 7.2, the assumptions about the electron temperature profile shape have been made for the optically thick 2nd harmonic ECE spectra after the gas puff at 2.5 s. The best fit is obtained for T_e^{max} = 1400 eV, T_e^{min} = 50 eV, *p1_temp* = 2 and *p2_temp* = 3.5 (see Fig. 7.5). For the electron density, n_e^{max} = 4.25·10^{19} m^{-3}, n_e^{min} = 2·10^{17} m^{-3}, *p1_dens* = 2, *p2_dens* = 1.2 are estimated. Simulations have been performed for both LFS and HFS channels. Non-thermal electron populations have not been included in the first calculations.
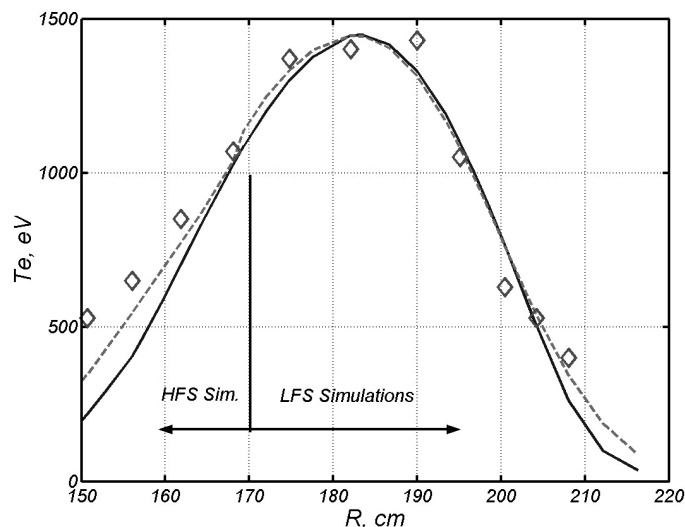
FIG. 7.5. ECE temperature profile simulations for the same shot as in Figs. 7.1 – 7.2 for the time after 2.5 s. The solid line is a spectrum calculated without the reflection coefficient taken into account, the dotted line represents the spectrum calculated with the reflection coefficient of 0.67. Diamonds are the experimental points from the 11-channel radiometer.

For the same discharge, the ECE spectra have then been calculated for the phase with the non-thermal electron population and then compared with the experiment for the time at about 0.6 s. In these simulations, the existence in the plasma centre of two non-thermal populations with parallel energies of 10 keV, and perpendicular energies of 14 and 24 keV, respectively, and densities of 1.1% and 1.5% of the total electron density are assumed. The results are shown in Fig. 7.6. The relativistic downshift for the 2nd harmonic X-mode is clearly seen at the frequencies below 106 GHz, as well as influence of fast electron populations on the HFS spectra between 130 – 145 GHz and to the intensity of the 3rd harmonic ECE above 160 GHz. The maximum radiation temperature for the 2nd harmonic T_e^{max} of about 2.2 keV (LFS measurement) and the maximum central electron density of 1.05·10^{19} m^{-3} are taken from the experiment.

It is necessary to realise, however, that there are many possible solutions that would give a similar satisfactory result. In a low-density plasma, trapped non-thermal electron populations with different energies and densities can exist. With the combined 2nd-3rd harmonic ECE radiometer, only qualitative information about non-thermal electrons can be obtained. To get the full information on different fast electron populations that exist in plasma, the help from other diagnostics, such as oblique and/or combined LFS/HFS ECE, soft and hard X-ray diagnostics would be essential. For the future

TEXTOR campaigns, some new X-ray diagnostics for non-thermal electron studies will become available.
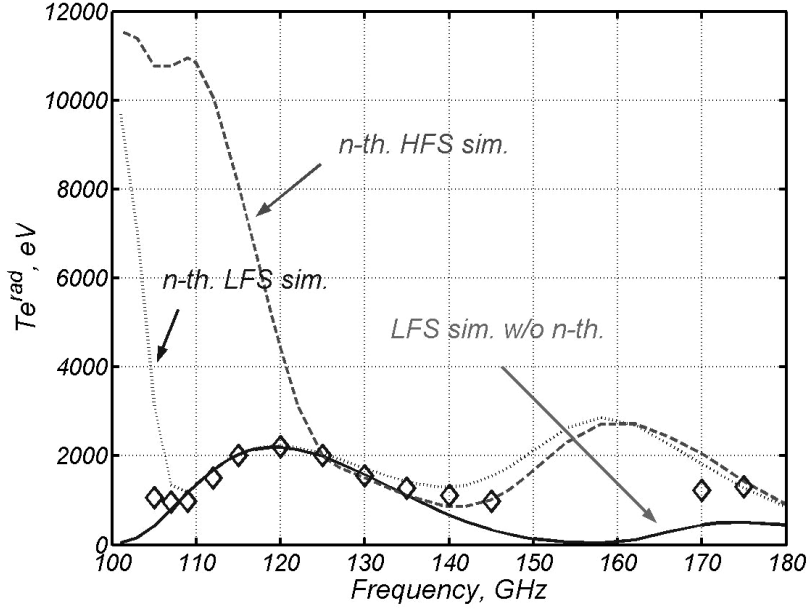

FIG. 7.6. Simulations for the same shot as in Figs. 7.1 – 7.2 but in the phase with non-thermal electrons: solid line – simulation performed for the LFS observation of the plasma without any non-thermal electron populations, dashed line – HFS simulations for the plasma with two non-thermal electron populations ($n_{n\text{-}th}^1$ = 1.1%, $n_{n\text{-}th}^2$ = 1.5%, $T_\parallel^{1,2}$ =10keV , $T_\perp^1$ =14keV , $T_\perp^2$ =24keV), dotted line - LFS simulations for the plasma with two non-thermal electron populations. Diamonds are the experimental points. Note the relativistic downshift for the 2nd harmonic at the frequencies below 106 GHz, and the enhancement of the spectra for the frequencies above 130 GHz due to the relativistic downshift of the 3rd harmonic ECE. For the calculations, the actual LFS/HFS antenna pattern parameters were used.

Acknowledgement

References

[1]   I. Entrop *et al.*, Phys. Rev. Lett. **84**, 3606 (2000).

[2]   B.C. Schokker, Thesis Technische Universiteit Eindhoven (1996).

[3]   H. Dreicer, Phys. Rev. **115**, 238 (1959).

[4]   J.F.M. van Gelder *et al*., Plasma Phys. Control. Fusion **40**, 1185 (1998).

[5]   I.H. Hutchinson, *Principles of Plasma Diagnostics*, Cambridge University Press (1994).

[6]   A. Costley and D. Bartlett, *Private Communications* (2003); G Ramponi *et al*., "*Simulation of JET ECE spectra along multiple chords and comparison with experiment*", Proc. of the Fifth International Workshop on ECE and ECRH, San Diego, USA (1985).

[7]   V.S. Udintsev *et al*., in Proc. of the 27th EPS Conf. on Control. Fusion and Plasma Phys., Budapest, Hungary, Eur. Conf. Abstr. Vol. **24**B, 952 (2000).

[8]   R.M.J. Sillen, Rijnhuizen Report 86-165 (1986).

Chapter 8

Conclusion and future prospects

To study plasma properties in the presence of large and small MHD modes, new high-resolution ECE diagnostics have been installed at TEXTOR, and some of the already existing systems have been upgraded. The new diagnostics include a fast (sampling rate up to 2 MHz) 16-channel heterodyne radiometer to study small-scale structures and fast fluctuations in the electron temperature profile throughout the plasma, and a combined 2nd -3rd harmonic radiometer to diagnose non-thermal electron populations. Moreover, use is being made of a 16-channel ECE imaging system, which provides the emission distribution along a vertical chord. Together with other TEXTOR diagnostics, these are powerful tools to study MHD phenomena and related transport.

Two models for the plasma transport properties inside large MHD islands have been found to give estimations for the heat diffusivities, which are much lower than the global plasma heat diffusivity, which is agreement with previous measurements in different tokamaks [1, 2]. The 3D-reconstruction of large modes in TEXTOR with the help of all available ECE diagnostics allows modelling the island as a structure with closed flux surfaces. The main plasma heat flux flows through the X-point area probably along stochastic magnetic field lines. The confinement is improved within the magnetic island, compared to the background plasma. This is confirmed by a temperature profile flattening and sometimes even a secondary peaking inside the island, compared to the X-point. The same observations have been made in the electron density profiles by a pulsed radar reflectometer. However, in order to have more accurate measurements, one would prefer the $m/n = 2/1$ modes to be stationary for a longer time interval than described in this thesis. With the present TEXTOR plasma position control and heating systems, it is very difficult to achieve this. In the near future, many TEXTOR systems will be significantly upgraded. A new ECRH gyrotron will operate at 140 GHz with a power of 800 kW and pulse duration up to 10 s. This will allow to heat the island more effectively than with the 110 GHz gyrotron, to study its transport properties and to make a comparison with NBI or Ohmic shots. New interesting physics at TEXTOR is expected to come from the so-called Dynamic Ergodic Divertor (DED) [3]. The DED allows for an enhanced particle removal by a pump limiter, it may unlock modes, and impose a different rotation in the plasma edge and thereby improve the confinement. It consists of a quadruple set of four helical conductors, installed on the inboard side of the TEXTOR vessel and aligned parallel to the magnetic field lines at the nearby $q = 3$ surface. With the use of the DED, it will be even possible to create a magnetic island with a pre-programmed size and position. This will make it easier to study its transport properties with precision.

Making use of the mode rotation, assumed to be a rigid rotor, it has been possible to obtain information on the topology of the $m = 1$ precursor mode leading to sawtooth collapses. It becomes clear that this precursor cannot be described by an $m = 1$ cold tearing-mode island but by a hot crescent wrapped around a cold high-density bubble. In the future multi-chord ECE-imaging will allow this mode reconstruction without the assumption of the rotation to be rigid.

The mode rotation studies with the ECE-Imaging diagnostic have shown that the purely poloidal component of plasma rotation due to diamagnetism can be significant in some Ohmic and NBI-heated discharges at TEXTOR, especially when large modes are

present with low toroidal ion velocity. It is confirmed that if the $m = 1, 2$ and 3 modes with $n = 1$ number are coupled, they have their X or O-points in phase at the LFS. The large islands are almost always asymmetric at the LFS and symmetric at the HFS, although, the total island width is the same in both cases.

Both the ECE and the pulsed radar reflectometer diagnostics have confirmed the evidence of a small-scale mode with $1 < m/n < 2$. The exact m and n numbers of this mode are not yet known and cannot be deducted from the ECE and the pulsed radar reflectometer measurements only. The mechanism that forces this mode to uncouple from the strongly coupled 2/1 and 1/1 modes is not understood either unless a strong pressure gradient forces a large poloidal rotation and breaks the magnetic topology at some time. For this type of measurements, fast magnetic diagnostics (for example, Mirnov coils), as well as information on rotation on a faster time scale than possible with the present CXRS diagnostic, are essential. To reveal whether the effects may be attributed to a possible modification of the q-profile in this region, the newly installed Motional Stark Effect (MSE) diagnostic can be very helpful.

The rotation of MHD modes is closely connected to the problem of the avoidance and mitigation of disruptions. The injection of co- and counter neutral beams to avoid disruptions was successfully tested at TEXTOR. If $m/n = 2/1$ mode activity is detected, the counter-NBI is switched on by the trigger, and a minor disruption occurs. It cleans the plasma efficiently, and the sawtooth activity appears soon after, so the discharge can be terminated successfully. If it is not possible to avoid the disruptions in that way, it can be mitigated by an intensive helium puff that suppresses runaway electrons.

Qualitative studies of non-thermal electrons at different heating regimes (ECRH and Ohmic) at TEXTOR were done with the help of the combined 2nd-3rd harmonic X-mode ECE radiometer. It has been found that the lower energetic non-thermal electrons are directly responsive to small density changes, in contrast to the highly energetic runaways with energy up to 20 MeV. Those are only affected by a substantial density ramp up. The same is applicable to the response of the mildly non-thermal electrons to ECRH; even though the ECRH power from 110 GHz gyrotron injected into the plasma was not high. A satisfactory agreement with the NOTEC-simulated ECE spectra has been obtained. However, there are many possible solutions that would give rather similar results, especially if several trapped non-thermal electron populations with different energies and densities co-exist in the plasma. In order to have the full information on the electron populations in the plasma, one needs as much as possible information from other, not yet applied, diagnostics, such as oblique and/or combined LFS/HFS ECE, soft and hard X-ray detectors.

The broadband temperature and density fluctuations and their influence to the plasma transport properties are a relatively new subject of study at TEXTOR. Even though a dedicated ECE cross-correlation technique was not yet available at TEXTOR, first evidence for a difference between the normalized power spectra outside and inside $q = 1$ surface has been observed from a cross-correlation analysis between various ECE-Imaging channels or from the autocorrelation function. From the measurements one can conclude that the turbulent structures inside the $q = 1$ surface are separated from the turbulence outside the $q = 1$ surface. This fits nicely with the observation that $q = 1$ surface acts as a barrier for the thermal transport. Correlation length and time measured inside q=1 are in agreement with the observed turbulent heat-diffusivity.

High frequency broadband turbulence has been studied also near the $q = 2$ magnetic islands. It appears that the turbulence characteristics are strongly modulated by the macroscopic islands. At the island O-point the correlation length and time are much

larger than at the X-point. This modulation of characteristics can be explained either by the difference in turbulence driving gradients between X- and O-point or in case of stochastic magnetic fields by the necessity that the stochastic areas have to rotate with the X-point.

A high-frequency component outside the $q = 2$ surface has been observed too, which is in agreement with the measurements obtained by an O-mode density reflectometer. The possible origin of this mode was suggested to be either ITG or trapped electron mode, however, the latter is very unlikely, because the fraction of trapped electrons is very small outside $q = 2$ surface at TEXTOR. Another observation has been made in Ohmic and ECR-heated discharges and revealed a difference in the spectral slope between the two heating methods, similar to what has been observed at the TJ-II stellarator and some other devices not only with ECE but also with a Langmuir probes at the edge. This difference can be caused by the fact that a small fluctuation in temperature could be non-linearly amplified by the applied heating method, leading to a modification of the temperature profiles and power spectra. However, knowledge of the plasma rotation and, therefore, the correction for the Doppler shift, is essential for this kind of studies.

References

[1]   B.Ph. van Milligen *et al*., Nucl. Fusion **33**, 1119 (1993).
[2]   F. Salzedas *et al*., Phys. Rev. Lett. **88**, 075002 (2002).
[3]   K.H. Finken, Transactions of Fusion Technology **37**, 421 (2000).

Appendix A

Values of some physical constants

Electron charge, *e*:	1.602×10^{-19} C
Electron mass, m_e :	0.911×10^{-30} kg
Ratio e/m_e:	1.759×10^{11} C/kg
Proton mass, m_p :	1.673×10^{-27} kg
Neutron mass, m_n :	1.675×10^{-27} kg
Speed of light, *c*:	2.998×10^{8} m/s
Permeability of vacuum, μ_0 :	$4\pi \times 10^{-7}$ H/m
Permittivity of vacuum, $\varepsilon_0 = 1/(\mu_0 c^2)$:	8.854×10^{-12} F/m
Boltzmann constant, *k*:	1.381×10^{-23} J/K

Conversion from Kelvin to eV

1 electron volt (eV) = 1 Kelvin (K) $\times$ 1.1604×10^{4}

Appendix B

Conversion from CGS to SI units

Although SI is the widely accepted system nowadays, some physicists continue to use the old Gaussian, or CGS, units. The table below helps to convert units expressed in CGS to the ones in SI:

Unit (SI) = Unit (CGS) × Conversion Factor

Quantities	CGS (name)	Conversion Factor	SI (name)
Distance	cm	$=10^{-2}$	m
Mass	g	$=10^{-3}$	kg
Time	sec	$=$	sec
Force	dyne	$=10^{-5}$	Newton
Energy	erg	$=10^{-7}$	Joule
Charge	esu	$=3.333 \times 10^{-10}$	Coulomb
Electrical Potential	statvolt	$=299.8$	Volt
Magnetic Field	Gauss	$=10^{-4}$	Tesla
$1\ eV = 1.602 \cdot 10^{-12}\ erg$			

Summary

Controlled thermonuclear fusion has the potential to fulfil the demand of mankind to have an inexhaustible source of energy that does not cause any serious environmental pollution. If the temperature of the thermonuclear plasma is high enough, light nuclei may fuse into heavier ones. The energy released in the process of fusion may be used to produce electricity.

The main research goal is to make the fusion reaction self sustained. The temperature and pressure of the thermonuclear plasma is high: hundreds of million degrees and tens of atmospheres. In stars like our sun the plasma can be confined by gravity. On earth this is only possible by means of strong magnetic fields. The most efficient magnetic configuration so far is the tokamak. However, under the relevant conditions for fusion, plasma instabilities may lead to a confinement degradation and enhancement of the transport of heat and particles. In some cases, the plasma can even be completely lost in the event of a so-called disruption. This causes large heat loads and eventually damage to the tokamak wall.

Very often, so-called tearing modes or magnetic islands precede disruptions. These modes tear the equilibrium magnetic topology and, thereby enhance the transport. Magnetic islands are formed on magnetic flux-surfaces on which, by geometrical resonance, field lines close on themselves since the local helicity of the field lines as given by the local winding number q is such that q is equal to the ratio of simple integer values. The islands on these surfaces can be described by their toroidal and poloidal mode numbers, m and n, with the ratio between m and n equal to the local q. In TEXTOR, large perturbations were observed near the $q = 1$, $q = 2$ and $q = 3$ flux-surfaces by means of various microwave (Electron Cyclotron Emission, Pulsed Radar Reflectometer, HCN-interferometer), Thomson scattering of laser light, and various forms of spectroscopy ranging in wavelength between visible light and soft x-rays. Some of these diagnostics were especially designed to study the plasma transport properties in the presence of large Magnetohydrodynamic perturbations.

Two different models to describe the effect of plasma transport properties inside large magnetic islands give similar estimations of the heat diffusivity. The diffusivity inside the island is much lower than the global plasma heat diffusivity. The results are in good agreement with the measurements performed in other tokamaks. The 2D-reconstruction of large modes in TEXTOR has been obtained with the help of ECE diagnostics. It allows modelling the island as a structure with closed flux surfaces. The areas around the tips of neighbouring islands of the same chain are called X-points. The main plasma heat flux from the centre of the plasma to the outside appears to flow around the islands through the X-point area probably along stochastic magnetic field lines. The perpendicular transport crossing the boundary of the island (O-point) is very much reduced because of the low diffusivity. This is evidenced by a temperature profile flattening and sometimes even a secondary peaking inside the island, compared to the X-point. A significant density peaking inside the island has also been observed by means of Thomson scattering and pulsed radar reflectometry.

Studies of a large $m = 1$ precursor to a sawtooth collapse have shown that the perturbation has the form of a hot crescent wrapped around a cold but dense bubble. It appears that the standard tearing mode theory is not applicable here.

The broadband temperature and density fluctuations and their influence on the plasma transport properties are a relatively new subject of study at TEXTOR. From the measurements one can conclude that the turbulent structures inside the $q = 1$ surface are separated from those occurring outside the $q = 1$ surface. This confirms the earlier observation that the $q = 1$ surface acts as a barrier for thermal transport.

Mode rotation studies with the ECE-Imaging diagnostic have shown the importance of the poloidal component of plasma rotation in some Ohmic and NBI-heated discharges at TEXTOR. If the modes with $m = 1, 2, 3$ and $n = 1$ number are coupled, they have their X-points ($m = 2$ and 3) and the hot crescent ($m = 1$) in phase at the LFS. The large islands are almost always radially asymmetric at the LFS but symmetric at the HFS. However, the total island width is the practically same at both locations.

Beside the large modes described above, there are small-scale modes with higher m and n numbers that exist in the plasma. One of these modes has been observed both by the ECE and the pulsed radar reflectometer diagnostics with: $1 < m/n < 2$. It is well possible that the magnetic topology breaks up further when the low m and n islands become too large and that this forces the creation of a chain of islands with higher m and n numbers.

The turbulence characteristics appear to be strongly modulated if large $m/n = 2/1$ islands are present. Near the island O-point both the correlation length and time are much larger than near the X-point. This can either be explained by the modulation of the turbulence driving gradients due to the large islands or by areas of stochastic magnetic field that have to rotate with the X-point of those islands.

The rotation of MHD modes is closely connected to the problem of the avoidance and mitigation of disruptions. The injection of co- and counter-neutral beams to avoid disruptions was successfully tested at TEXTOR. If $m/n = 2/1$ mode activity is detected to be above a set critical value, the counter-NBI is switched on, and a minor disruption occurs. It cleans the plasma efficiently, and a 'healthy' sawtooth activity appears soon after, so the beam can be switched off or the discharge can be terminated softly. If it is not possible to avoid the disruptions in that way, they can be mitigated by an intensive Helium puff that suppresses runaway electrons.

During the disruption, a huge amount of runaway electrons can be created. However, there was a lack of experimental observation of a mildly energetic runaways, or non-thermal electrons. Qualitative studies of non-thermal electrons at different heating regimes at TEXTOR were done by means of a combined $2^{nd} - 3^{rd}$ harmonic ECE radiometer. It has been found that, unlike the lower energetic non-thermal electrons, the highly energetic runaways with energy up to 20 MeV are not directly responsive to small density changes. They are only affected by a substantial density ramp up. The same is applicable to the response of the fast electrons to ECRH. A satisfactory agreement with NOTEC-simulated ECE spectra has been obtained.

Samenvatting

Gecontroleerde thermonucleaire fusie heeft het potentieel om de vraag van de mensheid naar een onuitputtelijke energiebron zonder ernstige milieuverontreiniging te beantwoorden. Als de temperatuur van het fusieplasma hoog genoeg is, kunnen de lichte kernen samengevoegd worden tot zwaardere kernen. De energie die tijdens dit fusieproces vrijkomt kan worden gebruikt om elektriciteit op te wekken.

Het belangrijkste onderzoeksdoel is de fusiereactie zelfonderhoudend te maken. De temperatuur en druk van het thermonucleaire plasma moeten hiervoor zeer hoog zijn: enige honderden miljoenen graden met een druk van enige tientallen atmosfeer. Op aarde kan zo'n plasma niet met zwaartekracht bij elkaar gehouden worden zoals in sterren en onze zon. Het plasma kan slechts door middel van sterke magnetische velden worden opgesloten. De meest efficiënte magnetische configuratie tot dusver is de, in Rusland bedachte maar nu wereldwijd onderzochte, "tokamak". Hiermee zijn bijvoorbeeld in het Europese JET experiment 'break-even' condities behaald met een opwekking van een tiental MW thermisch vermogen. Nochtans, in de relevante omstandigheden voor fusie, kan plasma-instabiliteit tot een beperkende plasmadegradatie en tot een verhoging van het transport van hitte en deeltjes leiden. In sommige gevallen kan het plasma zelfs volledig door een disruptieve verstoring worden vernietigd. Dit veroorzaakt grote warmtebelastingen van de reactorwand en uiteindelijk schade.

Zeer vaak zijn de magneto-hydrodynamische (MHD) verstoringen zogenaamde 'tearing modes' of magnetische eilanden. Deze verscheuren lokaal de magnetische topologie en verhogen daardoor het warmtetransport. De magnetische eilanden ontstaan op magnetische fluxoppervlakken waar door geometrische resonanties magneetvelden op zichzelf aansluiten. De geometrische mode getallen m en n van deze eilanden hebben dan een verhouding die overeenstemt met het zogenaamde getal q die de lokale heliciteit van het magneetveld beschrijft. In TEXTOR, worden de grote verstoringen waargenomen rond de $q = 1$, $q = 2$ en $q = 3$ fluxoppervlakken door middel van diverse microgolf diagnostieken (de emissiemetingen van elektronen cyclotron golven (ECE), de gepulste radar reflectometer, de HCN-interferometer), de Thomsonverstrooiing van laserlicht, de spectroscopie in een zeer breed golflengtegebied van zichtbaar licht tot zachte röntgenstraling. Sommige van deze diagnostieken zijn vooral ontworpen om de eigenschappen van het plasmatransport in aanwezigheid van grote magnetische verstoringen te bestuderen.

Het blijkt uit de resultaten met twee verschillende methoden dat het warmtetransport binnen een magnetisch eiland veel lager is dan in het omringende plasma. De resultaten zijn in goede overeenkomst met de metingen die bij andere tokamaks worden uitgevoerd. De 2D-topologie van grote eilanden in TEXTOR is verkregen met behulp van ECE metingen. Het beschrijft het eiland als een structuur met gesloten stroom- en fluxoppervlakken. De belangrijkste warmtestroom vanuit het centrum van het plasma naar de buitenwereld vloeit waarschijnlijk door de zogenaamde X-punt gebieden. Dit zijn gebieden tussen de punten van naburige eilanden waar de magnetisch veldlijnen stochastisch verlopen. Het transport loodrecht op het eiland en binnen het eiland is zeer klein, zodat zelfs lokale maxima in temperatuur en vooral dichtheid binnen eilanden gevormd worden. Dit is mede waargenomen door middel van Thomsonverstrooiing en gepulste radar reflectometrie.

De studies van de $m = 1/n = 1$ voorloper van zaagtand-collapsen hebben aangetoond dat deze verstoring als een hete sikkelvormige verstoring beschreven kan worden die een

koud en dicht cirkelvormig gebied grotendeels omringt. Het blijkt dat de standaard 'tearing mode' theorie niet op dit type verstoring toepasselijk is.

De breedband temperatuurs- en dichtheidsfluctuaties en hun invloed op de transporteigenschappen van het plasma zijn een nieuw onderwerp van studie aan TEXTOR. Uit de correlatiemetingen van de turbulentie kan men concluderen dat de turbulente structuren binnen het $q = 1$ oppervlak gescheiden zijn van die aan de buitenzijde van het $q = 1$ oppervlak. Dit bevestigt de oudere observatie dat het $q = 1$ oppervlakte een barrière voor thermisch transport vormt.

De meting van de omwentelingsfrequentie van de eilanden met ECE-Imaging hebben het belang van de poloidale component van deze rotatie in sommige TEXTOR-plasmas aangetoond. De rotatie van eilanden, mits groot genoeg, met $m = 1, 2, 3$ en $n = 1$, kan gekoppeld zijn op een unieke wijze die een vaste faserelatie geeft tussen X- en O-punten van de eilandreeksen op verschillende q-oppervlakken De grote eilanden zijn bijna altijd asymmetrisch als functie van de poloidale hoek..

Naast de grote hierboven beschreven verstoringen zijn er ook kleinschalige eilanden met hogere m en n getallen. Eén van deze eilandreeksen is waargenomen zowel door ECE als de gepulste radar reflectometer met: $1 < m/n < 2$. Het is goed mogelijk dat indien de magnetische topologie verbroken wordt door grote eilanden met lage m en n getallen, dit tot de formatie leidt van parasitaire kleine eilanden met hogere m en n aantallen op andere q-oppervlakken.

De breedband turbulentie schijnt sterk te worden gemoduleerd als er grote $m/n = 2/1$ eilanden aanwezig zijn. Dichtbij het O-punt van het eiland zijn zowel de correlatielengte als -tijd veel groter dan dichtbij het X-punt. Dit kan aan de modulatie van de turbulentie-drijvende gradiënten toe te schrijven zijn of doordat er gebieden van stochastisch magnetisch velden zijn die met de X-punten mee roteren.

De rotatie van de MHD-verstoringen is nauw verbonden met het probleem van het vermijden of verminderen van de verstoringen. De injectie van bundels hete neutralen (NBI) tegen of juist met de plasmastroom mee kunnen MHD-verstoringen verminderen of juist bevorderen. Dit is met succes getest bij TEXTOR. Als een $m/n = 2/1$ mode activiteit boven een kritische waarde uitstijgt, wordt tegen-NBI ingeschakeld. Een niet al te ernstige gedeeltelijke disruptie maakt het plasma efficiënt schoon en de 'gezonde' zaagtand-activiteit verschijnt spoedig daarna, zodat de NBI kan worden geëindigd. Als het niet mogelijk is om de verstoringen die tot een totale disruptie leiden op die manier te vermijden, kunnen door een intensieve injectie van heliumgas de schadelijke effecten op de reactorwand worden verlicht.

Tijdens de disruptie, kan een reusachtige hoeveelheid relativistische (runaway-) elektronen worden opgewekt die extra schade toebrengen. Tot nu toe was het moeilijk het gedrag van suprathermische elektronen voor ze tot relativistische energie worden versneld te observeren. Kwalitatieve studies van suprathermische elektronen zijn gedaan bij verschillende regimes van TEXTOR-plasmas door middel van een gecombineerde 2^e - 3^e harmonische radiometer van ECE. Het blijkt dat, in tegenstelling tot de lagere energetische suprathermische elektronen, de hoogenergetische runaway elektronen met een energie tot 20 MeV niet direct gevoelig zijn voor kleine veranderingen in de dichtheid. Zij worden slechts beïnvloed door een forse dichtheidstoename. Hetzelfde geldt voor de reactie van de mild-suprathermische elektronen op verhitting met Elektron Cyclotron Resonante microgolfstraling (ECRH). Een bevredigende overeenkomst met de door de NOTEC-code gesimuleerde spectra van 2^e en 3^e harmonische ECE is verkregen.

Acknowledgements

During all this time in Jülich, I was not confined in Germany or Holland only. I have made an incredible amount of friends all over the World. I just want to mention a few of them: Theo and Mary Egbers, Gesa Koehn-Gould, Phil Stamp.

And, of course, GREAT THANKS to my wife Natasha. We have married in Jülich too, and this, together with the present thesis, are the main events that have happened in my life within the last years. Without help from Natasha, I would never have completed this thesis.

In the end, I would like to wish good luck to all those who will work at Rijnhuizen and Jülich in coming years, especially to Ivo, Maarten, Alexey, Kasia, Sanjeev and other PhD or Diploma students.

Curriculum Vitae

I was born on March 17, 1975 in Moscow, USSR/Russia. In 1992, I have finished the Phys.-Mathem. Lyceum 1502. In 1998, I have got the Master of Science Degree with Distinction at the Moscow Power Engineering Institute (Technical University) on specialty "Plasma Physics and Controlled Thermonuclear Fusion Research". My Diploma work, "Microwave Discharge in Multiple Magnetic Traps PN-1 and PN-3, models of Plasma Neutralizer for ITER Tokamak Injector", has been performed at the Nuclear Fusion Institute of the Russian Research Centre "Kurchatov Institute" under the supervision of Dr. Alexander Skovoroda and Valery Zhiltsov. After a short employment at the Russian Research Centre "Kurchatov Institute", I have started my PhD-work at the FOM-Insituut voor Plasmafysica Rijnhuizen in the Netherlands. A large part of this work has been carried out at the Institut für Plasmaphysik at Forschungszentrum Jülich, Germany. The research results are presented in this thesis.

After finishing my PhD, I have started as a post-doc at the Tore Supra tokamak at the CEA Cadarache in France under the supervision of Dr. Gerardo Giruzzi.